STUDY OF THE HIGH-LATITUDE IONOSPHERE WITH THE RANKIN INLET POLARDARN RADAR

A Thesis Submitted to the College of
Graduate Studies and Research
In Partial Fulfillment of the Requirements
For the Degree of Mater of Science
In the Department of Physics and Engineering Physics
University of Saskatchewan
Saskatoon

By

Heng Liu

PERMISSION TO USE

In presenting this thesis in partial fulfilment of the requirements for a Postgraduate degree from the University of Saskatchewan, I agree that the Libraries of this University may make it freely available for inspection. I further agree that permission for copying of this thesis in any manner, in whole or in part, for scholarly purposes may be granted by the professor or professors who supervised my thesis work or, in their absence, by the Head of the Department or the Dean of the College in which my thesis work was done. It is understood that any copying or publication or use of this thesis or parts thereof for financial gain shall not be allowed without my written permission. It is also understood that due recognition shall be given to me and to the University of Saskatchewan in any scholarly use which may be made of any material in my thesis.

Requests for permission to copy or to make other use of material in this thesis in whole or part should be addressed to:

Head of the Department of Physics and Engineering Physics
116 Science Place
University of Saskatchewan
Saskatoon, Saskatchewan
Canada S7N 5E2

ABSTRACT

The Super Dual Auroral Radar Network (SuperDARN) of HF coherent radars has been originally designed to monitor echoes, and thus study physical processes, from within the auroral oval, the area with the most frequent occurrence of discrete auroras. Monitoring of higher latitudes, the so-called polar cap (including the magnetic Poles areas), was anticipated because of over-the-horizon nature of the radars, but this capability was considered to be a value-added feature. Recently (2006 and 2008), two new radars at Rankin Inlet and Inuvik (Canada) were installed by the University of Saskatchewan radar group to be able to monitor HF echoes from within the polar cap directly. In this Thesis, two aspects of the Rankin Inlet (RKN) radar observations are investigated. First, occurrence of ionospheric echoes is studied. Assessment of the echo occurrence rate is performed and the rate is compared with observations of concurrently operating Saskatoon and Halley (Southern hemisphere) SuperDARN radars. It is shown that the RKN overall occurrence rates (within the optimal area of detection) are ~20% which is well above the rates for the Saskatoon (~6%) and Halley (~1%) radars. The rates are somewhat smaller in the early morning (02-05 MLT) and postnoon (15-20 MLT) hours of magnetic local time. Seasonally, the rates are smaller for summer with significant drop near the magnetic noon. Secondly, an event of the RKN radar monitoring of a polar cap arc, progressing through the radar field of view, is presented. F region echoes are shown to be stronger in the arc's wake, and they are broader on both its sides. Arc-related sheared plasma flows were demonstrated by considering the radar velocity measurements. Occasional occurrence of strong shears away from the arc was noticed, and it was related to the onset of a second, sub-visual arc, emerging from the auroral oval and intruding the polar cap. The data presented demonstrate the usefulness of the RKN observations of the high-latitude arcs whose mechanism of formation is presently unclear. An attempt has been made to discern magnetic signatures of the polar cap arc. Magnetic perturbations were found to be very weak and not easily interpreted.

ACKNOWLEDGEMENTS

I would like to take this opportunity to thank all those people who made this Thesis possible. First and foremost, I thank Dr. A. V. Koustov, my supervisor, for the direction and continuous support I have received. If not him, I would not accomplish this Thesis work. Many thanks go to all members of the Institute of Space and Atmospheric Studies and the Department of Physics and Engineering Physics. Efforts of the Saskatoon radar group in making high-quality Rankin Inlet radar measurements used in the Thesis are appreciated. Special thanks are to Dr. D. Andre and R. Fiori for their help with IDL programming. This Thesis is based on various other data sets. OMTI all-sky camera data collection and their processing have been done by Dr. K. Hosokawa (University of Electro-Communications, Tokyo, Japan). His significant contributions to the Resolute Bay project of the Thesis are very much appreciated. The Resolute Bay OMTI camera (http://gwave.ice.uec.ac.jp/cgi-bin/hosokawa/resolute/resolute.cgi) has been operated in cooperation between the Solar Terrestrial Environment Laboratory, Nagoya, Japan (Dr. K. Shiokawa) and the University of Electro-Communications, Tokyo, Japan (Dr. K. Hosokawa). I also thank Drs. E. Donovan and E. Spaswick (University of Calgary) who providing Taloyak optical data. CARISMA and NRCAN magnetometers data were downloaded from the Canadian Space Agency Data Portal (http://portal.cssdp.ca:8080/ssdp/jsp/logon.jsp). ACE data were obtained from CDAWEB site (http://cdaweb.gsfc.nasa.gov/istp_public/) where they were provided by Dr. D. J. McComas of Southwest Research Institute.

Finally, I extend my gratitude to my family for their constant support and encouragement.

TABLE OF CONTENTS

LIST OF TABLES

LIST OF FIGURES

LIST OF ABBREVIATIONS

ACF	Autocorrelation Function
CADI	Canadian Advanced Digital Ionosonde
CBB	Cambridge Bay
CARISMA	Canadian Array for Realtime Investigation of Magnetic Activity
CSA	Canadian Space Agency
CW	Clockwise
DMSP	Defense Meteorological Satellite Program
EISCAT	European Incoherent Scatter
FAC	Field-Aligned Currents
FB	Farley-Buneman
FFT	Fast Fourier Transform
FoV	Field-of-View
GD	Gradient-Drift
HAL	Halley
HF	High Frequency (3 – 30 MHz)
IMF	Interplanetary Magnetic Field
INV	Inuvik
IRI	International Reference Ionosphere
ISIS	International Satellite for Ionosphere Studies
l-o-s	line-of-sight
MLAT	Magnetic Latitude
MLT	Magnetic Local Time
OMTI	Optical Mesosphere Thermosphere Imager
PC	Polar cap
PolarDARN	Polar Dual Auroral Radar Network
R_E	Earth radius
RES	Resolute Bay
RKN	Rankin
SA	Sun-aligned arc
SAS	Saskatoon
SuperDARN	Super Dual Auroral Radar Network
TALO	Taloyak
UT	Universal time
UV	Ultra vilot
VHF	Very High Frequency (30 – 300 MHz)

CHAPTER 1

INTRODUCTION

Since the initial suggestion by Gilbert in 1800s, it is believed that the Earth's magnetic field can be well approximated by a dipole. However, as a result of reconnection, the dipole magnetic field lines near the Poles are stretching into the outer space, and are connected directly to the magnetic field in the interplanetary media, the so called interplanetary magnetic field (IMF), that is mostly the Sun's magnetic field near the Earth's orbit. Such high-latitude magnetic field lines are said to be "open". This is in contrast to the magnetic field lines at lower latitudes, say less than 80^0, where they are "closed" in a sense that an individual magnetic field line in the southern hemisphere ends up in the northern hemisphere.

The Earth's open magnetic field lines are associated with a distinct class of processes occurring in the near space, and signatures of those can be detected through observations on the ground at very high latitudes, close to the magnetic Poles. One of these are high-latitude auroras that show up and disappear suddenly in the sky near the Poles. These auroras do not last for a long time, but they can be as dynamic and, once in a while, as intense as the auroal zone (latitudes of 60^0-70^0) auroras. Study of the very high-latitude processes is important for understanding the mechanisms of Sun's energy penetration into the upper atmosphere and possible harmful effects of this energy on various technological systems operating in the near Earth space. The extreme latitudes are less explored as regular observations with geophysical instruments in High Arctic and Antarctica are difficult to perform.

This Thesis considers measurements from a number of instruments working in the Canadian sector of High Arctic to investigate two major phenomena occurring on supposedly open magnetic flux lines, the excitation of small-scale irregularities of charged particles at heights of ~ 300 km and occurrence of a special type of auroras, the arcs, that are visible as a stripe of luminosity stretched towards the Sun. One of our goals is to locate and investigate an arc event for which both phenomena co-exist and to unravel, if possible, physical processes associated with both phenomena. In this Chapter

we give a brief overview of the environment we will be dealing with, describe some processes and formulate, in more detail, the goals of the Thesis.

1.1 Solar wind

The Sun provides energy to the Earth in a number of forms. Everyone is familiar with warms and heat coming with its light. Less known is the fact that a fraction of total energy comes from particles emitted from the Sun and reaching the Earth environment. The idea of the presence of a "torrent or flying cloud of charged atoms or ions" from sunspots was first hypothesized by Fitzgerald (1882, 1900). Then in 1931, Chapman and Ferraro discussed the interaction of supersonic expansion of solar corona as the solar wind. Chapman and Ferraro (1931) proposed that a current would set on the front side of the Earth's magnetic field cavity, the effect of which is detectable on the ground. Parker (1958) named this flow the "solar wind". In the early 1960s the existence of the solar wind as a continuous stream present at all times was proven by Russian and American space probes. During that time it also was discovered that the solar wind carries with it a magnetic field (Sonett, 1960), which was termed the IMF.

According to measurements near the Earth's orbit, the solar wind is composed of electrons and ionized hydrogen (protons) in approximately equal ratio with ~ 5% (by number) admixture of ionized helium. The ions of heavier elements are also present but in much fewer numbers. The proton density is ~5 particles per cubic centimeter, and the proton and electron temperatures are of the order of 10^5 K. The solar wind flow velocity is about 450 km/s on average, but it can be anywhere from 300 to 2000 km/s.

1.2 Magnetosphere

The Earth has its own magnetic field, and its interaction with the solar wind, carrying the IMF, leads to development of a special cavity, in the near Earth environment. It is called the magnetosphere. The particle motion there is determined by the Earth's magnetic field. The magnetosphere has a complex structure. Due to the particle and energy input from the solar wind and the Sun's radiation, the magnetosphere

contains particle populations with a vast spectrum of energies. The charged and neutral particles of different energies behave differently in the magnetosphere, which leads to formation of special magnetospheric regions and the magnetospheric current systems.

Figure 1.1 shows the shape and some of the major regions of the Earth's environment. When particles of the solar wind approach the Earth, they begin their journey around it in a curved surface called the "bow shock" on the sunward side of the magnetosphere, at ~ 10 R_E (Earth radii, R_E = 6370 km), where the solar wind plasma decelerates to subsonic speeds. This is just like water makes a curved wave in front of a boat. The particles then arrive to a transition region, called the magnetosheath, and finally reach the outer boundary of the magnetosphere, known as the magnetopause. The front-side of the magnetopause is of a round shape and it is extended to the night side forming the magnetotail. While traveling along the magnetopause, some solar wind particles leak through the magnetic barrier and are trapped inside the magnetosphere. Some particles can penetrate directly into the upper atmosphere in the areas denoted in Fig. 1.1 as “neutral points”, but this is not the most “popular” way the particles appear in the upper atmosphere.

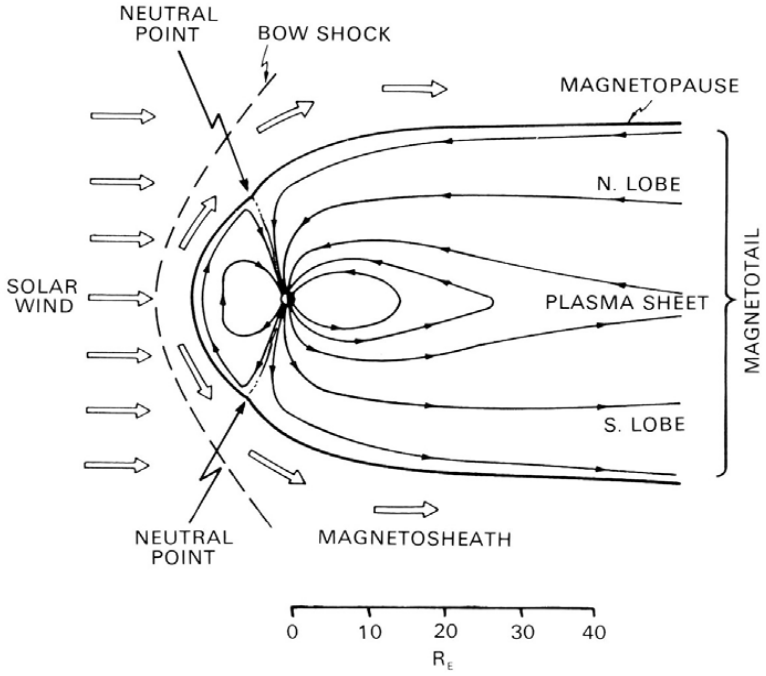

Figure 1.1. Characteristic regions of the near Earth environment in the north-south plane. Hollow arrows show solar wind flow around the magnetopause (Hargreaves, 1992).

Inside the magnetosphere, a special area exists, the plasma sheet. Here the particles are concentrated and eventually pushed towards the Earth. Figure 1.1 shows typical sizes of the magnetospheric regions. Less obvious from this diagram is the fact that the magnetotail extends up to ~ 100 R_E.

Simultaneously with particle motions near the Earth, the IMF experiences transformations as it interacts with the Earth's magnetic field. There are two possible scenarios, as illustrated in Fig. 1.2. One process is the so-called quasi-viscous interaction, Fig. 1.2a, and the other one is the magnetic merging and reconnection, Fig. 1.2b.

(a)

(b)

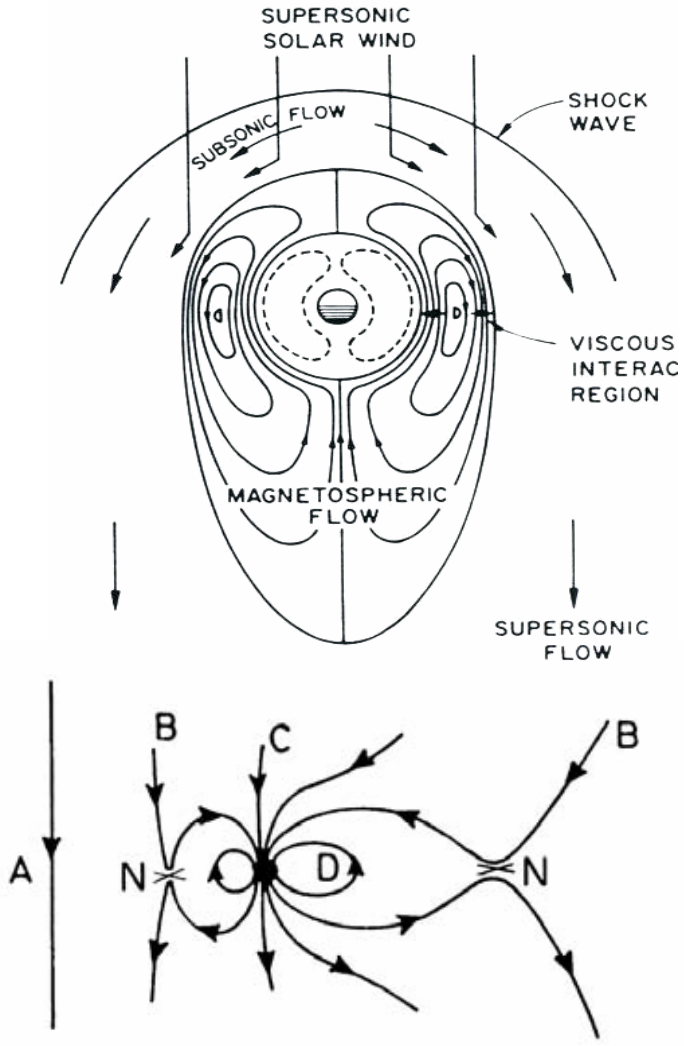

Figure 1.2. Solar wind-magnetosphere interaction processes: (a) quasi-viscous interaction (Kelley, 1989) and (b) reconnection (Craven, 1997).

Quasi-viscous interaction (Axford and Hines, 1961) is a generic name for processes occurring as the solar wind flows around the egg-shaped magnetosphere and drags along the IMF. The magnetosphere is assumed to be closed. Energy and momentum are transferred from the solar wind to the outer magnetosphere causing anti-sunward flow in the outer regions of the enclosed plasma. Because the system is closed, this flow reverses at the far nightside end of the magnetosphere (accumulation of flux lines here provides additional pressure) causing plasma to flow back toward the Earth and around the so called inner magnetosphere, that part of the magnetosphere where magnetic field lines are co-rotating with the Earth and where, generally, particles are not allowed to go in. Sunward motion is transferred to the outer edges of the inner magnetosphere.

According to the reconnection theory, proposed by Dungey (1961) for southward IMF, the IMF lines "merge" with the terrestrial field lines at the subsolar region of the magnetopause (point "N"), making "open flux tubes", Fig. 1.2b, tubes "C". The open tubes are then carried downstream by the magnetosheath flow and stretched into a long cylindrical tail. Eventually, the open tubes close again by reconnection in the centre of the magnetotail, point "N" in Fig. 1.2b. As a result of reconnection, some of the open field lines are converted back to regular IMF lines in the solar wind (line A in Fig. 1.2b). The other portion of the reconnected lines becomes closed terrestrial field lines. These field lines shrink as they move sunward along the magnetosphere flanks and eventually get into the dayside subsolar part of the magnetosphere, where they become subject to the dayside merging. The reconnection process excites the cyclical flow in the interior called plasma convection. The overall flow cycle is ~ 12 hours, of which field lines remain open mapping into the tail lobe for ~ 4 hours and then take ~ 8 hours to convert back from the tail to the dayside. Plasma flows in the magnetosphere are "projected" along the magnetic lines onto the lower levels, with the most important one at the heights of 100-300 km, where a highly conducting layer of the upper atmosphere exists, the so called ionosphere. The ionospheric image of the magnetospheric flow circulation consists of two convection cells with antisunward flow on open field lines over the Pole and a return sunward flow on closed field lines at lower latitudes.

1.3 Ionosphere

The ionosphere is that part of the upper atmosphere where a significant amount of charged particles are present. It is conventionally divided into three distinct regions, the D, E and F regions (Hargreaves, 1992). Figure 1.3 shows typical electron density profiles for day and night at solar maximum and solar minimum conditions.

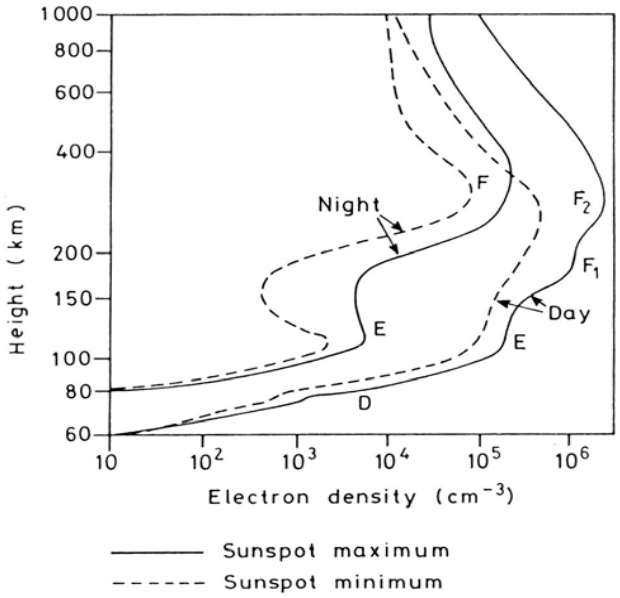

Figure 1.3. Ionospheric electron density profiles for day and night for both solar minimum and solar maximum (Hargreaves, 1992).

The F region is the upper ionospheric region (150 – 350 km), where the electron density peaks at ~ 250 km and a value of ~ 10^6 cm^{-3}. At F-region heights atomic oxygen is the dominant neutral atom, therefore, photoionization produces an abundance of O^+, and the dominant ion is O^+. In the absence of photoionization at night time, recombination results in a depletion of the F-region electron density but not as strong as in the E region.

The E region is the middle part of the ionosphere (90 – 130 km), where the electron density peaks at an altitude of ~ 120 – 130 km with values of ~ 10^5 cm^{-3}. At these heights the dominant neutrals are O, O_2 and N_2, with N_2 being the most dominant. The ionized component is formed primarily due to photoionization and ionization by precipitating energetic particles. All three neutrals are photoionized with a reaction such

as $X + h\nu \rightarrow X^+ + e^-$, where X represents the neutral species O, O_2 and N_2. Although N_2 is the most dominant neutral, there is no build up of N_2^+, because of an important series of interchange reactions that occur between ionized and neutral N_2 and O. The two most frequent reactions are $N_2^+ + O \rightarrow NO^+ + N$ and $O^+ + N_2 \rightarrow NO^+ + N$, which leads to an accumulation of NO^+ instead of N_2^+. No interchange reaction occurs with O_2^+, which leads to a build up of O_2^+ and the dominant ions in the E region are then NO^+ and O_2^+. In the absence of photoionization at night, recombination in the E region results in significant weakening and even disappearance of the E region. In the high-latitude ionosphere this effect is reduced by particle precipitation which can produce some ionization at night time.

The lowest ionospheric region, the D region (60 – 90 km), has the lowest electron density of ~ 10^4 cm^{-3}. As in the E region, the dominant positive ions are NO^+ and O_2^+. Additionally, electrons can attach to neutrals, creating negative ions. In the absence of photoionization at night, the D region completely disappears. The D region often does not have a peak and forms a ledge in the electron density profile. However, the D region is considered separately from the E region because the processes of its formation are quite different, mainly because of a chain of complex chemical reactions occurring here.

1.4 Plasma motions in the ionosphere

The ionospheric plasma is in a constant motion. It is driven by neutral winds and electric fields established in the ionosphere as plasma convects in the magnetosphere. For high latitudes, the electric field is the major source of plasma motion. For work with HF radars, the main instruments in this Thesis, motions at the E and F region heights are important. To estimate the velocity of electrons and ions we consider a configuration with a vertical magnetic field **B**, oriented in the negative *z* direction, and an electric field **E** oriented in the *x* direction.

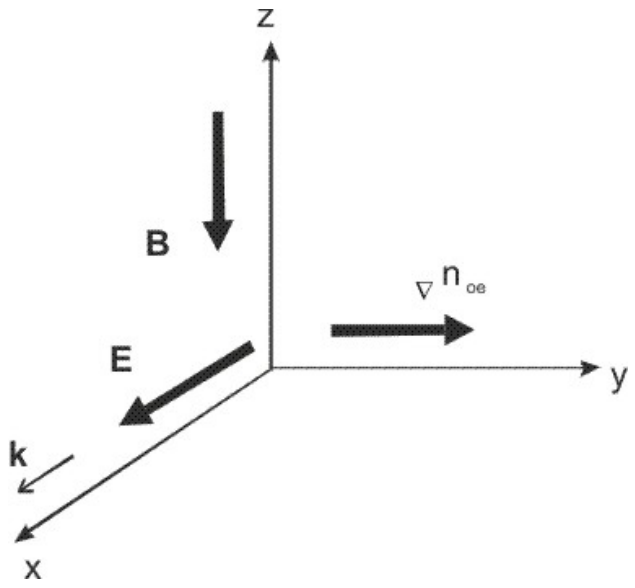

Figure 1.4. Configuration of electric and magnetic fields and background gradient of the electron density adopted for the analysis.

We consider simplified equations of charged particle motion that are considered to be valid for the heights below ~200 km where collisions between charged particles can be neglected (Kelley, 1989)

$$m_\alpha \frac{d\mathbf{V}_\alpha}{dt} = q_\alpha \left[\mathbf{E} + \mathbf{V}_\alpha \times \mathbf{B}\right] - m_\alpha \nu_{\alpha n} \mathbf{V}_\alpha , \tag{1.1}$$

where α=*i*,*e* represents either ions or electrons, $\nu_{\alpha n}$ is the collision frequency of a species α with neutrals, m_α and q_α are the mass and charge of ions or electrons. The terms due to pressure gradients were omitted in equations (1.1) as they are not important. For stationary conditions (d/dt=0), the particle fluid velocity $\mathbf{V}_\alpha$ from equation (1.1) can be written in a form

$$\mathbf{V}_{0\alpha} = \frac{\Omega_\alpha \nu_{\alpha n}}{\Omega_\alpha^2 + \nu_{\alpha n}^2} V_0 \frac{\mathbf{E}}{|\mathbf{E}|} + \frac{\Omega_\alpha^2}{\Omega_\alpha^2 + \nu_{\alpha n}^2} V_0 \frac{\mathbf{E} \times \mathbf{B}}{|\mathbf{E} \times \mathbf{B}|} \quad , \tag{1.2}$$

where

$$V_0 = \frac{E}{B} , \tag{1.3}$$

which will be referred to as the magnitude of the **E**x**B** plasma drift or plasma convection, Ω_α is the particle gyrofrequency given by $\Omega_\alpha = \frac{q_\alpha B}{m_\alpha}$.

In equation (1.2), the first term on the right describes particle fluid motion along the direction of electric field, and the second term describes particle motion along the **E**x**B** direction, both in a plane perpendicular to the magnetic field. In the F-region $\nu_{\alpha n} << \Omega_\alpha$, the first term in equation (1.2) is very small and can be neglected while for the second term, the coefficient $\Omega_\alpha^2/(\Omega_\alpha^2 + V_{\alpha n}^2)$ can be approximated as 1, so that equations (1.2) can be reduced to

$$\mathbf{V}_{0\alpha} = V_0 \frac{\mathbf{E}\times\mathbf{B}}{|\mathbf{E}\times\mathbf{B}|}. \tag{1.4}$$

Equation (1.4) implies that both electrons and ions move with the same velocity along the **E**x**B** direction. This process is often referred to as plasma convection. There are nonzero particle fluid velocities along the electric field, although they are small. The ion velocity is larger and can be described by equation:

$$\mathrm{V}_{0i} = \frac{\nu_{in}}{\Omega_i} V_0 \frac{\mathrm{E}}{|\mathrm{E}|}. \tag{1.5}$$

For the bottom side of the F region, $\nu_{in}/\Omega_i \approx 10^{-2}$. This implies that there is a relative drift between electrons and ions $\sim 0.01 V_0$ along the direction of electric field. This drift is called the Pedersen drift. Its existence is important for generation of small scale irregularities that we consider in the following section.

For the bottom of the E region, the expression for the fluid velocity of electrons is the same but for ions it changes because at these heights $\nu_{in}/\Omega_i >> 1$. The velocity of ions can be expressed (from equation 1.2) as

$$\mathbf{V}_{0i} = \frac{\Omega_i}{\nu_{in}} V_0 \frac{\mathbf{E}}{|\mathbf{E}|}. \tag{1.6}$$

An important conclusion from this equation is that electrons and ions do not move/convect with the same velocity in the E region. Instead, there is a significant relative drift in the **ExB** direction, called the Hall drift. Since velocity of ions is $\sim 0.1 V_0$ (from equation 1.6), and it is along the direction of E field (equation 1.6), the Hall drift

vector is oriented exactly along the **ExB** direction, and its magnitude is equal to the $\left|\frac{E}{B}\right|$.

Presence of a strong relative drift between the electrons and ions coupled with significant electron density in the E region leads to excitation of a strong current detectable with magnetometers, instruments sensitive to changes of the geomagnetic field. We mention that the Pedersen drift still exists at these height, but it is of secondary importance.

Existence of relative drift between electrons and ions in the ionosphere can lead to the development of plasma instabilities, amplification of chaotic plasma density fluctuations of certain scale. The end result of instabilities is the creation in the ionosphere of micro structures of the electron density that can scatter radio waves.

1.5 Gradient drift plasma instability

Plasmas are capable of supporting a number of wave motions, for example electrostatic waves at plasma frequency. These oscillations would normally die because of the diffusion damping. However, in the presence of sources of energy, and in a case of a possibility of this energy to be transferred to waves, the spontaneous weak waves can grow and lead to the so called plasma instability. The unstable waves would grow to some amplitude and thus electron density waves/irregularities would be excited in the plasma. It is very important to know the growth rate and threshold for a plasma instability as this would indicate conditions for which ionospheric irregularities would occur, and various systems such as coherent radars can be used for their detection and thus investigated. It is also very important to know the velocity of plasma waves as scatter from them would give information on the electric field and thus one can remotely diagnose the plasma conditions in the ionosphere.

There are many processes that can lead to plasma instability and generation of density structures in the ionospheric plasma. Here we concentrate on one of these that is considered to be the most likely mechanism of ~10 m irregularity formation in the high-latitude F region, the gradient drift (GD) instability.

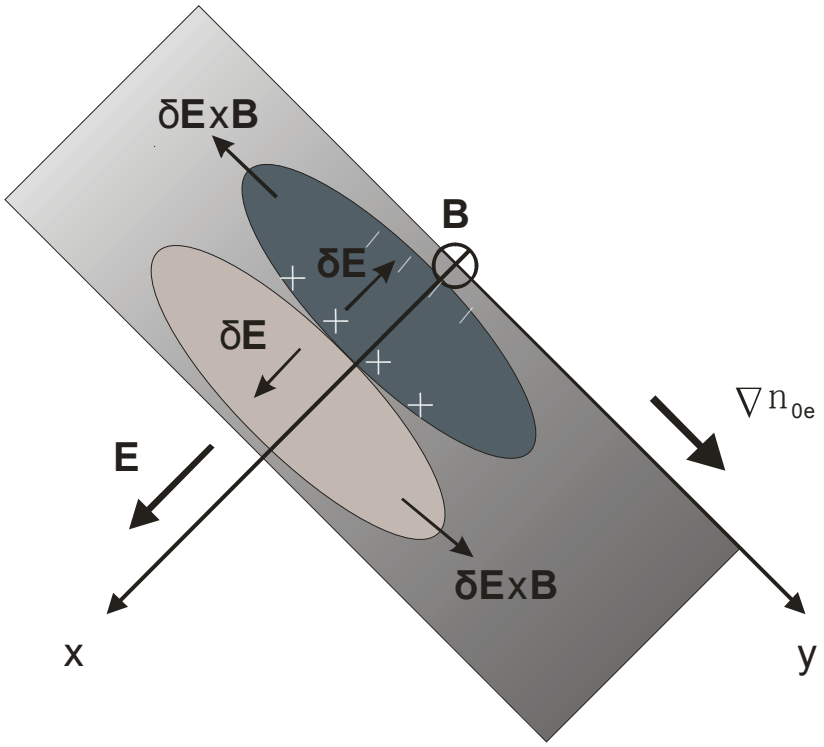

Figure 1.5. Ionospheric configuration for the gradient drift instability in the F region. Dark (light) shading indicates density enhancement (depletion).

Consider an F region plasma configuration shown in Fig. 1.5. We assume that there is a downward directed magnetic field, an electric field in the *x* direction and plasma density gradient in the *y* direction. Let us consider blob-like perturbations in the electron density established in the ionosphere. The dark shading indicates a density enhancement in the perturbation, and the light shading indicates a density depletion. As these blobs are set, the polarization electric fields $\delta\mathbf{E}$ will be established inside the blobs, as shown in Fig. 1.5. This happens because the ions move along the direction of the electric field with Pedersen speed of V_{0i} and the electrons have alomost no Pedersen drift speed. As a result, charges would build up on blob edges as shown in Fig 1.5. Because plasma as a whole (electrons and ions) is moving in the **ExB** direction at the F region heights, blobs with enhanced (depleted) plasma would $\delta\mathbf{E}\times\mathbf{B}$ drift in the negative (positive) *y* direction. This means that, if there is a plasma density gradient in the *y* direction as shown, then the blobs with enhanced (depleted) density move to the

low (high) density regions, implying wave amplitude increase (instability) of the density perturbation.

To describe the instability quantitatively, we consider one Fourier component of the perturbation blob with wave vector **k** and frequency ω. We also consider a more general case where **k** is directed away from the *x* axis. The frequency and growth rate of the sinusoidal perturbation can be determined as follows. First, one has to consider the simplified equation of motion but neglect the effects of particle inertia, ion-electron collisions and the neutral wind. Also, one has to consider the continuity equation for ions and electrons:

$$\frac{\partial n_\alpha}{\partial t} + \nabla \cdot (n_\alpha \mathbf{V}_\alpha) = 0 . \tag{1.7}$$

Linearizing these equations, and requiring non-trivial solution of two equations for two unknowns (usually perturbation in the electrostatic potential and electron density), one obtains the dispersion equation. By assuming $\omega = \omega_r + i\gamma$, where ω_r and γ are the frequency and the growth rate of the perturbation, one can solve the dispersion equation to obtain

$$\gamma = \frac{V_0}{L}\cos^2\theta - k_\perp^2 D_\perp , \tag{1.8}$$

where $\theta = \cos^{-1}\left(k_x / k_\perp\right)$ is the azimuthal angle of the $\boldsymbol{k}$ vector with respect to the *x* axis, $D_\perp = (\nu_{en}/\Omega_e\Omega_i)C_s^2$ is the diffusion coefficient, $C_S = \sqrt{\frac{T_e + T_i}{m_i}}$ is the ion-acoustic speed (T_e and T_i are temperature of electrons and ionos), and *L* describes the scale of the plasma gradient:

$$\frac{1}{L} = \frac{\nabla n}{n} . \tag{1.9}$$

Detailed derivation of the expression (1.8) is given in Appendix A. Equation (1.8) implies that a perturbation propagating along *x* axis would grow faster than perturbation along any other direction. At large angles θ, the plasma is stable and no linear wave generation is possible. According to (1.8), γ is larger for larger |**E**×**B**| drift and for stronger plasma gradient. It is important to note that the GD plasma instability in the F

region can directly generate only irregularities with a scale-size of tens of meters (otherwise, the last term in (1.8) is larger than the first term and the growth rate is negative). The ~10-m irregularities observed by HF radars such as the SuperDARN radars, that are to be used in this Thesis, are obtained through the non-linear cascading of energy from large to small scales (Tsunoda, 1988). One should also note that waves of larger scale (hundreds of meters), corresponding to smaller $|\boldsymbol{k}|$ values, cannot be linearly generated because of recombination effects (Tsunoda, 1988). The value of $1/\gamma$ gives an estimate of how much time is needed to develop ionospheric irregularity. For typical auroral F region parameters $\nu_{en}/\Omega_e = 10^{-4}$, $C_s = 450\, m/s$ (so that $D_\perp = 0.21\, m^2/s$) and $E_0 = 10\ mV/m$, $L = 10\, km$, one can find that the fastest growing modes with wavelength of ~30 m have growth time of $\gamma^{-1} \approx 100\, s$.

1.6 High-latitude auroras and plasma flow in the ionosphere

Aurora is a dynamic ionospheric phenomenon and an indicator that a host of plasma processes are occurring. The aurora delineates those ionospheric regions where particles from the magnetosphere reach the upper atmosphere. For this reason, studying the distribution of the aurora and plasma flow around it can provide clues as to the origins of various kinds of auroras, and the electric field structure around them.

1.6.1 Auroral oval

The scientific study of aurora started as early as the seventeenth century (Akasofu, 1964; 1976). Auroral displays occur mainly in the high-latitude ionospheric regions of both northern and southern hemispheres and can appear in all local time sectors with various patterns and intensities. In general, the areas of most frequent occurrence of aurora occupy a space of oval belt centered around the magnetic Pole with somewhat larger shift to the equator in the midnight sector. Figure 1.6 gives an example of auroral oval for moderately disturbed magnetic conditions of the planetary magnetic index Kp=4; panel (a) is a digitized "statistical" oval as originally obtained by Feldstein and

Starkov (1967) while panel (b) shows actual measurements of the auroral UV emission made by the IMAGE satellite on 02 February 2002 at 03:09 UT.

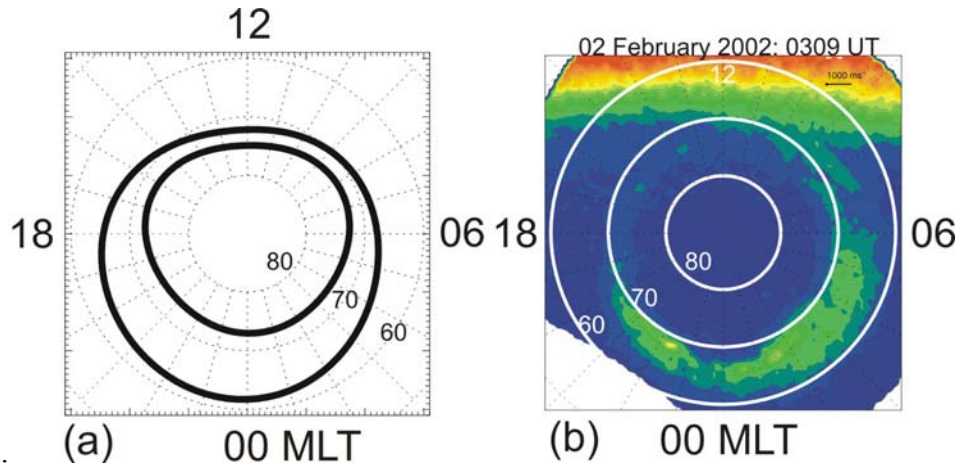

Figure 1.6. (a) Statistical Feldstein-Starkov auroral oval for Kp=4 and (b) Auroral luminosity map in UV radiation from the IMAGE satellite observed on 02 February 2002 at 03:09 UT.

The contours describe the "original" oval as it was inferred as an area where discrete auroral arcs would be frequently observed (Feldstein and Starkov, 1967). Nowadays, especially with introduction of UV imagers, the oval can be observed on a regular basis from a single camera on a satellite. Figure 1.6b shows that the oval occupies much higher latitudes of 72^0-75^0 on the dayside, and that typical nightside latitudes are 60^0-70^0.

The aurora can be classified into two types. The first is the diffuse aurora, which shows a uniform luminosity and is driven by a fairly uniform electron flux through the aurora. The other is the discrete aurora or auroral arcs, which are narrow structures of luminosity and for which the average energy and electron flux vary considerably across the aurora.

1.6.2 Auroras in the polar cap

In this Thesis we are concerned about a specific type of discrete aurora, the arcs occurring in the polar cap, the region poleward of the auroral oval. We prefer to use the term 'polar cap arcs' to refer to the general types of auroral arcs seen at very high latitudes.

Theta aurora

In contrast to the arcs in the auroral oval which correlate well with the southward IMF, polar cap arcs are mainly observed during periods of northward IMF and quiet magnetic conditions (Berkey et al., 1976; Ismail et al., 1977; Lassen and Danielsen, 1978). The arcs can be very bright and can extend across the polar cap from the dayside to the nightside of the auroral oval. If these arcs are observed from space, the optical emission has a pattern resembling the Greek letter 'theta' (Frank et al., 1982). The theta aurora was first discovered by the Dynamics Explorer 1 (DE1) satellite. Theta aurora is produced by low-energy (0.6-1.0 keV) electrons from the magnetotail. These electrons do not undergo acceleration in near-Earth space, and are therefore less penetrative than those giving rise to classical auroral arcs; the base altitude of theta aurora is high, typically above 200 km.

Sun-aligned arcs

With the help of ground-based all-sky cameras, images of auroral arcs can be taken and studied. Auroras may be described by their overall shape, brightness, location, orientation, motion, spectral composition, and spatial and temporal intensity variations. At first, people did not distinguish between different types of aurora comprising the auroral oval. In 1972, Eather and Mende discovered day-night and latitude variations in the spectral characteristics of auroral oval emissions (Gallagher, 1997). In 1973, Eather advocated a reevaluation of the auroral oval based on the spectral characteristics of the aurora comprising the auroral oval. Within the auroral oval, up to the polar cap boundary, discrete auroras are often observed. Many discrete auroral forms are narrow (<100 km) in latitude and can extend up to thousands of kilometers in longitude. They appear in the sky as an arc segment of a circle and hence are referred to as auroral arcs.

More recent observations showed that arcs can be seen well poleward of the auroral oval. Various names have been used to describe these arcs, for example: Sun-aligned (SA) arcs, transpolar arcs, polar cap (PC) arcs. Although it is not clear whether or not they are the same phenomena, we decided to use the term 'polar cap arcs' to refer

to the high latitude arcs that we will report in this Thesis. We note that although PC arcs have been known for a while, not much information has been collected so far. The PC arcs can be stable or moving. The lifetime of a clear polar arc ranges from several tens of minutes up to many hours. The range of lifetime of moving arcs is from several minutes to hours (Valladares et al., 1991; 1994).

From the statistical data collected over Resolute Bay (RES) and Cambridge Bay (Canada) it has been shown that most arcs at RES move duskward (Shiokawa et al., 1995). If we consider northwestward, northward, and northeastward arc motions to be the duskward motion, about 49% of arcs observed at RES move duskward during magnetically quiet periods. If we ignore the ones not well seen, this value becomes 83%. The typical velocity of the arc motion is ~375 m/s with a slightly higher velocity at lower latitudes (Shiokawa et al., 1995). IMF conditions for the moving arcs are as follows: the B_x component is mostly negative, the B_y and B_z components are often negative prior to and positive after the event.

1.6.3 Plasma flow around polar cap arcs

Information on the plasma flows related to the PC arcs is very limited, and moreover, what is known, has been provided from observations of theta aurora which is a more global and intense phenomenon. Carlson and Cowley (2005) summarized the situation by saying that convection is highly irregular with a number of reversals in the dawn-to-dusk direction. Sometimes, a PC arc (theta aurora) can be seen coinciding with the sunward flow but more frequently with the anrisunward flow. Similar conclusions can be made from coherent HF radar measurements around the theta-aurora (Chang et al., 1998; Milan et al., 2005; Liu et al., 2005; Eriksson et al., 2006). Convection measurements with incoherent scatter radars show that the morning sector PC arcs usually coincide with the convection reversal (Gallaher, 1997).

1.7 Objectives of the undertaken research

This Thesis has two major objectives, both are to be addressed with the recently installed PolarDARN/SuperDARN HF coherent radar at Rankin Inlet.

The first goal is to investigate ionospheric echo occurrence for this radar and discuss differences with two other SuperDARN radars, Saskatoon and Halley. We note that detection of ionospheric F region echoes in the SuperDARN observations is vital for achieving the main objective of the experiment – providing data on plasma convection in a significant portion of the high-latitude ionosphere. To find optimal conditions for better echo coverage, one would want to know the reasons for the onset and disappearance of HF echoes. Although this is a fundamentally important question, so far, it has not been addressed in a systematic way. This is despite the fact that the SuperDARN radars have been in continuous operation since 1993 and more than one full solar cycle has passed since then: the solar minimum of 1995-1997 was followed by the solar maximum of 2001-2002 in the maximum of the cycle 23 and then quiet Sun conditions came back in 2005-2009.

From the first days of RKN radar operation (May 2006), it became clear that this radar shows unusually high echo occurrence rates, as compared to other SuperDARN radars working simultaneously. Moreover, the RKN occurrence rates seem to be even higher than the ones reported for other radars during the solar cycle 23 maximum. This (very fortunate) phenomenon has been, and still is, a mystery that requires further investigation.

As for two other radars, some information on their echo occurrence rates has been reported in the past (e.g., Huber, 1999; Hosokawa et al., 2001; Koustov et al., 2003), but our goal is to compare their data with observations by the RKN radar during the same periods. One of the reasons for such a comparison is a general quest to understand why the echo occurrence rate for the SuperDARN radars varies significantly from one location to another. The Saskatoon radar works in the same time sector as the RKN radar but it is located much more equatorward. There is partial overlap between field of views (FoV) of these radars. The reason behind selection of the Halley radar for the analysis is a recent debate regarding potential location for a third (new) PolarDARN radar. In the

Canadian sector of the Arctic, the magnetic latitude of a site is 5^0-7^0 larger than its geographic latitude. Since this new radar targets processes in the polar cap, and more importantly, plans to operate in conjunction with the incoherent scatter radar at Resolute Bay (MLAT=75^0), one would want to find optimal locations in terms of echo occurrence. Geographically, the RKN radar is located just slightly equatorward of the Arctic circle (66.5^0 geographic latitude) meaning that the radar does not operate in complete darkness, when the electron density in the F region can be very low and so the propagation conditions are not satisfactory to receive HF echoes. If one would place the new radar at higher latitudes, above the polar circle, the propagation conditions would deteriorate, at least for winter months. One would expect then a drop in echo occurrence because of this, but the question is by how much. In this regard, Halley observations are very important. Within this radar field of view, a point has very high geographic latitude but still low geomagnetic latitude. The radar operates in complete darkness for extended periods, and its data would be very instructive in judging the effect of propagation conditions on echo occurrence for observations in Canadian Arctic.

The second objective of this Thesis is to further investigate the capabilities of the Rankin Inlet radar in monitoring and providing information on plasma parameters in the vicinity of the polar cap arcs. This is a very broad area of recent research, and there are many issues that need to be addressed. The fundamentally important one is the plasma flow pattern associated with PC arcs. Resolution of the issue would allow one to make much more definitive conclusions on the mechanism of such arc formation. As we already mentioned, there is no coherent and clear picture on the character of the plasma flows in the PC arc vicinity despite attempts to address the issue with incoherent scatter radars (e.g., Gallagher, 1997), magnetometers (Zhang et al., 1999, the only study known to the author) and with drift meters onboard low-orbiting satellites (e.g., Carlson et al., 1988). Recently, Koustov et al. (2008) presented a case of successful Rankin radar monitoring of a morning PC arc. HF signatures of the PC arc were identified as a strong echo power drop at the arc location, and the onset of sheared flows coinciding with the arc and generation of echoes in the wake of the PC arc that was moving duskward. The echoes considered were very likely coming from the E region. We are targeting in this Thesis a case of Rankin radar monitoring with F region echoes.

One of the reasons is that the E region HF velocity is not related to the **E**x**B** plasma drift velocity in a straightforward manner (Koustov et al., 2005; Gorin, 2008). Detection of F region echoes in the vicinity of the arc would give the **E**x**B** plasma flows. The other aspects that requires further investigation are the relationship between arc-associated flows and the global convection pattern. The data presented by Koustov et al. (2008) were not of satisfactory quality to make definite conclusions.

In summary, the two major objectives of this Thesis are:

1) To assess the ionospheric echo occurrence rates for the Rankin Inlet "polar cap" radar for all seasons of 2007 and compare them with concurrently operating "auroral zone" radars in Saskatoon (the same MLT sector but at lower geographic latitude) and Halley (different MLT sector, and even hemisphere, but at much higher geographic latitude).

2) To isolate and investigate Rankin Inlet radar F region echoes in the vicinity of and during the temporal development of a PC arc event and thus to extend the initial findings by Koustov et al. (2008).

1.8 Thesis outline

The thesis is organized as follows. In the next Chapter 2 we describe the instruments whose data are to be used, with a special emphasis on the SuperDARN radars, the major instrument. We then address the first issue, the ionospheric echo occurrence rates for the Rankin Inlet radar in Chapter 3. In Chapter 4 we investigate in detail one polar cap arc event using optical camera and RKN radar observations. We summarize the results and give suggestions for future research in Chapter 5.

CHAPTER 2

INSTRUMENTS

In this Chapter we introduce three major instruments that will be used in this Thesis. These are a HF radar that measures parameters of coherent echoes, including echo occurrence rate, an optical all-sky camera that is used to map and monitor high-latitude auroras and a fluxgate magnetometer that can detect signatures of aurora-related currents through their disturbances of the Earth's magnetic field. Our goal here is to describe the principles and modes of the instrument operation.

2.1 SuperDARN HF radars

The Super Dual Auroral Radar Network (SuperDARN) system is a network of ground-based, coherent, high frequency (HF) Doppler radars whose primary goal is to monitor ionospheric plasma convection at high latitudes (Greenwald et al., 1995). The SuperDARN radars transmit radio pulses and receive echoes from the ionosphere. The echoes occur because the radar waves are backscattered by the ionospheric irregularities that are often associated with quasi-periodic plasma structures/waves generated in the ionosphere. In the F region, such irregularities are, very likely, produced by the GD instability. We introduced the basic ideas behind the GD instability in the Introduction. It is important to realize that because of strong plasma diffusion along the magnetic field, F region irregularities tend to be elongated in the direction of the geomagnetic field (Hargreaves, 1995). This implies that the wave fronts of the irregularities are stretched along the magnetic field. In order for scattering from such an irregularity to occur, the radar waves must propagate perpendicularly to the magnetic field. The SuperDARN radars are operated in the high frequency band of 8-20 MHz, so that the radio rays can refract in the ionosphere and become perpendicular to the magnetic field lines. The radar backscatter would occur if the radar wavelength is twice that of the scattering

ionospheric irregularity. This means that the SuperDARN radars monitor ~10-m size irregularities.

Currently, 21 SuperDARN radars are operational; 14 radars are located in the northern hemisphere and 7 in the southern hemisphere (Fig. 2.1). Figure 2.1 shows the fields of view (FoVs) of the radars in both hemispheres for ranges of 400-2800 km. One can notice that most of the radars cover geomagnetic latitudes of 60^0-70^0 corresponding to the auroral zone/auroral oval latitudes. Three radars, at Hokkaido, Wallops Island, and Blackstone, are located significantly equatorward of the others; these radars were installed for monitoring plasma flows at middle and low latitudes. Two radars, at Rankin Inlet (Nunavut, Canada) and Inuvik (North West Territories, Canada), are located poleward of all others; these two radars were installed to monitor plasma flows much deeper inside the polar cap as compared to what can be achieved with the "auroral zone" radars. This pair is called the PolarDARN pair to distinguish their target area of monitoring. In Fig. 1a we dark-colored the FoV of the Rankin Inlet radar because its data are of primary interest in this Thesis. The exact position of all SuperDARN radars in geographic and geomagnetic (altitude corrected geomagnetic, ACCGM) coordinates and the radar boresights are listed in Table 2.1. The list of institutions running these radars can be found on the official SuperDARN website at http://superdarn.jhuapl.edu/.

The shown in Fig. 2.1 FoV for each radar is achieved through a single beam scanning over 16 directions separated by ~3.24° in azimuth. Thus, the azimuthal width of one SuperDARN radar FoV is ~52°. Measurements for each beam position are performed at 75 distinct "range gates" that are 45 km in range, with the first gate starting at a distance of 180 km. The full scan used to last 2 min but lately the scans have been shortened to 1 min. This means that the radar beam stays for ~3 s in each position. Each SuperDARN radar has a line of 16 individual equally spaced antennas constituting the main array that is used for transmission and reception of radio signals.

Antennas have a height of ~15.24 m above the ground and between each array the distance is also ~15.24 m (the Saskatoon radar). Most of the radars have an additional array of 4 antennas that are used for measurements of the elevation angle of arriving radio waves.

Table 2.1: SuperDARN radar locations and radars boresight directions from geographic North

Radar	Geog Lat (ºN)	Geog Long (ºE)	AACGM Lat (ºN)	AACGM Long (ºE)	Boresight Direction (º)
King Salmon	58.68	-156.65	57.43	-100.51	-20.0
Kodiak	57.61	-152.19	57.17	-96.28	30.0
Prince George	53.98	-122.59	59.88	-65.67	-5.0
Saskatoon	52.16	-106.53	61.34	-45.26	23.1
Kapuskasing	49.39	-82.32	60.06	-9.22	-12.0
Goose Bay	53.32	-60.46	61.94	23.02	5.0
Stokkseyri	63.86	-22.02	65.04	67.33	-59.0
Pykkvibaer	63.77	-20.54	64.48	68.48	30.0
Hankasalmi	62.32	26.61	59.78	105.53	-12.0
Wallops Island	37.93	-75.47	30.93	75.52	26.14
BlackStone	37.10	-77.95	48.59	-3.627	-32
Hokkaido	43.53	143.61	38.14	145.67	30.0
Rankin Inlet	62.82	-93.11	72.96	-28.17	5.7
Inuvik	68.35	133.00	71.45	87.67	29.47
Halley	-75.52	-26.63	-61.68	28.92	165.0
Sanae	-71.68	-2.85	-61.52	43.18	173.2
Syowa South	-69.00	39.58	-66.99	72.06	165.0
Syowa East	-69.01	39.61	-67.00	72.06	106.5
Kerguelen	-49.35	70.26	-58.73	122.14	168.0
TIGER Bruny Isl	-43.38	147.23	-55.31	-133.36	180.0
TIGER Unwin	-46.51	-168.38	-55.15	-106.54	227.9

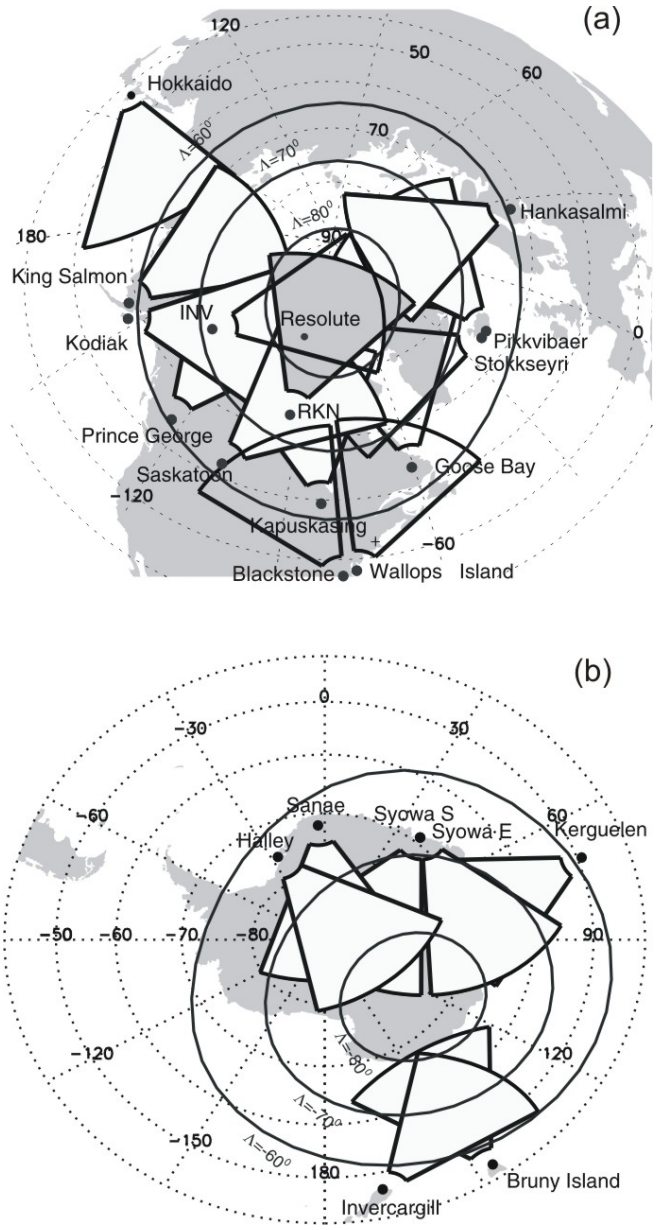

Figure 2.1. SuperDARN radar fields-of-view (FoVs) for the (a) Northern and (b) Southern hemispheres. Shaded area in panel (a) is the FoV of the Rankin Inlet (RKN) radar whose data will be extensively investigated in this Thesis. Also shown are the lines of equal magnetic latitudes of 60^0, 70^0 and 80^0.

The radars transmit a pulse sequence consisting of 5 to 9 pulses. Lately, an 8-pulse sequence designed by Dr. McWilliams (U of Saskatchewan) is widely accepted as the one providing better opportunities to properly measure very large Doppler velocities. Such sequence is adopted for the Rankin Inlet radar operation, Fig. 2.1. Each pulse in the

sequence is 300 μs in duration, and pulses are separated by non-repeating integer multiples of the 1500-μs lag time.

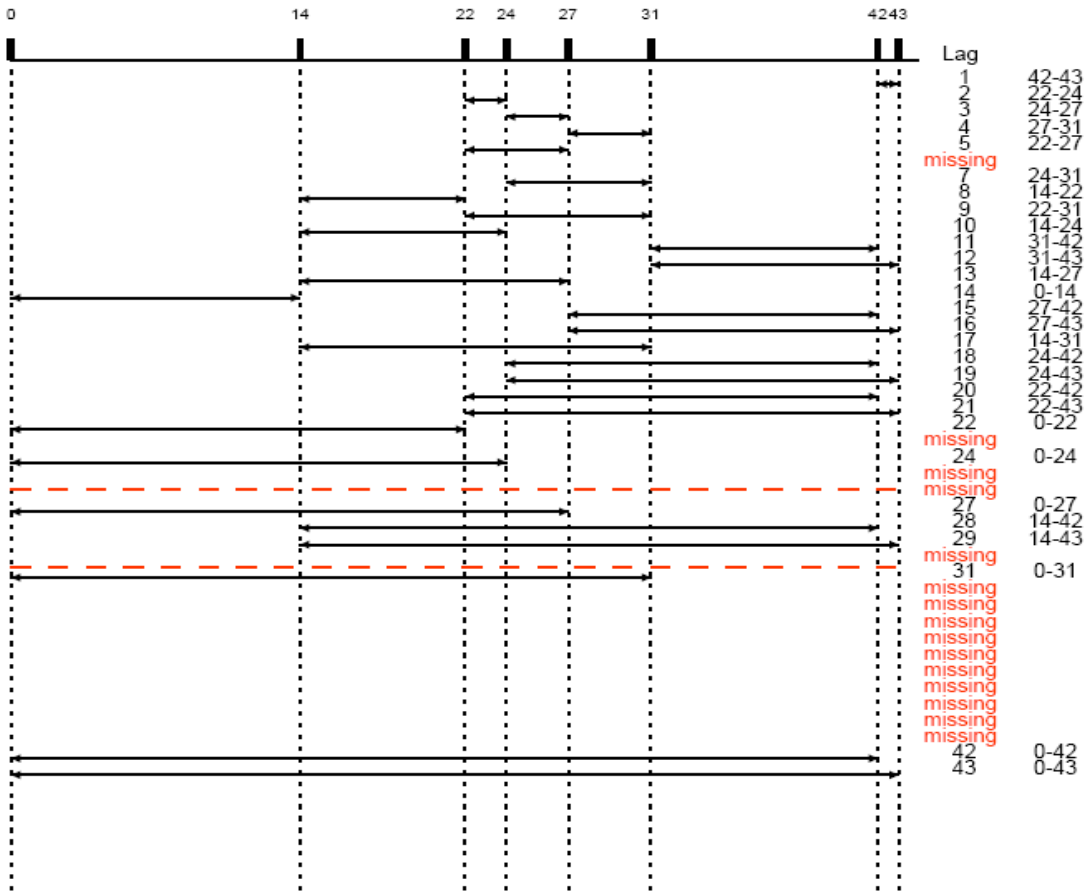

Figure 2.2. 8-pulse sequence currently used in Rankin Inlet PolarDARN radar observations (re-created with the original program by K. McWilliams/A. Schiffler, U of Saskatchewan).

Some lags in Fig. 2.2 are indicated as 'missing'. This is because for 8-pulse sequence, the maximum possible lag numbers is $8 \times (8\text{-}1)/2=28$, so that there are 15 missing lags for the lag number between 1 and 43. The first missing lag has number 6. We note that out of the 28 possible lags, not all are available as some of them are not suitable for the analysis and often called "badlags" (this will be explained later).

The pulses returned from the ionosphere are sampled and processed to generate the complex autocorrelation function (ACF) for various time delays between them and for all ranges between 180 and ~3600 km (gate 75, although recently sampling in a

larger number of gates is sometimes used). For a good ACF, the real and imaginary components of the signal should have the shape of a decaying sinusoid.

Several comments need to be made about generation of ACFs before a procedure to derive the velocity, power and spectral width is described. The ACF approach implies correlation of signals transmitted at different times but received from the same range. Unfortunately, this is not always easy to accomplish.

Figure 2.3 explains some features of ACF derivation for a case of two pulse transmission. At time t_0 ($t_0 + \tau$) the first (second) pulse is transmitted. We assume scattering occurs at three different ranges: d_0, d_-, d_+.

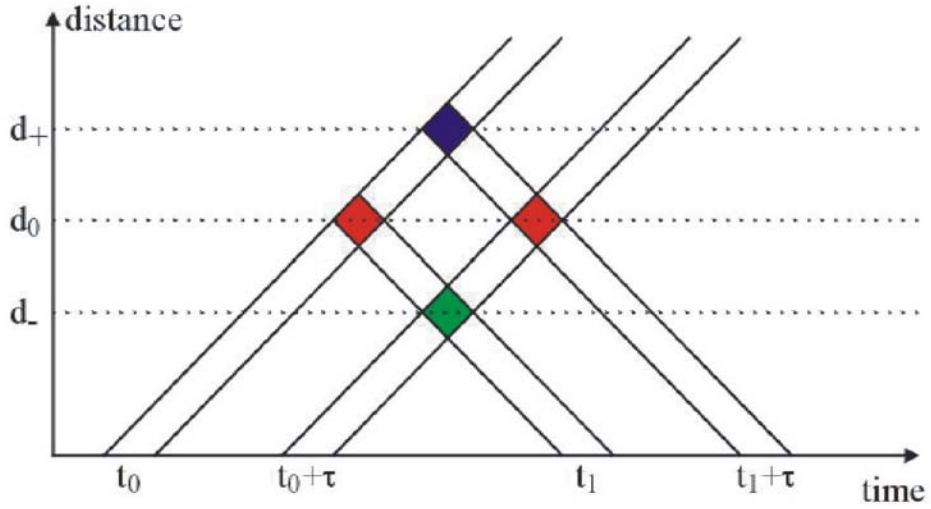

Figure 2.3. Space-time diagram for a two pulse sequence (from Huber, 1999).

The echo 1 with amplitude $A_1(d_0)$ arrives at time $t_1 = t_0 + 2d_0/c$, which is also the time when the echo 2 return as $A_2(d_-)$ from range d_-, so that the total amplitude is

$$A(t_1) = A_1(d_0) + A_2(d_-). \tag{2.1}$$

At time $t_1 + \tau$, the echo 2 returns from d_0 with an amplitude of $A_2(d_0)$, and also echo 1 returns from range d_+ with amplitude $A_1(d_+)$, so at this time, the total amplitude is

$$A(t_1 + \tau) = A_1(d_+) + A_2(d_0). \tag{2.2}$$

These two amplitudes are averaged over a number of pulse sequences to give the ACF:

$$< A(t_1)A(t_1+\tau) >=< A_1(d_0)A_2(d_0) > + < A_1(d_0)A_1(d_+) > + < A_2(d_0)A_2(d_-) > + < A_1(d_+)A_2(d_-) > \ . \quad (2.3)$$

Since the last three terms are considered to be the time-average of uncorrelated signals, the equation (2.3) can be simply written as

$$< A(t_1)A(t_1+\tau) >=< A_1(d_0)A_2(d_0) > , \quad (2.4)$$

which has the information about range d_0 and lag τ. An important aspect of the above consideration is that the measurements at a certain range could be affected by signals from other ranges if the time-average of the last three terms in (2.3) is not exactly equal to zero.

Figure 2.4 gives an example of the ACF and illustrates how it is analyzed (Villain et al., 1987). For a good ACF, the real and imaginary components of the signal have a shape of a decaying sinusoid, just as shown in Fig. 2.4a where the real and imaginary components of the ACF are plotted against lag number. The rate of change of the ACF phase angle Φ is used to determine the Doppler velocity of the echo, Fig. 2.4c. It is assumed that $\Phi =< \omega_D > k\tau$, where *k* is the lag number. The slope of the best fit line to this plot is the Doppler frequency ω_D of the echo, which is related to the measured Doppler velocity (irregularity velocity) as

$$V_I = V_D = \frac{c\omega_D}{4\pi f_R} , \quad (2.5)$$

where *c* is the speed of light in vacuum. Recently, a correction of this equation has been suggested by replacing speed of light in vacuum by speed of light in the ionospheric plasma (e.g., Gillies et al., 2009). To derive equation (2.5) we have to take into account two shifts in the frequency of radio waves due to the Doppler Effect. Assuming f_T to be the frequency of a transmitted by the radar wave, V_I to be the irregularity velocity, the frequency f_I measured by the system "moving with the irregularity" would be $f_I = f_T(1+V_I / c)$ due to the Doppler effect. When the signal is getting back, there is another Doppler shift (since irregularity is moving with respect to the radar) which leads to radar-measured frequency of $f_R = f_I /(1-V_I / c)$. Combining both shifts, we get the

radio wave frequency received by the radar as $f_R \approx f_T(1+2V_I/c)$. From here, the irregularity velocity is $V_I = c(f_R - f_T)/2f_T$. Since $f_D = f_R - f_T$ is related to ω_D through $f_D = \omega_D/2\pi$, one arrives to equation (2.5).

Power and spectral width of echoes are determined by considering the decay of the ACF. The signal decay is assumed to follow either a Gaussian (σ) or an exponential (λ) distribution. Figure 2.4d plots the ACF power fitted with both exponential and Gaussian approximations. More typically, the exponential distribution is used:

$$P(\tau) = P_\lambda e^{-\lambda\tau}, \tag{2.6}$$

where P_λ is the maximum backscattered power. The constant λ (this should not be confused with the wavelength) is determined using a least-square fit and used to calculate the width of the spectrum from

$$width = \frac{c\lambda}{2\pi f_{radar}}. \tag{2.7}$$

Figure 2.4b graphs the magnitude of the fast Fourier transform (FFT) of the ACF shown in Fig. 2.4a. The vertical and horizontal lines indicate the velocity and spectral width calculated by equations (2.5) and (2.7) using the exponential approximation. Reasonable agreement between the Fourier spectrum and the FITACF estimates of the mean Doppler velocity and spectral width is seen.

As we mentioned earlier, there are some badlags when the ACF is computed. These are normally excluded. There are two types of badlags. The first type of badlags happens because the SuperDARN radar design is such that it is impossible to receive and transmit signals at the same time. Also, the radar must not be transmitting when it receives first echoes from a pulse 1 (Lag 0). Often, ACFs are bad when there is no Lag 0 data. The position of the gaps depends on the lag to first range, pulse length and the lag separation.

The second type of badlags is caused by strong scatter influence from 'unwanted' ranges. These are often referred to as cross-range noise. Originally, it was adopted the lag is 'bad' if the signal from an unwanted range is larger than $0.3 \times$ number of averages $\times$ power of wanted signal. For typical measurements with ~70 averages, this implies that a lag is bad if the signal power from unwanted range is 20 times more than

the one from the wanted range. Lately, a more stringent condition was implemented; a lag is bad if signal from unwanted range is simply stronger.

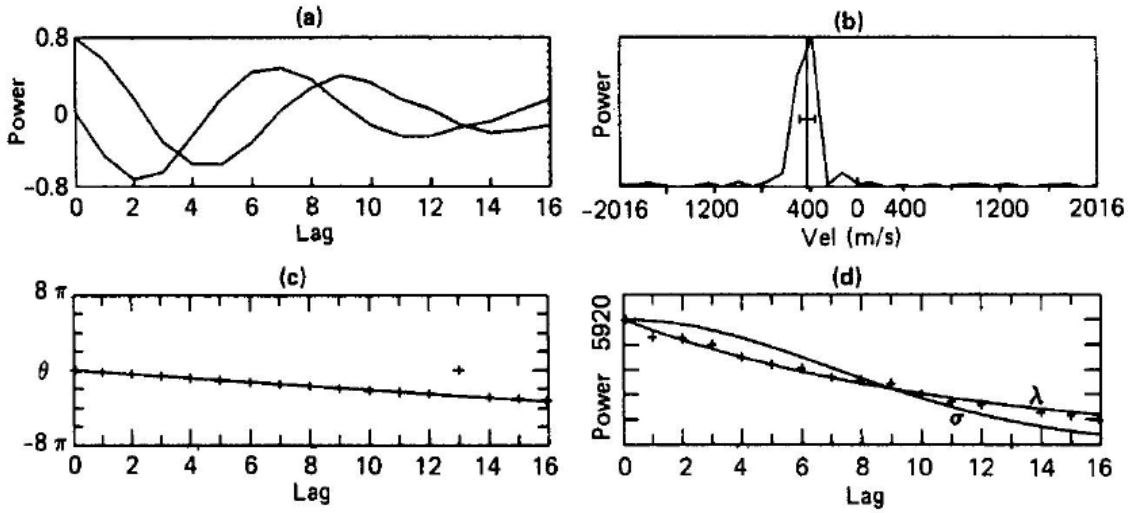

Figure 2.4. (a) Real and imaginary parts of the ACF. (b) Magnitude of the FFT of the ACF and the velocity (vertical line) and spectral width (horizontal line) obtained using FITACF algorithm. (c) Change of the phase angle with lag number. (d) ACF power decay for exponential (λ) and Gaussian (σ) least-square fits (Villain et al., 1987).

The SuperDARN data are often considered in combination with measurements by other instruments. In this kind of research, it is important to map properly the echo location. In this respect, one has to realize that the trajectories of HF radio waves in the ionosphere could be very complicated being affected by refraction. Figure 2.5 gives a sense of possible radio wave trajectories in the ionosphere that is represented by the International Reference Ionosphere (IRI) model calibrated on the density at the F region peak as measured by the ISIS-2 (International Satellite for Ionosphere Studies) topside sounder for one of the satellite passes from the mid to high latitudes (courtesy of R. Gillies, U of Saskatchewan). Figure 2.5b shows ray paths in the ionosphere for the 2-D density distribution shown in Fig. 2.5a and radar frequency of 11 MHz.

The radar rays at large elevation angles (black) are not strongly refracted and travel into the open space. While passing the ionosphere, some rays, such as the ray in red, can achieve perpendicularity with the magnetic field lines (these regions are denoted by red crosses along the red line), and if ionospheric irregularities happen to occur at these locations, returned echoes can be detected. Echoes received in this way are called ½F ionospheric echoes because backscatter occurs at the F region heights directly.

Starting from some smaller elevation angles (blue line), the rays would refract towards the ground. They then can be reflected back toward the radar. These echoes are called 1F ground scatter (GS). One can get ½E ionospheric and 1E GS echoes from the E region as well (green line). In a case of GS echoes, the beam can be reflected not only back toward the radar but also forward, toward the ionosphere. Rays that re-enter the E and F regions again can be backscattered. These kinds of echoes are referred to as one-and-a-half-hop (1½ hop) signals from the E and F regions.

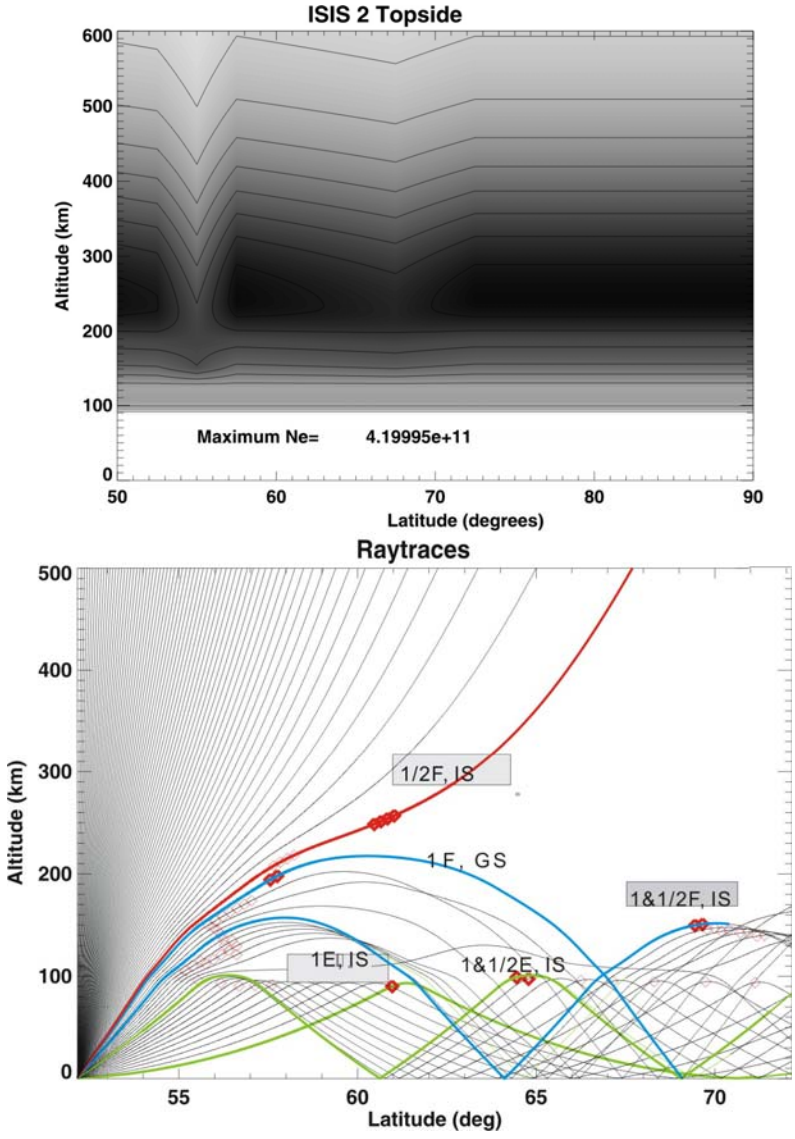

Figure 2.5. (a) 2-D electron density distribution according to the IRI model calibrated on the density at the F region peak measured by the ISAS-2 topside sounder for one of the satellite crossings from the mid to high latitudes. (b) Ray paths in the ionosphere for the density distribution shown in panel (a) and radar frequency of 11 MHz (courtesy of R. Gillies, U of Saskatchewan). Various modes of radar wave propagation are labeled.

2.2 OMTI all-sky camera at Resolute Bay

An all-sky camera is a standard instrument for monitoring aurora borealis. In this Section we introduce a camera that is part of a more complex instrument, the Optical Mesosphere Thermosphere Imager (OMTI) developed to investigate the dynamics of the upper atmosphere through night airglow emissions (Shiokawa et al., 1999). One of the main objectives for this instrument was detection of low intensity airglow variations such as the ones produced by atmospheric gravity waves. This capability of the OMTI is of particular importance for monitoring polar cap auroras because they are often of very low intensity. One of the targets of this Thesis is low intensity polar cap arcs.

The OMTI suite of instruments consists of an imaging interferometer, three all-sky cameras, three tilting photometers, and a Spectral Airglow Temperature Imager (SATI) installed in two containers. The imaging Fabry-Perot interferometer measures neutral wind vectors and temperatures at three different altitudes at the same time. Three cooled-CCD cameras are used as detectors. An all-sky airglow image is divided into three wavelengths, 557.7 nm (OI), 630.0 nm (OI), and 839.9 nm (OH)) by two dichroic filters, and then it passed through three band-pass filters, and received by the CCD cameras. The camera is successfully operated at the wavelengths of 557.7 nm and 630.0 nm and the reason for this is that the auroral spectrum has strong intensity in these lines.

We know that the aurora has many colors. Each color has a different wavelength. The brightest visible feature of aurora, the 'green light' at 577.7 nm, is due to the transition of an electron from the ^1S excited state to the ^1D state of atomic oxygen. Another commonly seen line, especially in the polar cusp and cap, is the 'red line' at 630.0 nm as the ^1D state relaxes to the ground state. The green oxygen line at 557.7 nm and the red line at 630.0 nm can be excited by the following processes:

$$O(^3P) + e \rightarrow O(^1S) + e' \quad (different\ \ energy),$$

followed by

$$O(^1S) \rightarrow O(^1D) + h\nu \qquad (557.7nm)$$

or

$$O(^1S) \rightarrow O(^3P) + h\nu \qquad (297.2nm)$$

For the red line, we have

$$O(^3P) + e \rightarrow O(^1D) + e^{/} \quad (different\ \ energy)\,,$$

followed by

$$O(^1D) \rightarrow O(^3P) + h\nu \qquad (630.0nm)\,,$$

where ^1S and ^1D have total electron spin s=0, and ^3P has spin s=1 (Vallance Jones, 1974).

The all-sky camera component of the system consists of the fish-eye lens (f = 24 mm) at the head of the camera. It has a wide field of view of almost 180^0. The shutter is controlled by a personal computer; the shutter is closed when daylight is detected by the CdS optical sensor. The filter wheel contains five 3-inch filters. The light received from the front lens passes through the telecentric optics and is focused on the thinned and back-illuminated 512×512 pixel cooled CCD detectors. The image data from the cameras are recorded on an optical disk/DVD and are uploaded to a computer network.

All equipment is set in two air-conditioned houses with several computers and a SUN workstation. The data from the instruments can be copied from remote stations through Internet, but for Resolute Bay, only DVD storage is available.

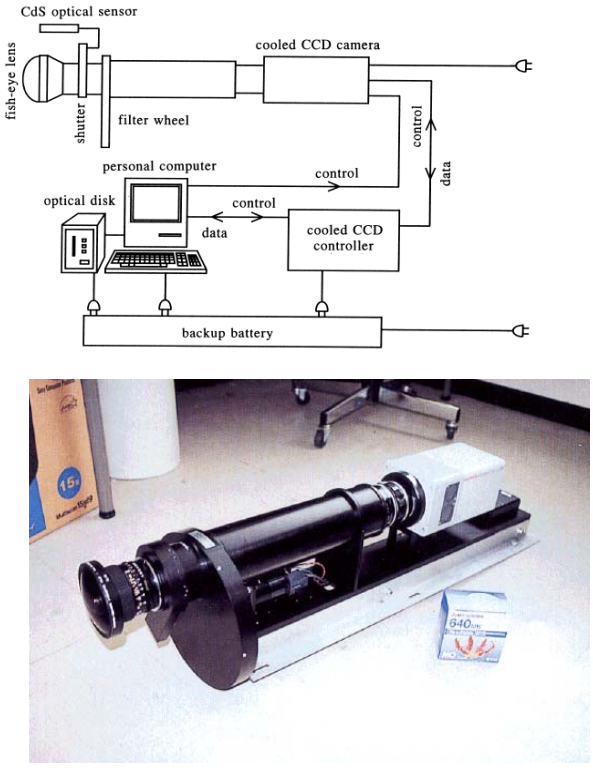

Figure 2.6. Schematic diagram and a photo of the Resolute Bay OMTI all-sky camera (Shiokawa et al., 1999).

The absolute sensitivities at the (256, 256) pixel (around the center of image) vary from 0.02 to 0.06 (counts/R/s) depending on the cameras and filters. For 557.7 nm camera, the sensitivities are 0.029, 0.044 and 0.049 (counts/R/s), and for 630.0 nm camera, the sensitivities are 0.038, 0.055 and 0.053. For aurora emissions with an intensity of 100 R, a 100-s exposure provides 300–500 counts per pixel. This amount is enough to infer airglow patterns, since the read-out noise and the dark noise of the CCD detector are 10 (counts/pixel/s) and far less than 1 (counts/pixel/s), respectively. The typical exposure times for 557.7 nm and 630.0 nm cameras are 105 s and 165 s, respectively.

2.3 Magnetometers

Magnetometers have been used for studies of currents in the close Earth's space for more than a century. They monitor variations of the Earth's magnetic field of time scales from fraction of a second to a daily variations. In this Thesis, data from several Canadian Array for Realtime Investigation of Magnetic Activity (CARISMA) magnetometers run by the University of Alberta as a part of the Canadian Geospace Monitoring mission (supported by the Canadian Space Agency) and Natural Resources of Canada (NRCan) Geomagnetic Laboratory, Ottawa will be used. In this Section, we give a brief introduction into magnetometer measurements.

Magnetometers measure components of the Earth's magnetic field, X, Y and Z. These are usually North, East and down directions, in geographic coordinates. There are two major types of magnetometers: one for measurements of relative changes of the geomagnetic field (fluxgate magnetometer) and the other one for measurements of absolute values of the geomagnetic field (proton magnetometer). The latter are more expensive and require more field work so that these measurements are only done at a number of permanent observatories (at some NRCan stations). CARISMA magnetometers are designed to measure quite fast variations since data are digitized with the rate of 8 samples per second. For the WEB distribution, the CARISMA data are averaged to one measurement in 5 s. The NRcan magnetometer data are usually 1-min averaged values. We will be using data collected with fluxgate magnetometers.

A fluxgate magnetometer works as follows. First of all, structurally, it consists of two small ferromagnetic cores wrapped by two coils of wire, Fig. 2.7.

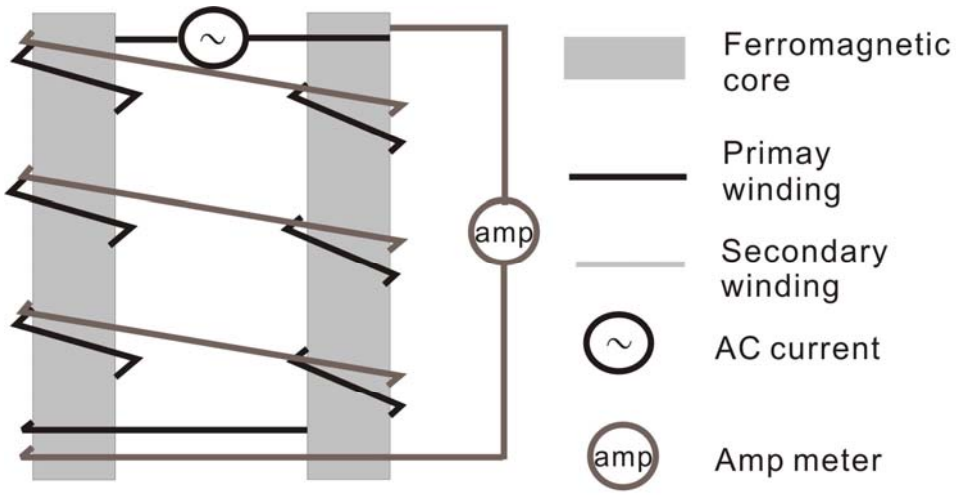

Figure 2.7. A scheme illustrating principle of fluxgate magnetometer operation.

The cores are placed parallel to each other and are considered to be the primary core. The direction in which the current from an external generator flows in windings is opposite, so that the magnetic fluxes created in the cores are opposite and the total flux is zero in absence of the external magnetic field. The current that is passed trough the primary coils is large so that the ferromagnetic material hysteresis saturation level can be easily achieved. A secondary loop, the sensing loop, is wrapped around both cores. By measuring the signals in the secondary loop, we can measure the magnitude of external magnetic field.

Figure 2.8 explains the details of how a fluxgate magnetometer works. The high-frequency sinusoidal current (50-1000 Hz) is sent to the primary cores, Fig. 2.8a. Because of the saturation effect, this sinusoidal signal drives each core to saturation as it goes through a magnetization hysteresis loop. One effect to keep in mind is that when the saturation is achieved, the change of the total magnetic flux through the cores is zero and so is the voltage in the sense loop. The signal in the sense loop due to just one core is shown in Fig. 2.8b; one can notice that the waveform is rather of a trapezoidal shape. The second effect to consider is that in absence of the external (Earth's) magnetic field, the cores saturate at the same time, as shown in Fig. 2.8c, and no signal is detected in the sense coil. In the presence of the external magnetic field parallel, for example, to the

core 1, the core 1 would get out of the saturation and return back to saturation earlier than the other core (as shown in Fig. 2.8d, top line) than the other core (bottom line in Fig. 2.8d). This means that there would be two short periods for which compensation of fluxes due to cores does not happen and two spikes in voltage of the sense coil would occur. For these periods, the total flux is changing as shown in Fig. 2.8e. Notice that there are two spikes in voltage for one cycle of the external generator implying that the frequency of the response is doubled as compared to the input frequency, compare Figs. 2.8a and 2.8f. The output voltage of the sense coil is measured. Fluxgate magnetometers usually work on a compensation principle: additional voltage is sent to compensate any voltage created in the sense loop. After appropriate calibration and orientation on a site, a fluxgate magnetometer collects data that are often transmitted to users via Internet.

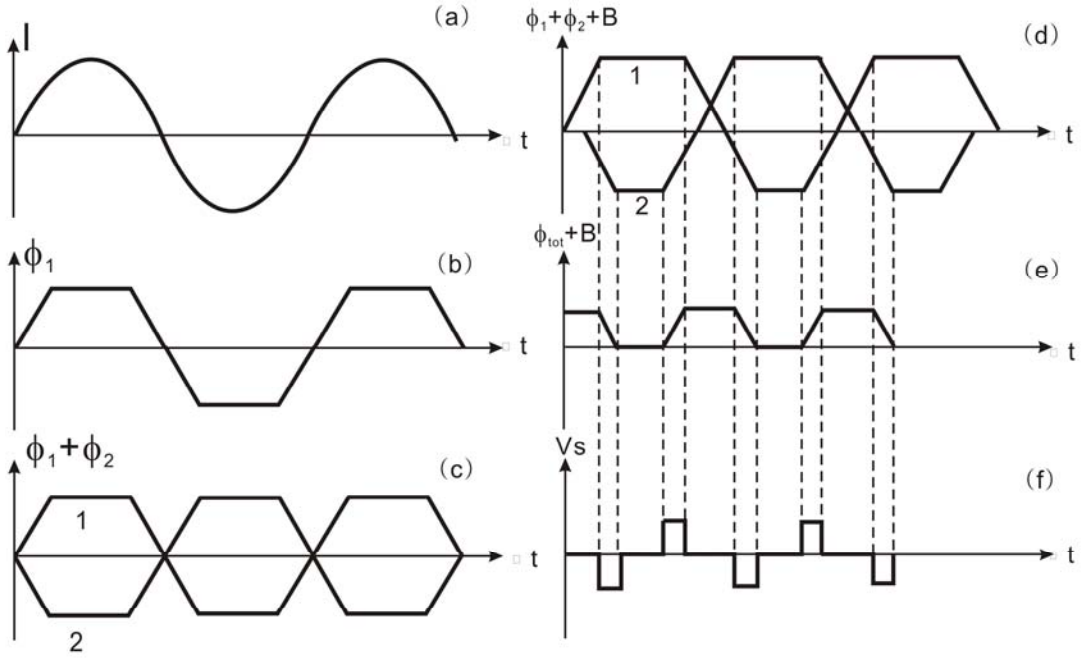

Figure 2.8. Diagrams explaining the principle of fluxgate magnetometer operation.

Table 2.2 gives information on locations of magnetometers used in this Thesis. Exact positioning of these magnetometers within the field of view of the SuperDARN/ PolarDARN radars will be shown later in Chapter 4, Fig. 4.1.

Table 2.2: Magnetometer locations

Station	Lead organization	Code	GG(ºN) Lat	GG (ºE) Long	CGM(ºN) Lat	CGM(ºE) Long
Rankin Inlet	CARISMA	RKN	62.82	267.89	72.91	-25.34
Taloyoak	CARISMA	TALO	69.54	266.45	78.95	-31.05
Cambridge Bay	NRCAN	CBB	69.12	254.97	77.31	-51.27
Resolute Bay	NRCAN	RES	74.69	265.11	83.57	-43.50

2.4 Summary

In this Chapter, an introduction to the principles of operation of three major instruments to be used in this Thesis is given. These are the PolarDARN HF radar for detection of radar echoes, all-sky camera for monitoring the auroral luminosity distribution within the radar field of view and fluxgate magnetometer for detection of geomagnetic field perturbations associated with occurrence of radar echoes and optical forms.

CHAPTER 3

RANKIN INLET RADAR IONOSPHERIC ECHO OCCURRENCE RATES: A COMPARISON WITH SASKATOON AND HALLEY OBSERVATIONS

Since the start of operation in 2006, the Rankin Inlet (RKN) radar consistently outperforms other radars of the SuperDARN network in terms of echo occurrence. This is evident from a simple comparison of time plots for various radars on the main SuperDARN website at http://superdarn.jhuapl.edu. The more recently installed Inuvik (INV) radar, paired with the RKN radar, seems to show high echo occurrence rates as well. Although this fortunate circumstance has been publicized, for example at the Annual SuperDARN workshops, the radar echo occurrence rates have not been investigated in a comprehensive way. More importantly, there is no answer to the basic questions as to why this happens and what one should expect in terms of echo occurrence in future when the Sun's activity will increase. In this Chapter, an attempt has been made to investigate some aspects of the question. We first quantify the RKN radar echo occurrence and then compare the numbers with the ones (obtained in a similar way) for two other SuperDARN radars, at Saskatoon (SAS) and Halley (HAL). We compare observational conditions for these radars in a quest to understand the reasons for differences in radar echo detection rates.

3.1 Review of previous SuperDARN work

Ruohoniemi and Greenwald (1997) were the first who investigated echo occurrence for SuperDARN-type HF radars. They considered long-term (1988-1993)

trends for the Goose Bay radar. The echoes were found to mostly occur within a band of latitudes 65^0-75^0 with much larger rates on the nightside and much lower rates between 12:00 and 14:00 MLT. At the dusk and dawn, echoes occurred within the auroral oval while in the midnight and noon sectors, echoes were seen often well equatorward and poleward of the auroral oval boundaries. With a magnetic activity increase, the maximum rates became smaller but echoes were detected over a larger range of latitudes, both equatorward and poleward of the auroral oval. The authors concluded that the auroral zone echoes occur more frequently during winter of the solar cycle maximum. The lack of echoes during summer was interpreted as an effect of solar radiation (for the sunlit ionosphere) smoothing out the plasma gradients and thus reducing the production of irregularities through the GD instability. Reasons for seasonal variation have not been discussed.

More frequent echo occurrence during winter was also reported by Milan et al. (1997) who investigated 20-month long statistics for the Co-operative UK Twin Located Auroral Sounding System (CUTLASS) radars in Finland. These authors concluded that the electron density in the ionosphere contributes strongly to the echo appearance at a specific range. They pointed out that proper amount of refraction is a very important factor leading to preferential time sectors and radar ranges for echo detection. This result implies that particle precipitations within the auroral oval provide favorable conditions for echo occurrence while seasonal changes of the ionosphere due to sunlight are less important.

Ballatore et al. (2001) investigated cumulative echo occurrence rates for 6 northern hemisphere SuperDARN radars for 1997-1998. This period is close to the solar cycle 23 minimum. Overall, echoes were more frequently seen at latitudes of 65^0-80^0 with the rates of ~7% during winter, ~5% during equinox, and ~3% during summer. These authors also investigated relationship of the echo occurrence and the IMF and parameters of the solar wind. It was found that there is a statistically significant correlation between the echo occurrence and the negative B_z component of the IMF, independent of the season. Also, no clear correlation with the solar wind density and velocity was found.

More systematic investigation of F region echo occurrence has been undertaken by Hosokawa et al. (2001) who considered data from six Northern hemisphere radars operated in 1996-1998 (again, close to the solar cycle 23 minimum) and showed that echoes mostly occur on the dayside at latitudes of 70^0-75^0 corresponding to the poleward edge of the auroral oval or even poleward of it. In other MLT sectors, echoes were collocated with the auroral oval. It is interesting to note (this was not mentioned in the original paper) that the two Iceland radars (Pikkvibaer and Stokkseyri), whose FoVs are oriented azimuthally, detected a significant amount of echoes not only at the auroral oval latitudes but also from within the polar cap, at MLAT=70^0-80^0. Such echoes were preferentially seen in the afternoon sector all the way until early morning. Hosokawa et al. (2001) focused on dusk echoes seen well equatorward of the auroral oval. These were related to the mid-latitude trough.

Parkinson et al. (2003) considered one year (1999-2000) of echo statistics for the Australian SuperDARN radar at Bruny Island. The echoes were found to dominate in the midnight sector at, and somewhat poleward of, the auroral oval. With the Kp index increase, more echoes were seen equatorward of the auroral oval. It was noticed existence of a March (fall) maximum though the overall seasonal variation was apparently not significant.

Koustov et al. (2006) investigated occurrence of King Salmon HF radar echoes near the equatorward edge of the auroral oval and reported preferential occurrence in the dusk-midnight sector. The Hokkaido mid-latitude radar also detects this sort of echoes (Koustov et al., 2008).

On the poleward side of the auroral oval, Fiori et al. (2009) recently presented data on the RKN radar echo occurrence for two seasons, winter and summer and in all radar beams. It was shown that the radar sees echoes mostly in radar gates 0-25 (ranges <1500 km) with the rates up to ~40%. Winter data showed echo appearance at larger ranges. All radar beams showed comparable occurrence rates. This study, however, was limited in terms of data involved (as this topic was not its major target) and the data presented were a first quick look at the RKN occurrence rates.

3.2 Rankin radar location and geometry, differences with other SuperDARN radars

In the original design of the SuperDARN experiment, it has been envisioned that HF radars would be placed around the globe with FoVs covering, first of all, latitudes of the auroral oval (Greenwald et al., 1995). This was an extension of the original idea implemented for the Scandinavian Twin Auroral Radar Experiment (STARE) VHF radars in Northern Europe. Another idea was to use twinned radar systems with common FoVs so that the velocity data in one spot but from two distinctly different directions would be "merged" to infer the total vector of the plasma drift at the F region heights. Observations in all longitudinal sectors and at about the same magnetic latitudes have been targeted. Practical implementation of the original idea has been hampered by a lack of funding and slow network expansion into Russian territory in the Northern Hemisphere and very limited available places and considerable expense in the Southern hemisphere. Some single radars have not been paired so far, but this weakness has been alleviated by implementation of the Potential Fit technique for producing the global plasma convection maps. Figure 2.1 shows that most of the SuperDARN radars are positioned to have good coverage of the auroral oval latitudes of 65^0-75^0.

It is important to note that although the "auroral zone" SuperDARN radars have about the same FoVs in terms of geomagnetic latitudes (as they all were targeting the auroral oval), the geographic locations of the radars is not the same. Most of the radars are positioned at relatively low geographic latitude, equatorward of the auroral oval. This is to ensure that HF radio waves, while propagating to the scattering volume, would have opportunity to refract and meet the orthogonality condition with the magnetic field lines. One clear exception is the Halley radar in Antarctica. It is located well above the polar circle (~63^0) implying that significant periods of the year the radar works in complete darkness or under complete sunshine 24 hours a day. This is in contrast to other radars whose observations do not have complete darkness or complete sunshine conditions all year around.

Over the years of SuperDARN operation, it became clear that observations equatorward of the auroral oval are interesting scientifically and important for various

space weather applications, and HF radars were installed at Wallops Island, Hokkaido and Blackstone were put online. A new USA initiative (2009) would allow construction of eight more low-latitude HF radars.

The installation of the PolarDARN radars at Rankin Inlet and Inuvik was aimed at covering very high magnetic latitudes, indicating the beginning of "poleward expansion" of the SuperDARN network. The radars were expected to monitor plasma convection at magnetic latitudes above 80^0. For the RKN radar, the geographic latitude is high but it is still below the Arctic Circle implying that there is some photoionization to add refraction along the incident ray paths.

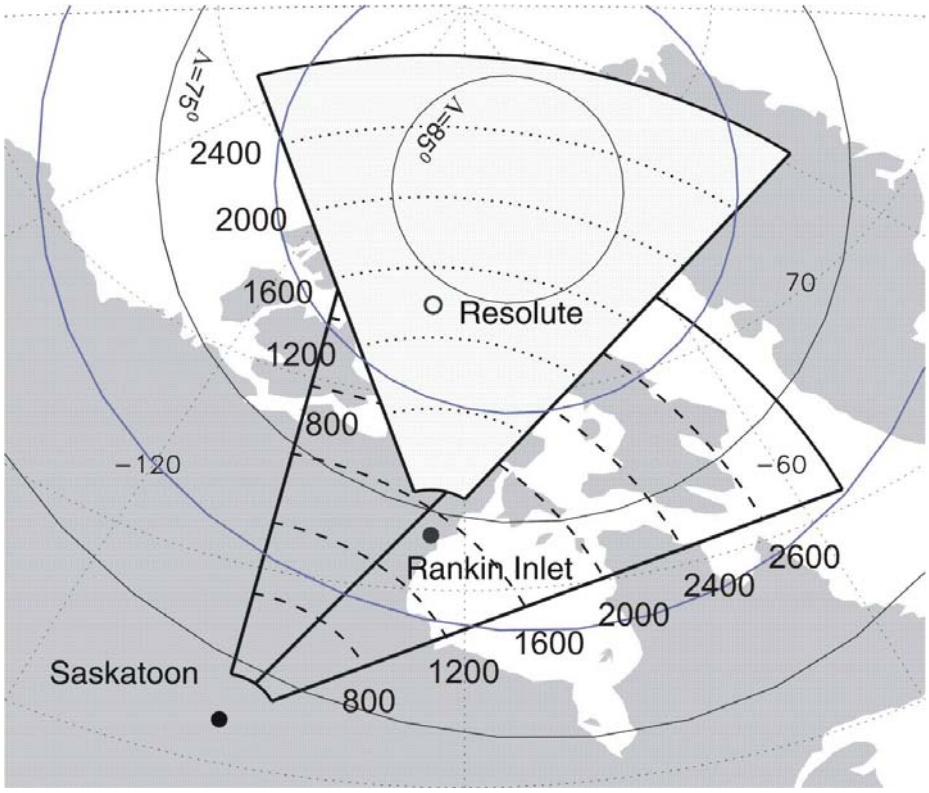

Figure 3.1. FoVs of the Saskatoon and Rankin Inlet PolarDARN radars for ranges 400-2800 km. Range marks for each radar are shown at the edge of respective FoVs. Resolute is an observatory where a number of instruments are located. Shown also are the lines of magnetic latitudes of 60^0, 70^0 and 80^0.

In this study, we decided to look at echo occurrence rates for the RKN radar and compare them with data for 2 other radars, Saskatoon and Halley. The objective here is

that Saskatoon radar monitors ionospheric echoes in the same MLT sector as the RKN radar, but is capable of seeing different range of latitudes, from ~ 65^0 to 85^0. We illustrate relative locations of the RKN and SAS radar FoVs in Fig. 3.1.

For the SAS radar, the geographic latitude of a point is smaller than its geomagnetic latitude. This is similar to the RKN conditions of observations. For the HAL radar, Fig. 2.1, a point within the FoV has much larger geographic latitude than geomagnetic latitude. This implies totally different observational conditions in terms of solar illumination effects and propagation conditions.

The radars have significant difference in terms of magnetic latitudes monitored. To illustrate this, we compare the radar FoVs with the typical locations of the auroral oval, Fig. 3.2. In Fig. 3.2 we show echo velocity maps for four typical periods (dusk, midnight, dawn and noon) for quiet conditions (Kp=0). One specific day, 07 November 2007, of operation has been selected for RKN and SAS, and a different day, 11 October 2006, for HAL, as not many echoes were detected on 07 November 2007. One can see that SAS sees echoes in the vicinity of the auroral oval through the direct mode for the first three time sectors. In the noon sector, as the oval is located closer to the North Pole, ionospheric (color) echoes just poleward of the oval are often received through 1½ propagation mode. For more disturbed conditions, the oval expands but the morphology of echo occurrence and propagation modes are often the same.

The RKN radar is located, most of the time, near the poleward edge of the auroral oval and the echoes received are clearly coming from within the polar cap, consistent with the objective for the radar installation. One can notice that the oval is more distant from the radar on the dayside, a geometry similar to that for the SAS radar.

The HAL configuration is very similar to that for the SAS radar. For the event considered, one can notice that no echoes are seen at noon hours. It is a common feature for HAL that echoes are seldom detected near magnetic noon.

For the statistical analysis below we decided to consider (for each radar) only 3 beams directed almost perpendicular to L shells. These beams were 6-8 for RKN, 2-4 for SAS and 7-9 for HAL. Although we did not expect that consideration of all beams would significantly change our conclusions, still the radar FoVs are oriented somewhat

differently with respect to the magnetic L shells and we wanted to avoid any uncertainty that might be related to this factor.

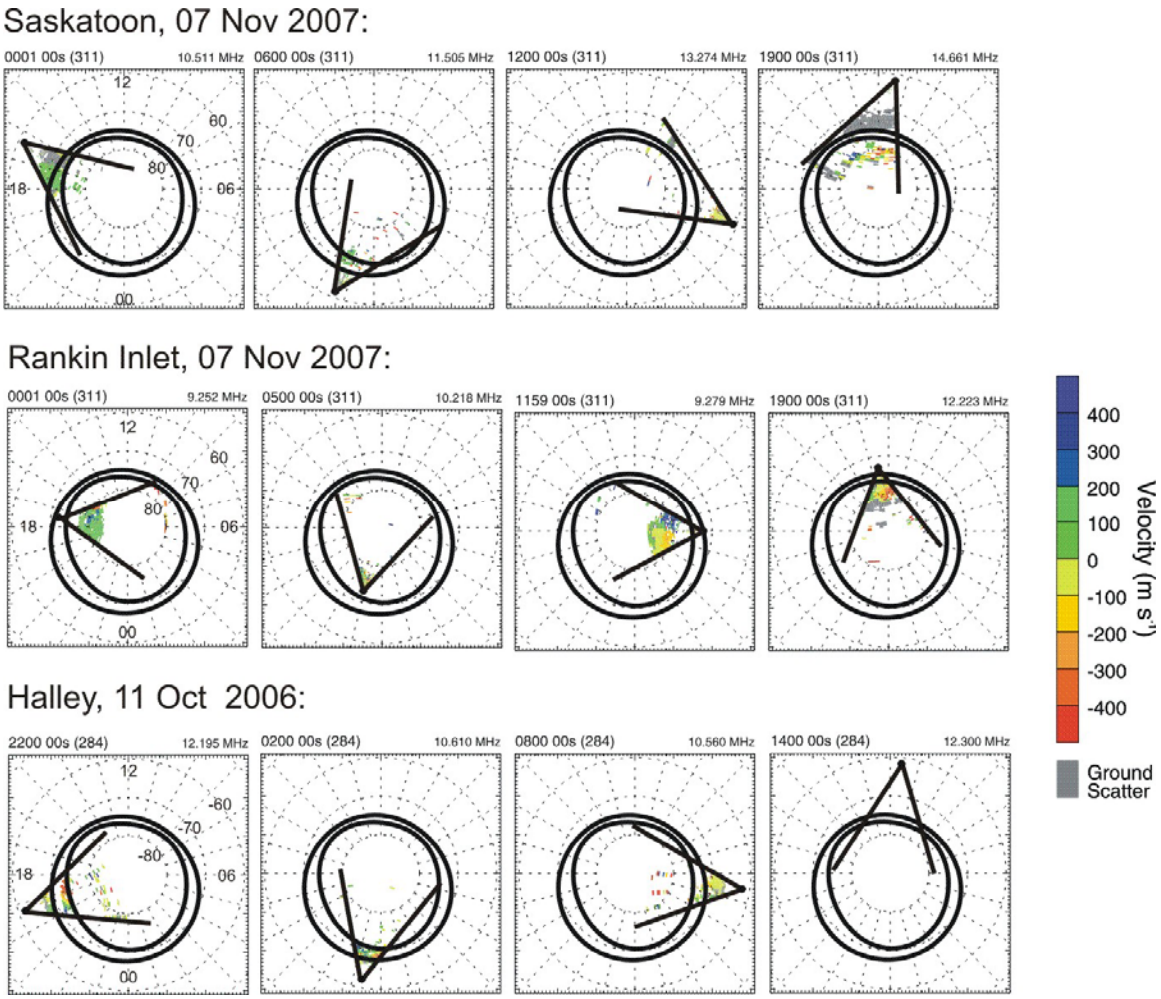

Figure 3.2. Echo velocity map in MLT-MLAT coordinates for the RKN (top), SAS (middle) and HAL (bottom) radars with respect to the quiet auroral oval (Kp=0), thick line. Four different UT times were selected to show echo locations in the evening, midnight, morning, and noon sectors. On each panel: top (bottom) is 12 (00) MLT, left (right) is 18 (06) MLT, circles are lines of magnetic latitudes of 60^0, 70^0 and 80^0.

To compute echo occurrence rate we adopted a straightforward scheme similar to Koustov et al. (2004). For each radar beam and gate, a value of 1 was assigned if an echo occurred and a value of 0 if it did not while the radar was operational and were able to detect echoes. This is in departure from the approach of Ruohoniemi and Greenwald (1997) who applied a more sophisticated method of echo occurrence estimate; they

assumed that, for practical derivations of the convection, data from a number of cells would be treated as received from one point and so, for a selected location, echo occurrence in neighboring places would be counted. The result is that their echo occurrence rates are higher than those reported by Koustov et al. (2004).

3.3 Results

One full year of operation, 2007, was selected for the comparison and averages over every calendar month were computed. The results were plotted in magnetic local time-magnetic latitude coordinates. Below we consider data for each of the radar and for some months selected to represent various seasons (other months of each season showed similar results).

3.3.1 Rankin Inlet statistics

Figure 3.3 shows echo occurrence rates at various magnetic latitudes and MLT times in the form of a color plot with the scale shown on the right. Four seasons are represented by the data for winter (January), summer (June), spring equinox (March) and fall equinox (September). One striking feature is that the rates can be as high as 60-70% in the midnight sector (red color on the winter and fall plots). Another obvious feature is that the echoes continuously occur within the band of latitudes 75^0-80^0. The second ~5^0 band of enhanced echo occurrence is at latitudes 80^0-85^0. We have to say that echoes have been seen at all latitudes within the RKN FoV; the background color in Fig. 3.3 does not mean a complete absence of echoes.

In terms of a seasonal trend, overall, echoes are more frequent during fall equinox although the rates are only slightly larger than for the winter observations (less red color). The lowest rates are seen during summer. We note that the rates during spring equinox are lower than during both fall equinox and winter. If one considers only high-latitude observations, at MLAT > 80^0, echoes occur preferentially during equinoxes (as indicated by additional “islands” of echo occurrence in the midnight sector).

In terms of the magnetic latitude, one can notice that during winter and equinoxes, echoes at very high latitudes, MLAT > 80^0, are seen. These echoes seem to be more frequent during equinoxes although one can notice such echoes for winter observations (noon-afternoon sectors) as well. There is a difference between the winter and equinox observations at high latitudes in a sense that the high-latitude echoes are more frequent during the daytime in the winter and during the nighttime in the equinoxes.

In terms of the magnetic local time, echoes are more frequent between ~06:00 and ~15:00 MLT for all seasons, and significant amount is observed between 18:00 and 01:00 MLT during all seasons but summer. One can notice that rates are somewhat depressed between 01:00 and 06:00 MLT (with perhaps smaller effect for the fall observations).

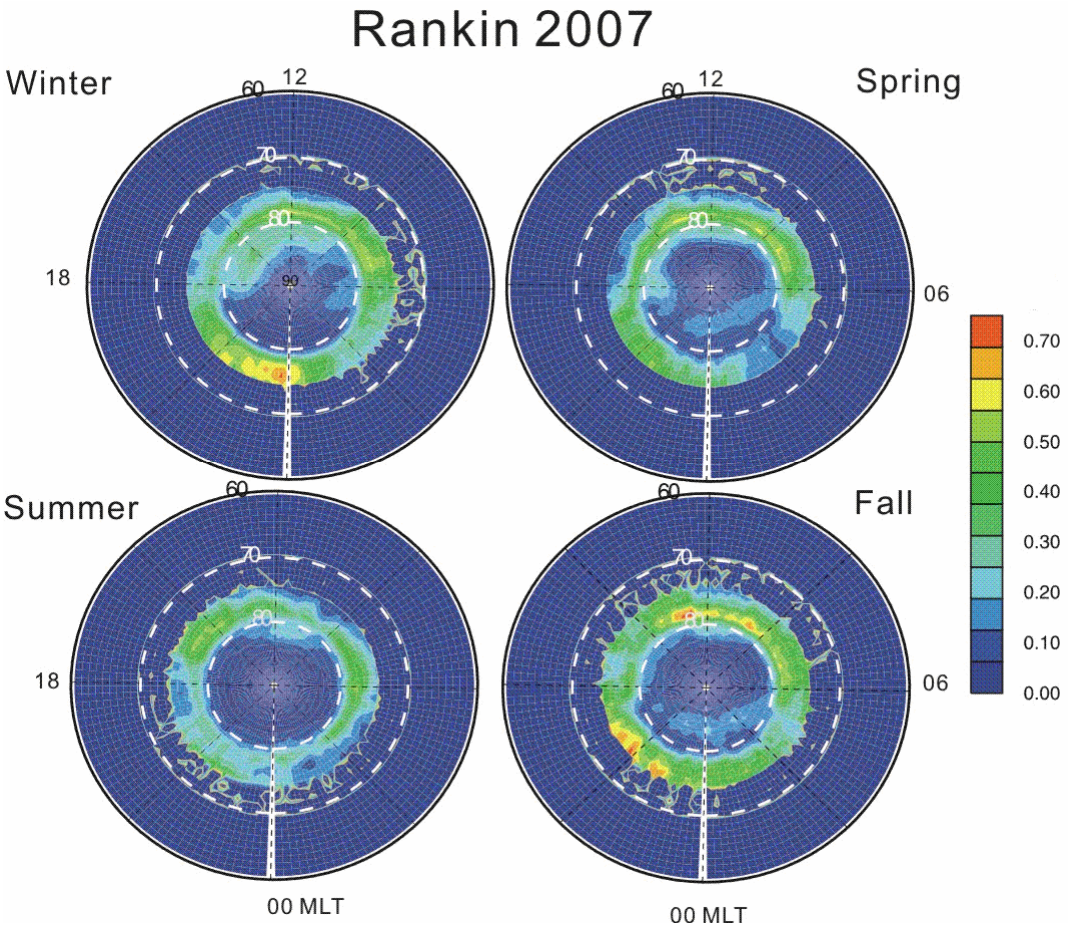

Figure 3.3. Echo occurrence rates at Rankin Inlet for winter (January 2007), summer (June 2007), spring equinox (March 2007) and fall equinox (September 2007).

To assess the color plot of Fig. 3.3 in a quantitative way we 1) plotted occurrence rate versus magnetic latitude at 4 typical MLT times and 2) computed average occurrence rate within 2 bands of latitudes over 24 hours. Figure 3.4a presents "slices" of the occurrence plot of Fig. 3.3 for MLT=3, 12, 17 and 23. In the midnight and morning sectors (23 MLT and 03 MLT), echoes are much more frequent at latitudes 75^0-78^0 although the rates are ~2 times larger before midnight. In the noon sector (12 MLT) and especially in the dusk sector (17 MLT), the maximum echo occurrence is seen at larger latitudes (by ~1^0-2^0) and a second peak is seen at much larger latitudes of >80^0. This second peak seems to be well separated from the first one.

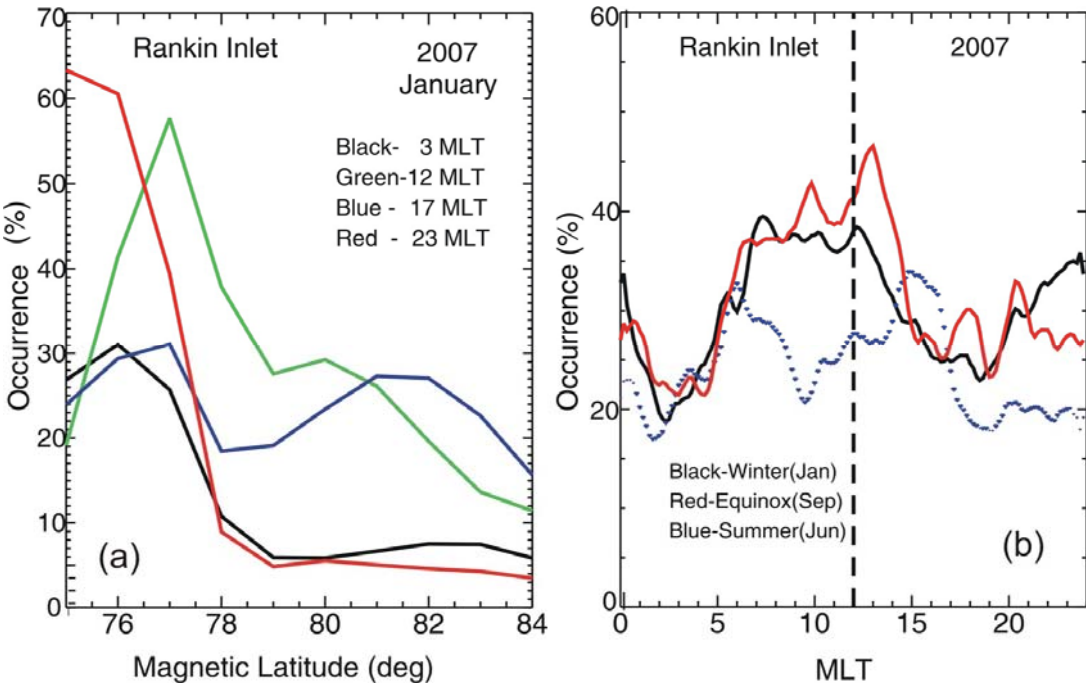

Figure 3.4. Rankin Inlet ionospheric echo occurrence rate (a) versus magnetic latitude for MLT=3, 12, 17 and 23 and (b) versus magnetic local time for winter, equinox and summer.

Occurrence rate variations with magnetic local time are presented in two ways. First, we give average rates, over the entire day, for two bands of enhanced echo occurrence and for all seasons, Table 3.1. For the band of the best occurrence, the average rates over a day are as high as 33.8% with slightly smaller values for summer and spring. For the other (more poleward) band, the rates go down dramatically, by a

factor of ~3 for winter and equinoxes and by a factor of ~8 for summer. Averaged occurrence rates over 10^0-band of latitudes is about 20% for all seasons. As was mentioned, there is some diurnal variation of echo occurrence in Fig. 3.3. To illustrate it, we plot in Fig. 3.4b the average rates for latitudes 75^0-80^0 against MLT for winter, fall (spring shows similar trends) and summer. Winter and fall data show a double peaked curve with maxima at noon and midnight. Interestingly enough, the summer data show something different. First, there is no midnight maximum, the distribution is rather flat. Second, there is no noon maximum; instead two maxima are seen at dusk and dawn, and echoes are not often seen in the noon sector.

Table 3.1. Echo occurrence rates for the RKN radar within 5^0 and 10^0 bands of latitudes with highest rate. Data for one month of each season are considered.

Radar	Magnetic Latitudes, deg	Ionospheric Echo Occurrence Rate, %			
		Winter	Summer	Spring	Fall
Rankin	76-80	33.5	26.1	30.7	33.8
	81-85	12.4	3.2	8.7	7.1
	76-85	23	14.7	19.7	20.5
Saskatoon	63-67	10.9	6.6.	8.5	10.0
	70-74	2.4	1.3	2.3	2.3
	76-80	5.5	4.2	7.2	6.4
	63-80	6.3	4.0	6.0	6.2
Halley	63-67	1.23	0.72	1.35	0.95
	69-73	0.89	1.06	2.16	3.67
	63-73	1.1	0.89	1.76	2.31

The fact that the RKN radar detects echoes well above the main latitudinal band (75^0-80^0) is very interesting. The main band corresponds to radar ranges of <800 km while the high-latitude band corresponds to radar ranges of 1000-1300 km (compare Figs. 3.1 and 3.3). We believe that the echoes in the main band are received through the direct propagation mode while the high-latitude ones through the 1½ hop propagation mode. This opinion is supported by comparable elevation angles for the bands on the dayside for winter (data are not shown here). Fall data show that elevation angles for high-

latitude band are somewhat larger than the elevation angles for echoes in the low-latitude band. We note that the highest occurrence rates are detected at lowest ranges; here the echoes can come from both E and F regions. From the plots presented, one cannot decide which part represents F region echoes and which part represents E region echoes.

3.3.2 Saskatoon statistics

Figure 3.5 presents echo occurrence rates for the SAS radar with a plot similar to the one for RKN, Fig. 3.3. The only difference is the scale; the maximum values here are 50% versus 70% for the RKN radar.

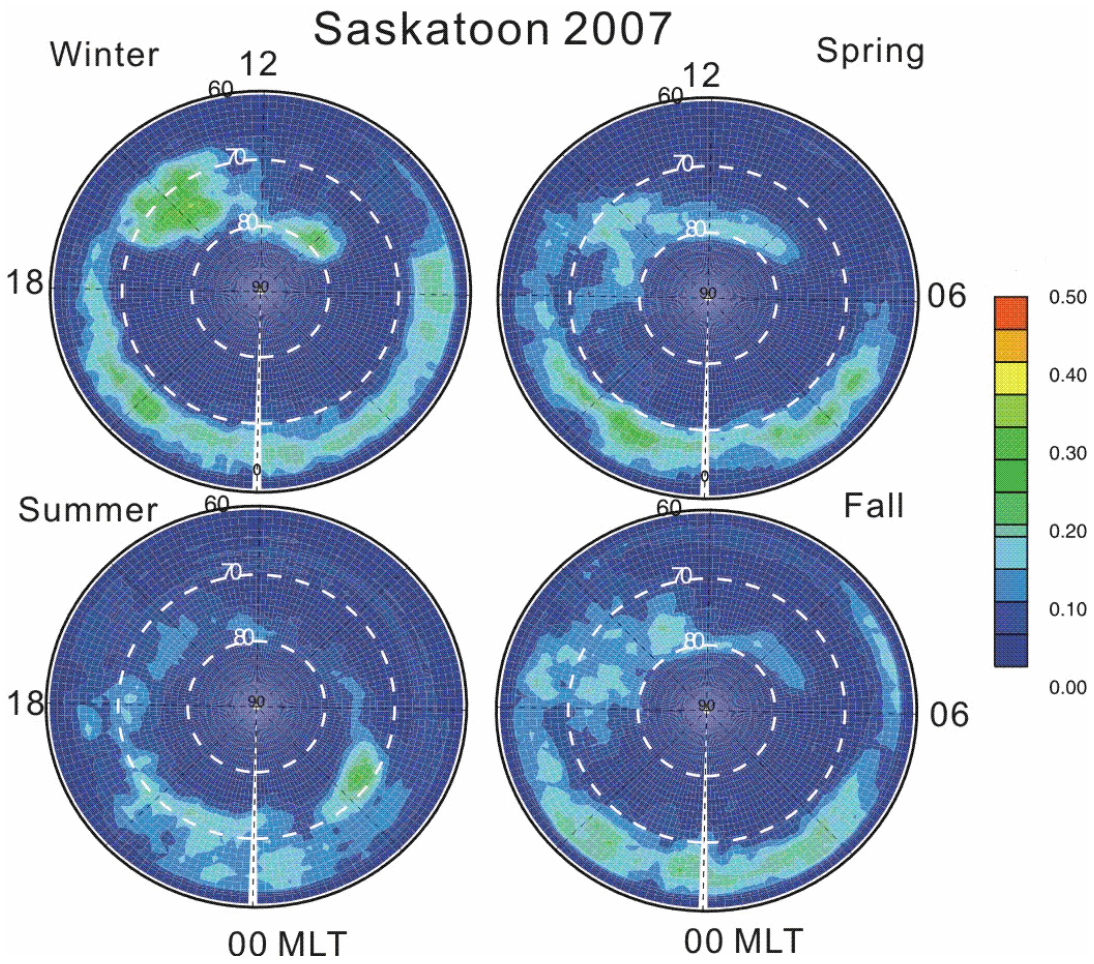

Figure 3.5. Echo occurrence rate at Saskatoon for winter (January 2007), summer (June 2007), spring equinox (March 2007) and fall equinox (September 2007).

One can notice that the pattern of echo occurrence is more complicated here. First of all, there no is a clear "belt" of enhanced occurrence as all seasons show a rate decrease between 06:00 and 12:00 MLT for latitudes of 60^0-70^0. The largest occurrence rates are at latitudes of 65^0-70^0. We assessed the SAS echo occurrence rates in three 5^0-bands, 63^0-67^0, 70^0-74^0, and 76^0-80^0. The first two bands characterize echo occurrence for the ½ propagation mode while the last band reflects echo detection through 1½ propagation mode. The typical occurrence rates over all these latitudes are ~6% which is lower than the one for the RKN radar by a factor of ~3.

In terms of seasonal dependence, one can conclude that echoes are more frequent during winter. Equinox measurements show somewhat smaller overall rates. Also, there is not much of a difference between spring and fall observations. The smallest rates were seen during summer.

In terms of magnetic latitudes, one can isolate echoes at latitudes of 65^0-70^0 as the ones related to the auroral oval and the ones at latitudes $>70^0$ that could be related to the cusp/cleft area on the dayside of winter and equinoxes observations and on the poleward nightside edge of the auroral oval for summer observations. There is no doubt that daytime echoes at magnetic latitudes ~80^0 are detected through 1½ (F region) propagation mode. Echoes at the lower latitudes are very likely received through direct mode. Huber (1999) presented Saskatoon data on elevation angles that support the latter judgment on the propagation modes.

In terms of magnetic local time, echoes are more frequent on the dayside during winter and on the nightside during equinoxes and summer. On the nightside, echoes are limited to smaller sector during summer (20:00-04:00 MLT) as compared to other seasons (17:00-06:00 MLT). We should note that the presented plots are very much similar to the ones reported in the past by Huber (1999) for observations in 1997.

One can notice some minor changes in occurrence rates for the SAS radar at various latitudes, Table 3.1. The seasonal variation of SAS echo occurrence is not very strong with summer showing slightly larger rates.

3.3.3 Halley statistics

Figure 3.6 presents echo occurrence rates for the HAL radar in the same format as the data for the RKN radar in Fig. 3.3. One has to note that the maximum rates here are even less than for the SAS radar, ~20%. As this radar operates in the Southern hemisphere, winter (summer) observations are represented by the data for June (January). The equinoxes have been "flipped" as well; spring (fall) is represented by September (March) observations. We should note that a quick scan through the HAL 2007 data showed significant amount of noise indicating deterioration of data quality. However, we performed analysis of Halley data for 1996 and 1997 (11 years earlier) and found that the main pattern of echo occurrence in MLT and MLAT is the same, although the absolute values of the rates were slightly higher than 2007.

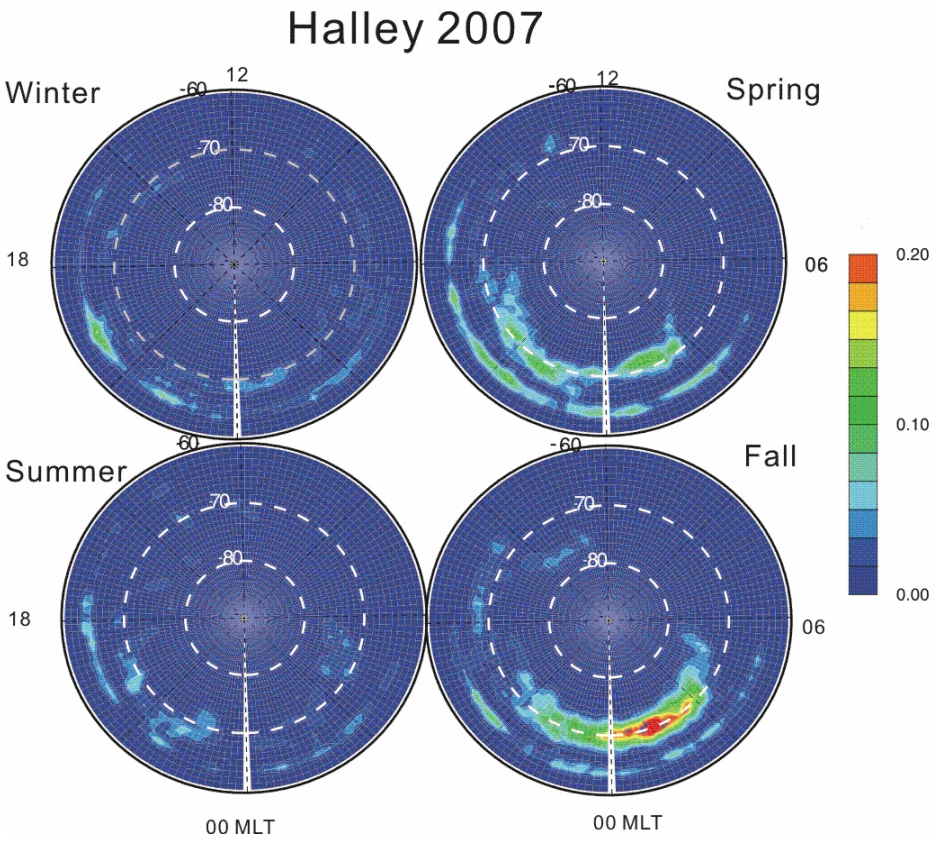

Figure 3.6. Echo occurrence rate at Halley for austral summer (January 2007), austral winter (June 2007), austral fall equinox (March 2007) and austral spring equinox (September 2007).

The most striking feature of Fig. 3.6 is absence (very low rates, as the color does not represent the value quite well) of echoes during noon hours for all seasons and at all latitudes. The only exception is a small "patch" at 78^0 and 15 MLT during the fall equinox. The echoes are seen on nightside within two bands of latitudes. Fall and spring measurements show the largest rates; the fall rates are significantly larger than the spring ones. We note here that the same effect was seen at RKN, but the months of the maxima are quite different. The other striking feature of Fig. 3.6 is that there are two clear "bands" of echoes for nighttime observations. This effect is less obvious for summer. It is very likely that these "bands" reflect occurrence of E and F region echoes received through ½E and ½F propagation modes. For Halley, one cannot notice much of a difference between summer and winter as the rates are fairly low for both seasons.

Perhaps some conclusions can be drawn from the average (over 24 hours) rates presented in Table 3.1. Here we show occurrence rates for two 5^0 bands of echo detection, 63^0-67^0 and 69^0-73^0. One can see that winter and summer show ~1% of occurrence. This is well below that observed during equinoxes, 2-3%.

3.4 Discussion

Whether an ionospheric HF echo is detected depends on several factors (e.g., Danskin et al., 2002). These can be split onto two categories: (1) factors related to radio wave propagation and (2) factors related to the irregularity generation and radio wave scattering.

There is no question that decameter irregularity presence in the ionosphere is a number one factor. Without irregularities, no ionospheric coherent echoes would be detected. As mentioned in Chapter 1, decameter irregularities are very likely produced in the high-latitude F region through the GD instability that requires enhanced density gradients and electric fields. Diffusion processes, however, prevent the GD instability development. Diffusion can be enhanced through formation of strongly conducting E region layer on those magnetic flux lines where the F region irregularities are to be developed. Another effect is smoothing out of the density gradients by sunlight.

Currently available measurements do not allow one to conclude on the exact regions (in time and space) with preferential conditions for decameter irregularity production. We proceed here with an idea that the auroral oval roughly delineates the areas with enhanced electric fields and more frequent occurrence of strong plasma gradients. If the assumption on strong plasma gradients seems to be reasonable (because of frequent particle precipitations happening here), the assumption on the electric field requires more explanation. Satellite measurements do show a significant electric field decrease equatorward of the auroral oval, with the only exception for cases of the polarization jet development (Koustov et al., 2006). Satellites, crossing the polar cap, do show occasional strong electric fields poleward of the auroral oval, but enhanced flows at auroral oval latitudes are very typical feature of the plots. Another indirect support of our hypothesis is the well-known effect of strong auroral electrojet occurrence at the auroral oval latitudes.

We should note that enhanced electric field does not mean that an HF echo would have stronger power as one might expect from the fact that the growth rate of the GD instability is proportional to the plasma drift (e.g., Tsunoda, 1988). Milan et al. (1999) and Danskin et al. (2002) presented several examples of HF echo observations from the area where electric field was monitored by the EISCAT incoherent scatter radar. It follows from these measurements that echoes occur when the electric field is somewhat larger that ~10 mV/m but there is no clear relationship between the echo power and electric field magnitude. Also Fukumoto et al. (1999, 2000) found only slight correlation of the F-region echo power and Doppler velocity that is proportional to the |**E**×**B**| plasma drift.

For the irregularities in the ionosphere to be detected, radio waves have to propagate almost perpendicular to the magnetic field lines since the irregularities are strongly stretched along the magnetic field lines, a property that is often referred to as the magnetic aspect sensitivity. Achieving perpendicularity with the magnetic field lines requires enhanced electron density in the scattering volume. Strong electron density by itself is also required because the coherent backscatter power is proportional to it (Starkov et al., 1983).

Generally, in the sunlit ionosphere, the density is expected to be higher than in absence of the sunlight. It means that the orthogonality condition is easier to reach during daytime observations. However, one has to keep in mind that frequent precipitations within the auroral oval may significantly enhance density in the ionosphere so that, after all, the effect of density decrease due to sunlight disappearance might be compensated.

Although enhanced electron density in the F region is a crucial factor for HF echo detection from there, enhanced electron density in E and especially D regions has harmful effect because at these heights frequent electron-neutral collisions lead to additional radio wave absorption while radar waves propagate to/from the scattering volume. Additionally, when electron density becomes very strong, HF radio waves can experience total reflection and significantly deviate from the direct propagation and can be lost. Also, HF echoes do not exist in the areas with very strong precipitation such as auroral arcs (Uspensky et al., 2001) perhaps due to strong electric field decrease.

While considering HF echo occurrence rates, it is important to realize that HF echoes can be received through 1½ hop. This is certainly a great advantage of HF radars over VHF systems, and the SuperDARN radars do regularly detect such echoes. However, the majority of HF echoes are expected to occur due to the direct propagation mode. This is because not all radio waves available for the direct mode signal formation would propagate to the ground and so the angular spectrum of the ground-reflected waves is narrower. Energy losses during ground reflection (for example, due to focusing waves in specific direction by an irregular reflecting surface) would add to the deficiency of the scattered power for radio waves on a 1½ hop path. Existence of ground reflected mode has detrimental effect on the ionospheric echo detection rate and thus on convection monitoring because such echoes prevent from clean ionospheric echo reception at certain ranges.

A quick overview of the diagrams of Figs. 3.3-3.6 confirms many of our expectations. All three radars detect echoes more frequently (overall) at relatively low ranges of 500-1500 km. This conclusion does not diminish the role of 1½ propagation mode in SuperDARN measurements. In fact, the RKN radar receives echoes trough this mode during winter in the noon sector and during equinoxes in the nighttime sector

(echoes at latitudes above 80^0 "co-existing" with the ones at latitudes below 80^0). This claim is supported by statistically larger elevation angles for the higher latitude echoes. The SAS radar also detects many such echoes on the dayside.

To illustrate the impact of GS echoes on IS echo rates, we show in Fig. 3.7 statistics for the ionospheric and GS echoes in September 2007 for the Saskatoon radar. Here corresponding diagrams were placed side-by-side. Of interest are observations on the dayside.

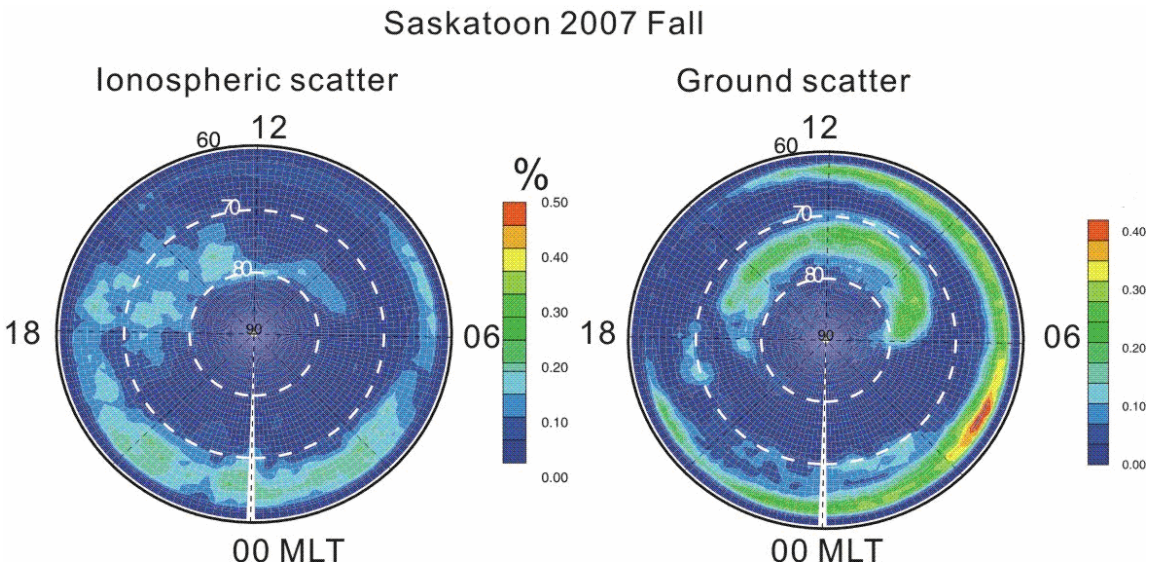

Figure 3.7. Echo occurrence rate at Saskatoon for ionospheric and ground scattered echoes in September 2007.

One can notice that the IS echoes are seen at latitudes of ~78^0-80^0 while the GS echoes are seen at latitudes of 70^0-75^0. One may anticipate that GS prevents IS echo detection at latitudes 70^0-75^0. We note that the preferential GS occurrence at latitudes "adjacent", but equatorward, the latitudes of enhanced IS echo occurrence strongly suggest that the IS echoes are received through 1½ propagation mode.

One may wonder, of course, on the reasons for echo absence at latitudes of 60^0-70^0 that are accessible to the SAS radar (since there are GS and 1½ IS echoes in these measurements). It is very likely that ionospheric irregularities are not strong enough or even absent here. Part of the reasons is that the dayside auroral oval is located at much larger geomagnetic latitudes as compared to the nightside latitudes. Additionally,

smoothing effect of the sunlight cannot be ignored entirely as for the Saskatoon location complete darkness does not last long even during winter. We think that the former effect is more significant as daytime direct mode F region echoes are seldom seen during every season. In this respect, the Halley data are even more revealing. This radar does not show much daytime echoes for all seasons, Fig. 3.6. We have to recall that geographic location of this radar is very high implying that in summer (winter) time the radar observes under sunshine (darkness) all day long and good magnetic aspect sensitivity propagation conditions can be easily satisfied during summer, but are much more difficult during winter. This implies that propagation conditions are not a major factor leading to small number of noon HAL echoes. We hypothesize that a similar effect of ionospheric irregularities deficiency exists for the SAS radar. We also have to note that for SAS, there are periods for which the terminator line is located in the vicinity of the radar so that irregularities would not be smoothed out by sunlight while propagation conditions would be still satisfactory. Yet, few echoes can be seen for such a special situation on the dayside. We conclude that it is absence of ionospheric irregularities that prevents echo detection equatorward of the auroral oval on the dayside by all three radars.

Let us now comment on other features of the RKN statistics. The RKN radar FoV is located near the poleward edge of the auroral oval. It means that even in the dark ionosphere, the orhtogonality condition is not difficult to satisfy as precipitations are enhanced in the area where the radar waves start penetration into the ionosphere (ranges 300-400 km, 3^0-4^0 poleward). In this respect, the situation is more favorable in the noon sector where the radar is located somewhat equatorward of the oval and, thus, has optimal conditions for refraction. The domination of noon echoes can be seen during equinoxes, but not so much for other seasons.

For the fall and winter, the maxima of echo occurrence were in the late evening sector at the smallest latitudes/shortest radar ranges. This sector is characterized by the frequent occurrence of substorms and associated strong precipitation and short lived enhancements of the ionospheric electric field. Onset of meter-scale irregularities related to strong electric field poleward of an expanding auroral bulge is a well documented effect (Fejer and Kelley, 1980).

The other interesting aspect of dayside observations is occurrence of far-range echoes at latitudes > 80^0. Although summer sunlit ionosphere is expected to provide better propagation conditions, and one would expect more far-range echoes, this does not happen probably because the irregularities are strongly damped during summer time by the sunlight as suggested by Ruohoniemi and Greenwald (1997). During winter, there is not much sunlight at these latitudes and the irregularities survive/are generated. In understanding the reasons for absence of the far-range summer RKN echoes one has to take into consideration the fact that electric fields are decreased at these latitudes, especially during summer, as indicated by CADI measurements (J. Jayachandran, personal communication).

Surprisingly, during equinoxes, the far-range echoes are more frequently seen on the nightside and not so much in the noon sector. It well might be that the harmful effect of sunlight still works here as on the dayside, but sunlight does not reach the midnight sector (as it does during summer) and the "winter" scenario works on the nightside.

One can certainly ask the question about absence of far-range midnight echoes during winter. It is our opinion that two effects are important. First of all, the RKN radar shows almost complete disappearance of GS echoes during winter, perhaps due to significant ice/snow coverage in the Canadian Arctic that provides poor backward reflections. Another factor is depressed electron densities in winter dark ionosphere so that production of scatters is reduced substantially and hence the needed echo power is not achieved. At equinoxes, the propagation conditions are still satisfactory and the irregularities are not so much affected by the sunlight.

In terms of irregularity production, the ranges of the RKN echoes correspond to a transition from the auroral oval to the polar cap. It is known from satellite observations (Fukunishi et al., 1993) that in this part of the high-latitude ionosphere, especially on the morning side, the electric fields are very strong. Hamza et al. (2000) reported that these latitudes are exactly where the fastest SAS velocities are often seen. In addition, poleward boundary intensifications (PBIs) occur frequently at these latitudes (Zesta et al., 2002). Both factors provide favorable environment for the GD instability operation. We can conclude that it is a fortunate combination of good propagation conditions and irregularity production that gives high occurrence rates for the RKN radar.

The HAL data showed the most simple picture; echoes were only seen at the auroral oval latitudes in the midnight sector. We explained the absence of daytime echoes by the remoteness of the area of measurements from the auroral oval and poor irregularity production. On the nightside, the surprising result is that observations during winter (complete darkness) do not show much of a difference with summer (complete sunlight) observations. This might imply that the auroral oval, even in complete darkness, always has localized "patches" of enhanced density sufficient to properly refract HF radio waves.

Unfortunately, the typical density profiles and typical densities for the latitudes of 80^0, where RKN sees most of echoes, are not well studied so far, even though there is a significant data base of systematic observations at Svalbard with the incoherent scatter radar. We consider this as an urgent task.

3.5 Conclusions

Plots of echo occurrence for three SuperDARN HF radars operated at the solar cycle minimum conditions (2007) show that the pattern of echo occurrence both in terms of maximum rates and the MLT-MLAT distribution depends strongly on the radar location. There are some seasonal trends specific for individual radars. The major conclusions from the plots can be summarized as follows:

- The typical rates of daily mean echo occurrence for the RKN, SAS and HAL radars in their bands of most frequent echo detection are ~20%, 6% and 1%, respectively.
- For some MLT sectors and MLAT latitudes the occurrence rates are much higher/lower than those typical values (by a factor of ~3).
- Generally, the rates are larger (smaller) for winter (summer) RKN and SAS observations. For HAL observations, the strongest echo occurrence is at equinox.
- All three radars detect the majority of echoes through the direct propagation mode. While Saskatoon shows a distinct area of enhanced echo occurrence at high latitudes (~80^0) near winter noon, Rankin sees echoes at these latitudes almost all the time, with some variation in the rate.

- It is a fortunate combination of reasonable propagation conditions and irregularity production in the transition region between the auroral oval and polar cap that gives unusually high echo occurrence rates for the RKN radar. For the SAS radar, a deficiency in propagation conditions contributes significantly to lower echo occurrence rates. The low geomagnetic location of the HAL radar leading to relative "remoteness" of its FoV from the auroral oval (where decameter irregularities are easier to excite) as well as its very high geographic location leading to poor propagation conditions, especially during winter, are the major factors for very low echo occurrence rates for this radar.

CHAPTER 4

OPTICAL, RADAR AND MAGNETOMETER OBSERVATIONS OF THE POLAR CAP ARC EVENT OF 07 NOVEMBER 2007

The SuperDARN radars have been successfully used for studies of plasma flows around optical forms (Chang et al., 1998; Uspensky et al., 2001; Liou et al., 2005; Milan et al., 2005; Koustov et al., 2008; Seran et al., 2009). In this Chapter, we use the RKN radar for investigation of the polar cap arc event. Two all-sky cameras have been operating in conjunction with the radar for several winter seasons, at Resolute Bay (RES) and Taloyak (TALO). In this Chapter we primarily consider Resolute Bay OMTI camera data. Resolute Bay is not at the optimal location for joint optical-radar work since, as we reported in Chapter 3, the RKN radar detects more winter echoes at MLAT of $<80^0$ so that work with Taloyak data would be more promising. However, the Resolute–Rankin work has been started earlier because the mapping software was available and Resolute Bay data were freely available. We should mention that polar cap arc occurrence is a rare and unique phenomenon known for years but illusive for detailed studies, and what we report here is an interesting piece of information on the phenomenon. Our other objective is to find arc signatures in magnetometer signals; this has been a difficult task for years (Zhu et al., 1997; Zhang et al., 1999). Some results presented in this Chapter have been reported by Liu et al. (2009) and Koustov et al. (2009).

4.1 Geometry of observations

Figure 4.1 shows the field of view FoV of the RKN and INV PolarDARN/ SuperDARN radars between range gates of 5 and 50 and the FoV of the all-sky cameras

at RES and TALO (for the off-zenith angle of 75^{o} and assumed luminosity height of 300 km). Radar range ticks (dashed line) are made for gates 15, 25, 35 and 45 (ranges in km are computable through an equation: $\text{range} = 180 + 45 \times \text{gate}$) for convenience of viewing.

Within the RKN radar FoV we indicate the position of the radar beam 7 data from which will be discussed in more detail. Also shown are the locations of several magnetometers; these are RES, TALO, Cambridge Bay (CBB) and RKN.

One can see that the RES and TALO cameras are optimal for joint work with the PolarDARN radars for range gates 5-45, corresponding to radar slant ranges of ~400-2200 km. We note that statistically speaking, detection of echoes at larger ranges is infrequent (Chapter 3) so that cameras cover the practical range of radar echo detection zone. Operation of two cameras with overlapping FoVs has great advantage because if the weather conditions are not good at one location, one would still have a chance to get common data with the PolarDARN radars at the other camera location. Unfortunately, for historical reasons, the event search has been done (so far) by first looking at the RES measurements; these seem to show fewer events. Additional advantage of having the TALO camera is that it measures much more frequently (every 10 s versus every 2 min for RES OMTI) so that dynamical optical forms can be investigated with fine time resolution including very short ranges where the RKN radar detects E region scatter.

In this study we consider one event of polar cap arc monitoring by the RKN radar on 07 November 2007. Over this day, a significant amount of joint data was collected so that several phenomena can be investigated. We focus on relatively short period of ~ 1.5 hour duration between 09:00 and 10:30 UT. During this period, a clear sun-aligned (SA) form appeared at the eastern edge of the RES camera FoV, it then moved westward, reached the RES zenith, then moved to the western part of the RES camera FoV and eventually disappeared.

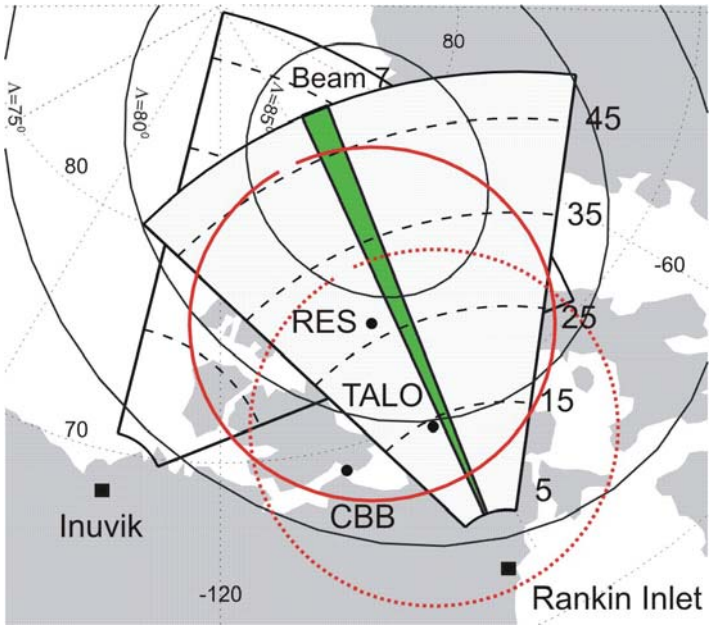

Figure 4.1. Field of view (FoV) of the Rankin Inlet (RKN) and Inuvik (INV) PolarDARN radars between range gates of 5 and 50 and location of ground-based magnetometers data from which are used in the study. The dashed lines indicate radar ranges according to the gate number (5, 15, 25, 35, 45). A shaded beam-like area (green) within the RKN FoV is the position of beam 7. Red solid (dotted) circle represents the FoV of all-sky camera (for the off-zenith angles of $<75^{o}$) at Resolute Bay (RES), Taloyak (TALO) for the assumed luminosity height of 300 km.

4.2 Resolute Bay OMTI Camera: All-sky images of the polar cap arc

Figure 4.2 shows six RES OMTI raw camera images (in red line of 630 nm) illustrating the event under investigation. At 09:00 UT, near the beginning of the event, an optical form is seen at the far eastern edge of the camera FoV stretching in the north-east to south-west (roughly sun-aligned direction). The arc is clearly progressing westward toward RES, as shown in the next frames at 09:20 and 09:30 UT. At 09:50 UT, it is located in the zenith of RES. One clearly recognizes that, at least at this time, the luminosity band is quite irregular at the most southward part of the arc where it is "merging" with the luminosity band stretched in the east-west direction, the poleward edge of the auroral oval. By 10:00 UT, the arc passed the RES zenith. The arc moved farther to the west and weakened and disappeared after 10:20 UT.

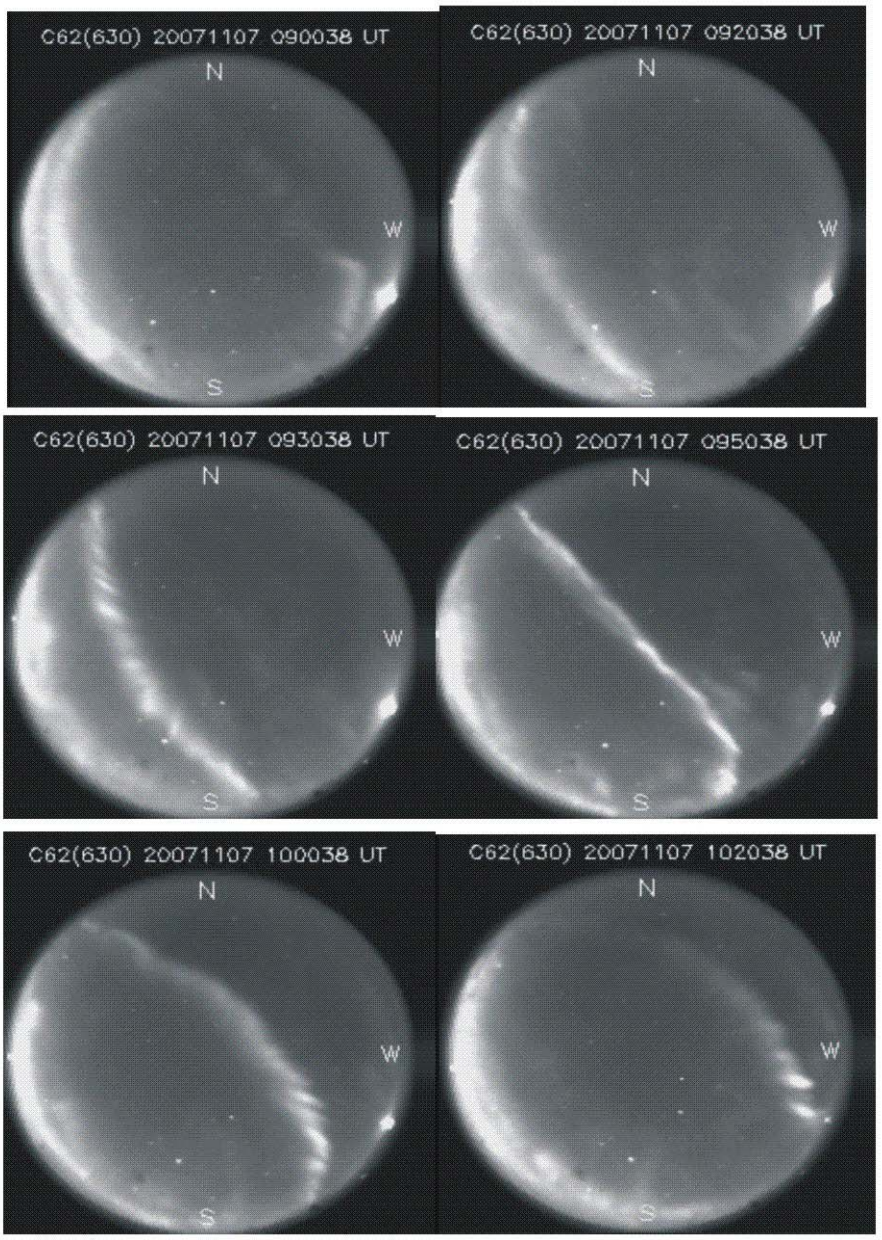

Figure 4.2. Six all sky images of a sun-aligned auroral form recorded by the OMTI camera at Resolute Bay on 07 November 2007. The wavelength of the camera filter is 630 nm.

4.3 PC arc and the auroral oval

For the event considered, the GUVI satellite was collecting data on auroral luminosity in the UV range over the northern hemisphere. Figure 4.3 shows the UV data within a "slice" stretched roughly along the noon-midnight meridian. One can see that auroral oval diameter is not large, typical of solar minimum conditions. The luminosity band over Greenland is wider than in the Central Canada sector. This is exactly the luminosity band from where the PC arc was detaching and progressing toward RES. There is a double oval luminosity structure on the noon side of the oval. No radar measurements are available for that part. Luminosity does not exist within the polar cap. There is no evidence for occurrence of the theta-aurora, which is consistent with previous observations that only ground-based cameras can detect weaker arcs (Zhu et al., 1997). Figure 4.3 also shows that the RKN radar was located near the poleward edge of the auroral oval while RES (red dot) was located clearly within the polar cap.

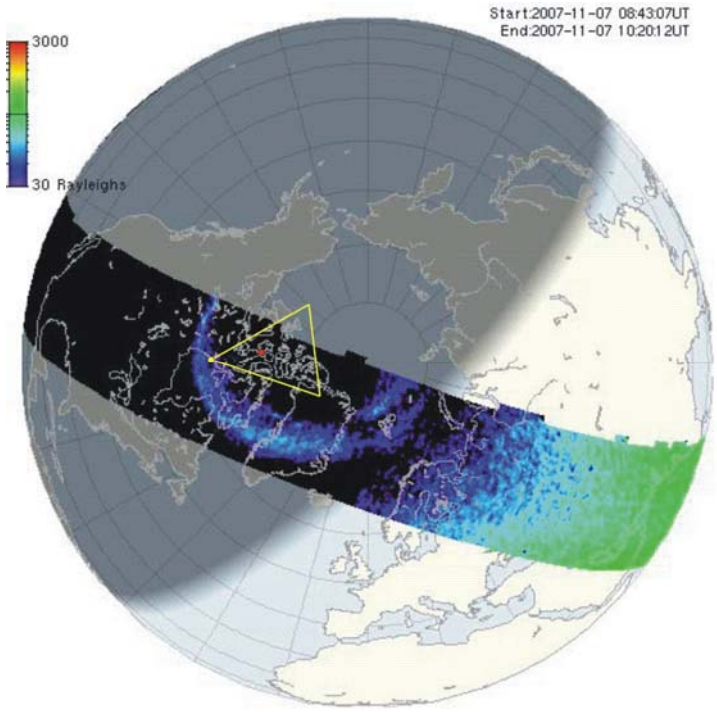

Figure 4.3. Global-scale UV image of the auroral luminosity, recorded by the GUVI satellite. The data were averaged/combined over the period of 08:43 -10:20 UT. Yellow lines show the approximate coverage of the RKN radar. The red dot is the approximate location of Resolute Bay. Data were obtained from the WEB: http://guvi.jhuapl.edu.

4.4 Taloyak all-sky camera: Some dynamical features in the PC arc behavior

Higher-rate optical observations at Taloyak allowed us to see some dynamical changes in the form of the arc as it was drifting through this camera FoV. These details are not detectable at RES not only because of the slower picture frame rate but also because these features have been observed at the equatorward edge of the OMTI FoV.

4.4.1 Distorted arc formation

While the arc was approaching the TALO zenith, it faded and a new one appeared in its wake. This is illustrated in Fig. 4.4 where one can see the original PC arc at 09:04 UT and onset of a new one, somewhat rotated with respect to the original one, at 09:08 UT. The second arc was also progressing westward and simultaneously experiencing deformations so that its equatorward part was more and more stretching toward east and not south. Eventually, the arc looked like a hook, Fig. 4.4, the 09:16 UT frame. By 09:20 UT, the arc's bent part merged with the auroral oval luminosity and the polar arc was seen as a SA form emanating from the poleward edge of the auroral oval.

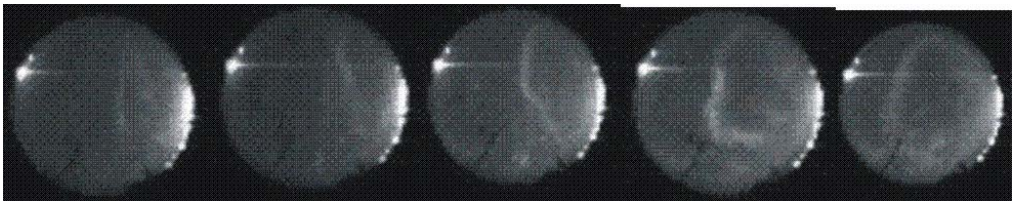

09:04 UT 09:08 UT 09:12 UT 09:16 UT 09:20 UT

Figure 4.4. Five TALO all-sky camera images of sun-aligned auroral forms recorded on 07 November 2007 between 09:04 and 09:20 UT. The top of the image corresponds roughly to geographic North, left – to West, right – to East, bottom – to South. The wavelength of the camera filter is 630 nm.

4.4.2 Onset of additional arc

Another interesting feature is a transient appearance of an additional arc near the TALO zenith at later time, Fig. 4.4. The first frame in Fig. 4.4 shows that the original PC arc passed the zenith and is located at the western edge of the camera FoV. In the immediate wake of the arc, there is not much luminosity. Somewhat to the east, the poleward edge of the oval luminosity is well seen; this band is very irregular with local enhancements seen in various spots. One can notice a more discrete form stretched in the north-south direction. This form eventually detaches from the oval-related band. This form is well seen in the TALO zenith at 09:48 UT. The form then weakened; it is barely visible at 09:52 UT, Fig. 4.4.

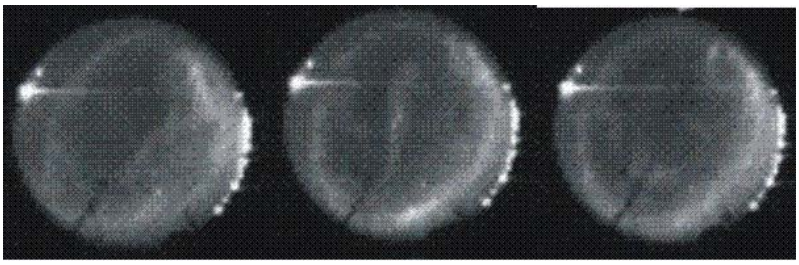

09:32 UT 09:48 UT 09:52 UT

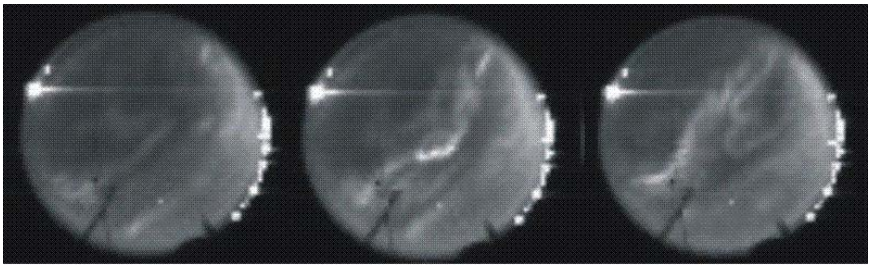

10:16 UT 10: 20 UT 10:28 UT

Figure 4.5. The same as in Fig 4.4 but for 09:32-09:52 UT and 10:16-10:28 UT.

4.4.3 Multiple arcs

Toward the end of the considered interval, 09:00-10:30 UT, multiple auroral arcs were seen starting from about 10:18 UT, Fig. 4.5. The forms had a tendency to be stretched in the N-S direction. The changes in the shape of the forms were quite fast and irregular. The intensity of the forms decreased significantly after 10:30 UT.

4. 5 General conditions on 07 November 2007

07 November 2007 was the quietest day of the month with the Kp index of 0o between 06:00 and 02:00 UT. The low activity is expected from the IMF conditions as the B_z component was positive over a significant portion of this period, Fig. 4.6.

In Fig. 4.6, the ACE measurements of the IMF, shifted forward to account for time delay of ~112 min required for the disturbance propagation from the satellite location to the midnight sector of the high-latitude ionosphere, appropriate procedure is given in Appendix B are presented. The shaded box indicates the period of the ground-based measurements under discussion. We first notice that the IMF B_z was mostly positive varying between 0 and +2 nT. After 10:30 UT, it finally settled to negative values. This is roughly the time when optical activity intensity decreased at both RES and TALO. The IMF B_x component was positive at ~2 nT most of the time. The IMF B_y component experienced significant variations. The original PC arc onset correlates with the beginning of B_y turning from positive toward negative values. The B_y polarity changed at ~9:10 UT and stayed at ~ -1.5 nT for ~ 25 min. After 09:40 UT, the IMF B_y became positive again and stayed at ~ +0.5 nT for the rest of the event considered. Clearly, the westward arc motion showed no obvious relationship with the B_y/B_z orientation.

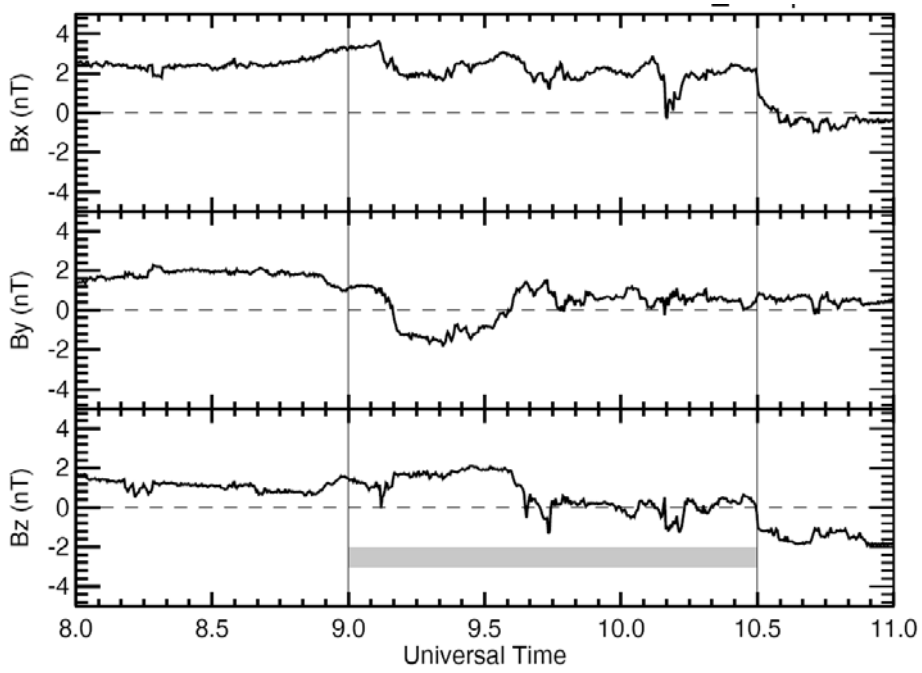

Figure 4.6. Interplanetary magnetic field (IMF) X, Y and Z components in the GSM coordinate system according to the ACE satellite measurements on 07 November 2007 between 08:00 and 11:00 UT. The data were shifted by 112 min forward. Shaded box correspond to the period during which the PC arc (Fig. 4.2) was observed by the RES OMTI camera. Vertical solid lines indicate moments of easily recognizable start in the duskward progression of the PC form and the time of its complete fading away.

The event is also characterized by very quiet magnetometer records. We will investigate measurements in the arc vicinity later. Here we present the X components of the magnetometer records across Canada from 08:00 to 11:00 UT, Fig. 4.7. The exact magnetometer locations are not crucial at this point; it is sufficient to say that together, they cover the auroral oval latitudes over Canada and some of them go deeper into the polar cap. One can find detailed information on the magnetometers at the official CARISMA WEBsite: http://bluebird.phys.ualberta.ca/carismaweb.

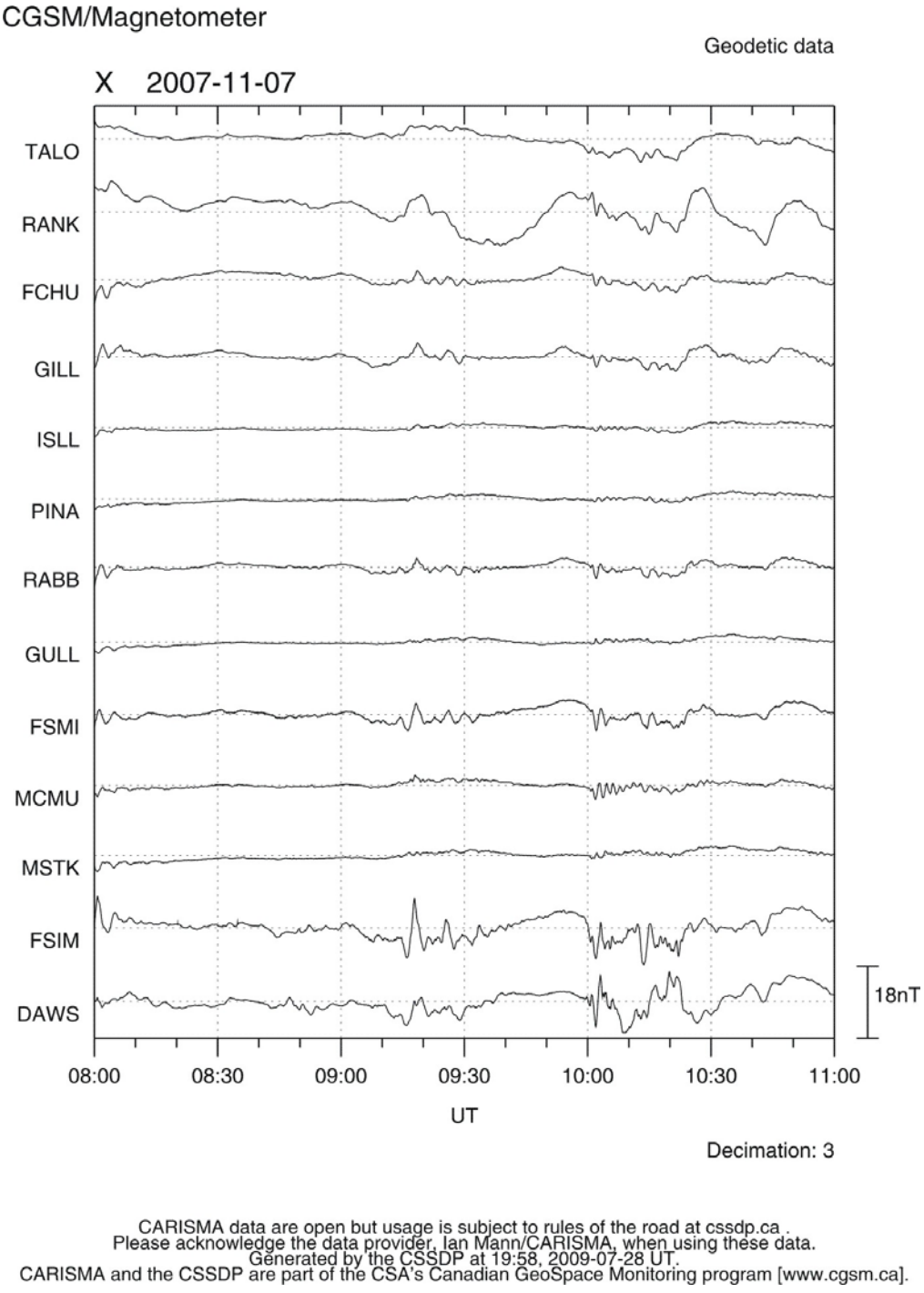

Figure 4.7. Earth magnetic field X (North-South) component variations recorded on 07 November 2007 between 08:00 and 11:00 UT. Magnetometer locations can be found at the WEB: http://bluebird.phys.ualberta.ca/carismaweb.

4. 6 Rankin Inlet radar observations in the arc vicinity

4.6.1 Range profiles for beam 7

On 07 November 2007, the RKN radar was operating in the fast (1-min) scanning mode. Reasonably good data were collected for the entire event. Figure 4.8 shows temporal variations of the echo power, velocity and spectral width at various ranges of beam 7. The standard British color scheme is used. The period of PC arc onset and progression is denoted by a horizontal bar on top panel.

The event started from relatively low-intensity echoes and even signal disappearance at ~09:15 UT. The band of echoes covered ranges of F region scatter (bins 20-35). The echoes disappeared after ~10:45 UT. Strong power variations occurred during the arc crossing of this beam, between 09:10 and 10:10 UT. We mention that short range echoes were also detected, but they are not a subject of the present study. Contrary to the event investigated by Koustov et al. (2008), we were not able to find regularity in the behavior of the parameters of these echoes.

The velocity also experienced strong variations in magnitude and even the polarity. Prior to 09:15 UT, it was positive at short ranges (bins 20-25) and negative at large ranges (bins 25-35). After signal reappearance at 09:20 UT, velocity was negative at short ranges and positive at far ranges, i.e. regions of negative and positive polarities switched their relative location. Positive velocities were, on average, larger than negative velocities.

Spectral width of echoes was enhanced (red color) between 09:00 and 10:10 UT. This corresponds to the period of arc presence in the vicinity of beam 7.

4.6.2 Radar echo power and velocity maps

Both power and velocity RKN maps show recognizable features in their dynamics once the approximate position of the PC arc is established. Figure 4.9 demonstrates a clear westward progression of the area with enhanced echo power, from

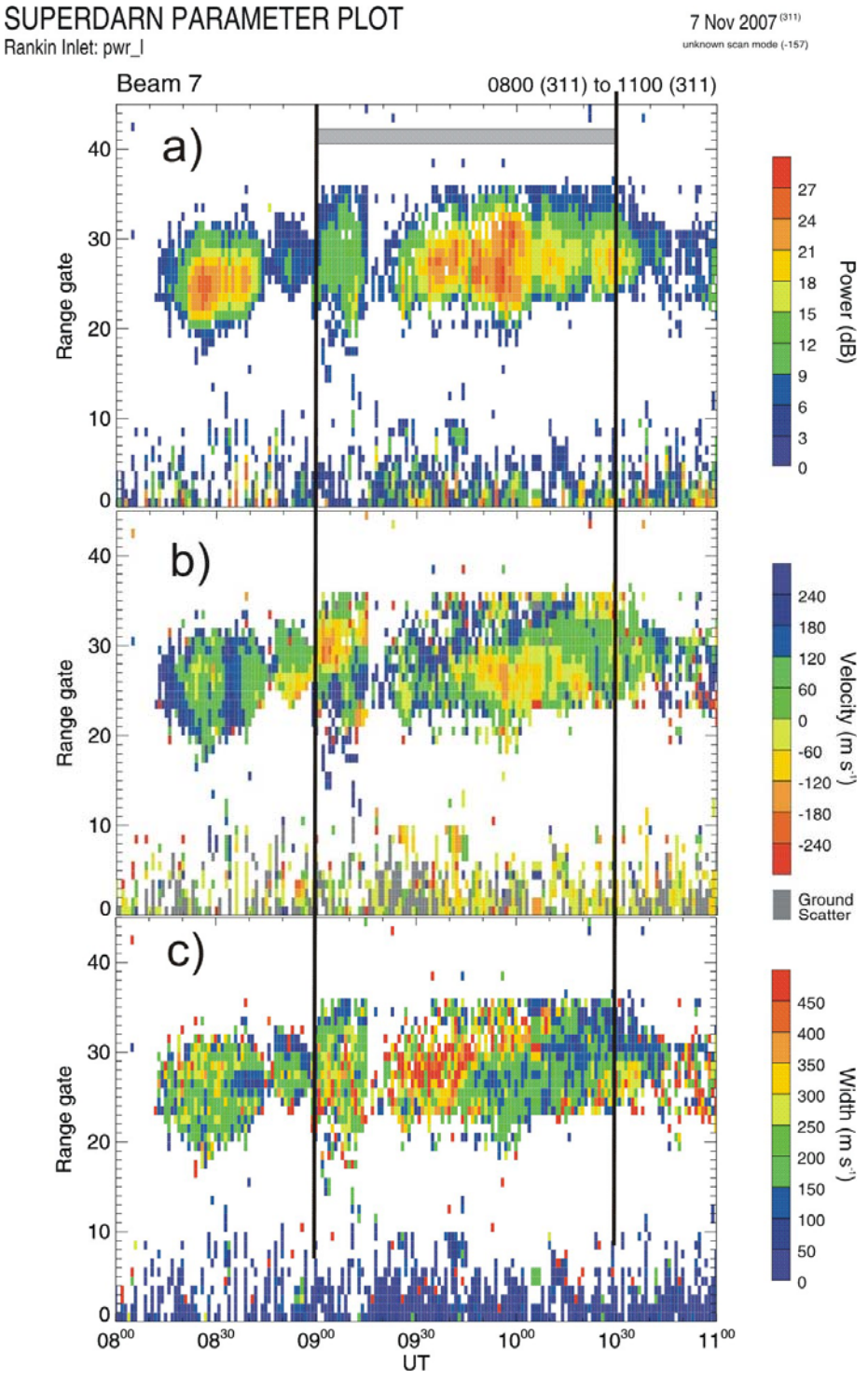

Figure 4.8. Echo power, velocity, spectral width according to RKN measurements in beam 7 between 08:00 and 11:00 UT on 07 November 2007. Horizontal bar on top panel and vertical lines indicate the period of PC arc progression through the RES OMTI camera FoV.

most clockwise beams 10-15 to most counter-clockwise beams 0-5. All frames show formation of an additional region with enhanced echoes; this region progresses westward, reaches maximum at 10:10 UT and fades away after that time. At 09:16 UT, the arc was aligned roughly with beam 7. At this time, very weak echoes were seen in this beam (just 3 gates with very low power).

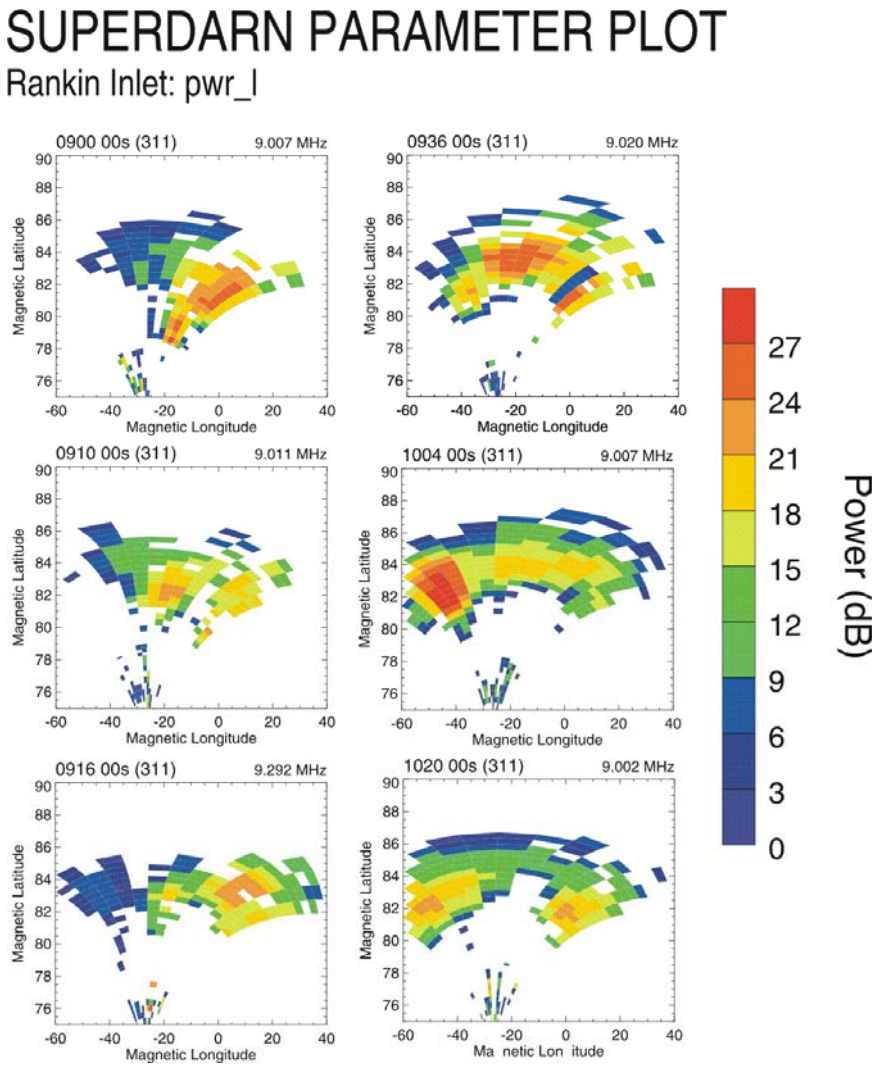

Figure 4.9. Selected RKN power maps for the 07 November 2007 event.

Figure 4.10 shows the velocity maps for the times of the echo power maps of Fig. 4.9. The first three frames, corresponding to the arc location eastward of beam 7, one can notice a yellow blob of the negative Doppler velocity in the most CCW westward beams.

This velocity polarity corresponds to the plasma flow away from the radar, and probably reflects the overall sunward flow. We will investigate this feature later. The next three frames, at 09:36, 10:04 and 10:20 UT, show formation in the west of the cigar-like region with negative velocity within the overall cloud of echoes with the positive velocity. This feature can be interpreted as formation of a channel with the flow away from the radar, probably toward the Sun.

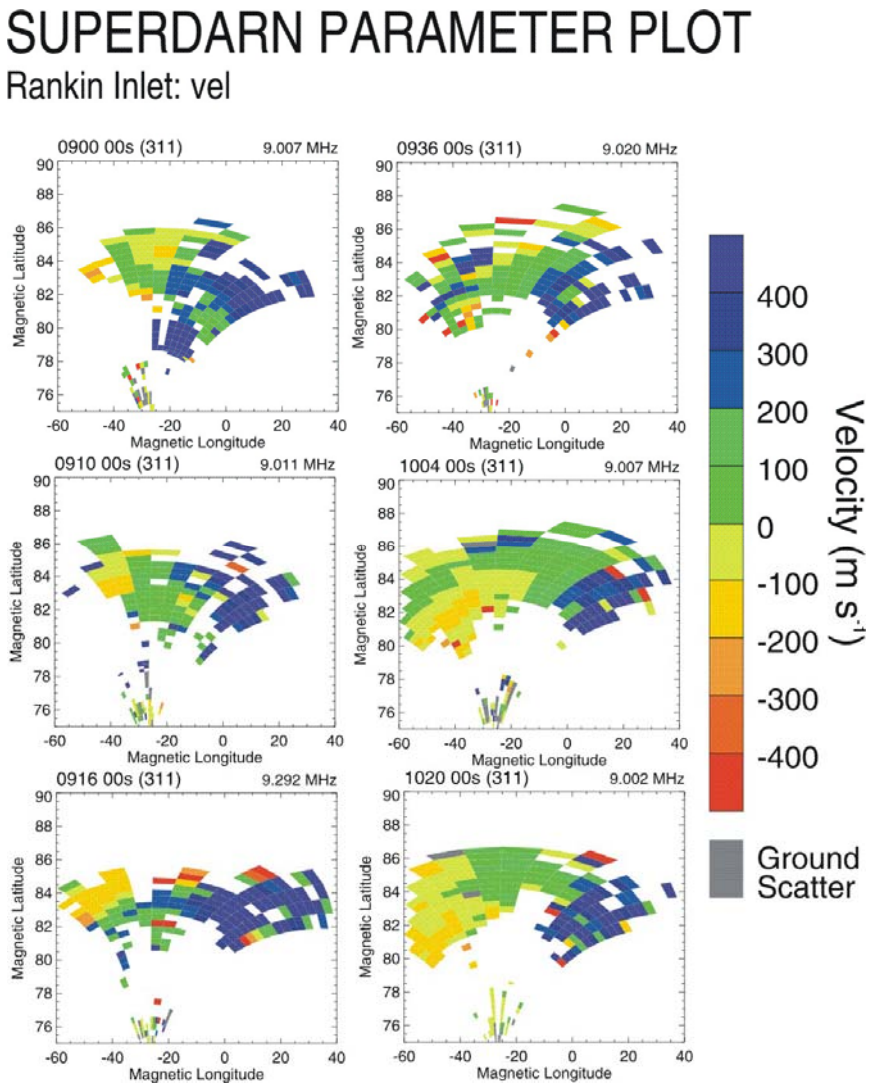

Figure 4.10. The same as Fig. 4.9 but for the velocity.

4.7 Locations of HF echoes and the PC arc

Figures 4.11 and 4.12 are plots of the luminosity (left columns) and superposition of luminosity and HF echo power and velocity (right columns) in the MLT-MLAT coordinates. We consider the same times as in Figs. 4.9 and 4.10. The mapping is done by assuming the luminosity height of 250 km (630 nm filter data). When the arc was strong, its location on the radar-optical frames was shown by a dashed line.

One can recognize sun-alignment of the luminosity band detached from the auroral oval as it stretches through the entire FoV of the camera towards 12:00 MLT tick. The optical arc was diffuse for the first three frames, evolving into a thin line on the fourth and fifth frames and having only a split equatorward end at the last frame. The form was not homogenous along its length, although that is most obvious in the last frame.

The white lines in Fig. 4.11 illustrate the feature that we have already mentioned, namely westward progression of the area with enhanced echo power. One can also recognize the stretching of the echo power pattern along the arc for the last three frames. The stretched echo-area was shifting westward together with the arc. For this reason, these echoes were very likely produced with involvement of the arc-associated electrodynamics.

Figure 4.12 shows the RKN velocity distribution in the vicinity of the PC arc. For the first three frames, the arc is located exactly in the area of the velocity polarity reversal. The arc and the reversal westward progressions are synchronous. The next two frames show formation of a narrow channel with sunward flow in the areas eastward of the PC arc. The last frame indicates that the arc is located within the sunward flow plasma.

The above interpretation of the flow directions around the PC arc assumes that the flow is predominantly along the arc. This is not quite correct because the arc had been shifting westward implying the convection component in this direction of the order of 100 m/s. More detailed analysis of the flow pattern will be performed later.

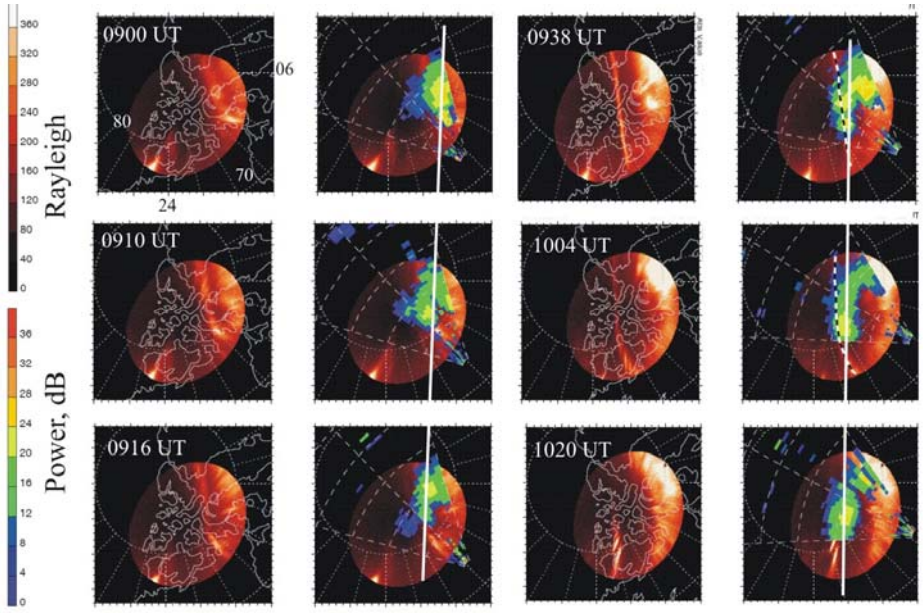

Figure 4.11. Selected maps of the luminosity distribution (left columns) and luminosity-RKN echo power distribution. Magnetic local time- magnetic latitude coordinates are used. White line is shown to indicate the westward progression of the area with enhanced echo power. When the arc luminosity was strong, its location on combined optical-radar maps was shown by dash line.

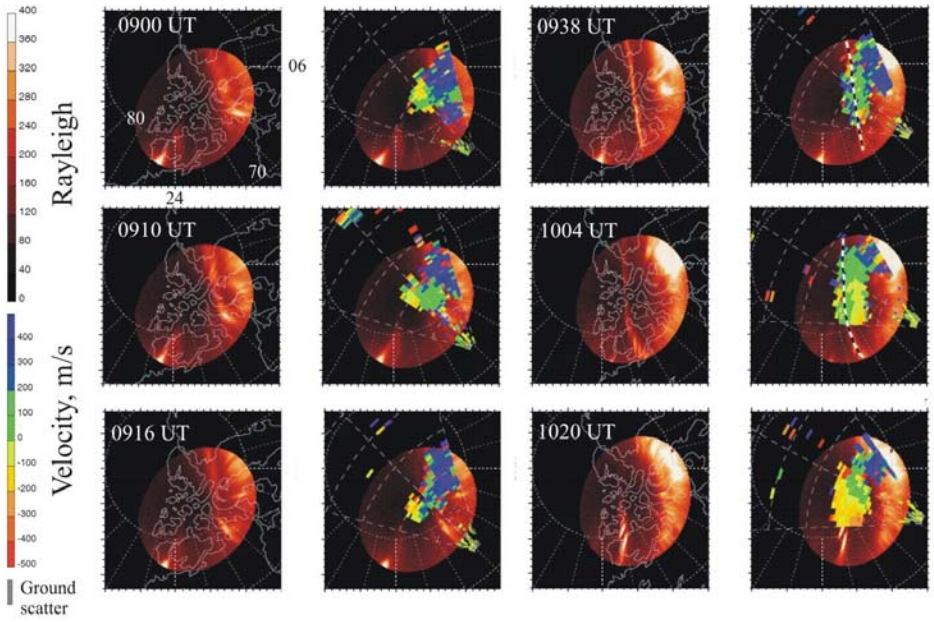

Figure 4.12. Selected maps of the luminosity distribution (left columns) and luminosity-RKN echo velocity distribution. Magnetic local time-magnetic latitude coordinates are used. When the arc luminosity was strong, its location on combined optical-radar maps was shown by dash line.

4.8 Detailed analysis of echo parameters for near-zenith arc location

Comparison of optical and radar data on a single map has some uncertainties of mapping. To make a more detailed comparison, we selected a frame for which the arc was located near the RES zenith so that, at least the optical data are positioned properly. Figure 4.13 shows the optical arc and distribution of (a) power, (b) velocity and (c) spectral width for 09:56 UT. For convenience we also added a marker (white dot) for radar range gate 27, beam 5 roughly corresponding to the location of Resolute Bay.

We would like to start from the spectral width diagram, Fig. 4.13c. One can clearly see that a band of broad-spectrum (widths up to 400 m/s) echoes extends all along the arc. We have already mentioned that broad spectra correlate with the arc location, and this diagram confirms this conclusion. We should also mention existence of a blob with broad echoes in the most CW beams. This blob correlates with the edge of enhanced luminosity at the poleward edge of the auroral oval. Notice that all other echoes have typical widths of <200 m/s (this value has been reported by Villain et al., 2002).

Figure 4.13a shows that the echo power is enhanced at ranges about 100-300 km closer to the radar than the arc location. This result is consistent with observations of Uspensky et al. (2001) in the auroral zone. We also should mention that echoes at the most CW beams are quite away from the arc, and moreover, the pattern of echo distribution suggests that these echoes are related to the poleward edge of the auroral oval. It is very likely that the radio wave propagation conditions are not satisfactory for echo detection near arc in these beams.

Doppler velocity data of Fig. 4.13b confirm our expectation regarding the nature of the echoes in the most CW beams. The velocity here is strongly positive and it drops sharply to much smaller values in beams 10-12. The velocity distribution for the echoes in the arc vicinity is quite peculiar. The farthest echoes located duskward of the arc have negative velocity. Close to the arc and at the arc location, the velocity is positive. Closer to the radar, to dawnward from the arc, the velocity is again negative. The band of negative velocity is quite stretched parallel to the arc suggesting that the band and the arc might be related.

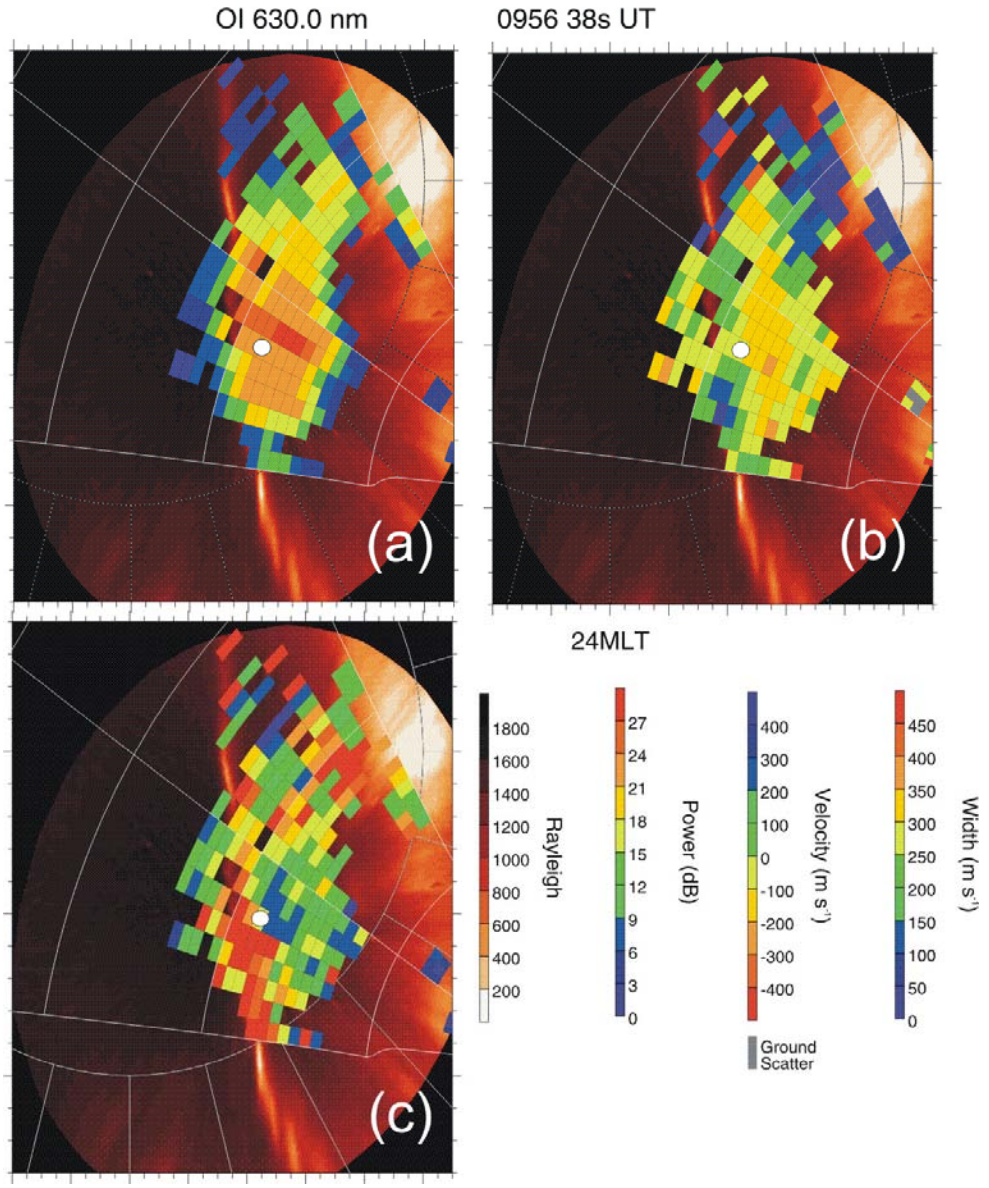

Figure 4.13. Optical image of RES OMTI camera at 09:56 UT on 07 November 2007 and RKN (a) echo power, (b) velocity and (c) spectral width maps for the closest scan. The radar and optical data are plotted in geomagnetic latitude–MLT coordinates with 24:00 MLT at the bottom and 06:00 MLT to the right of the diagram. Seen radar range gate circles correspond to bins 15, 30 and 45. White circle denotes the Resolute Bay location.

To give more quantitative assessment of the velocities observed we plotted the velocity distribution along the RKN beam 7, Fig. 4.14. Here we considered 10 RKN scans near the time of interest and plotted echo parameters versus range gate (range). The IDL software used to analize RKN data is presented in Appendix C. Figure 4.14a

shows that echo power was strongest ~135 km closer to the radar. Velocity was ~+100 m/s at locations ~ 300 km away from the arc, closer toward to the radar.

Velocity changed its polarity to reach ~-100 m/s at ranges ~ 100 km away from the arc location toward the radar. At ranges beyond the arc location, velocities were larger, ~ ± 150 m/s.

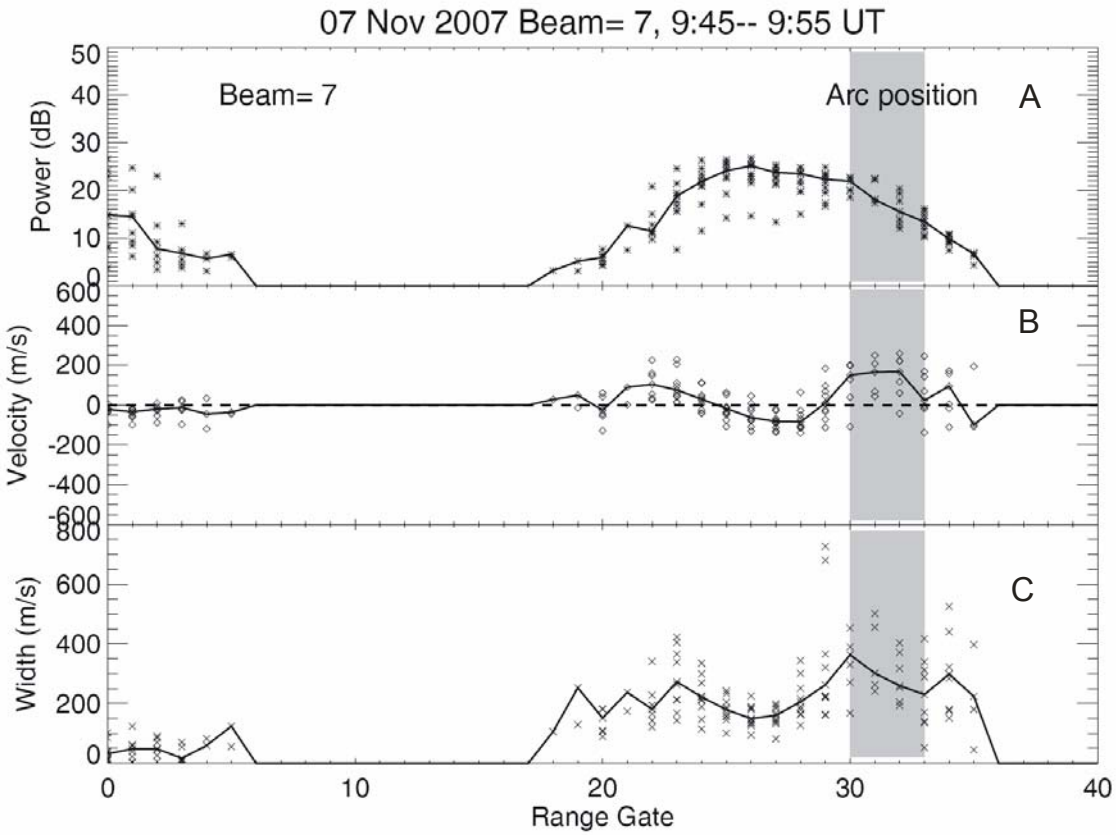

Figure 4.14. Power, velocity and spectral width distributions along the RKN beam 7 for the period of 09:45-09:55 UT. Solid curve connects the median values for measurements in each individual radar gate. Vertical dashed line indicates the approximate location of the arc within beam 7.

Figure 4.15 gives a quantitative description of echo parameter distributions in one radar gate 27 for various radar beam positions (azimuthal scan) during the time 9:45-9:55 UT. At this radar gate, the arc was crossed by beam 4. One can see enhanced echoes in central beams, a change of the velocity from ~+100 m/s westward of the arc in beams 2-4 to negative velocities of ~-100 m/s in central beams and to large velocities +

400 m/s in beams 10-13. Once again, these high-velocity echoes were probably not related to the arc.

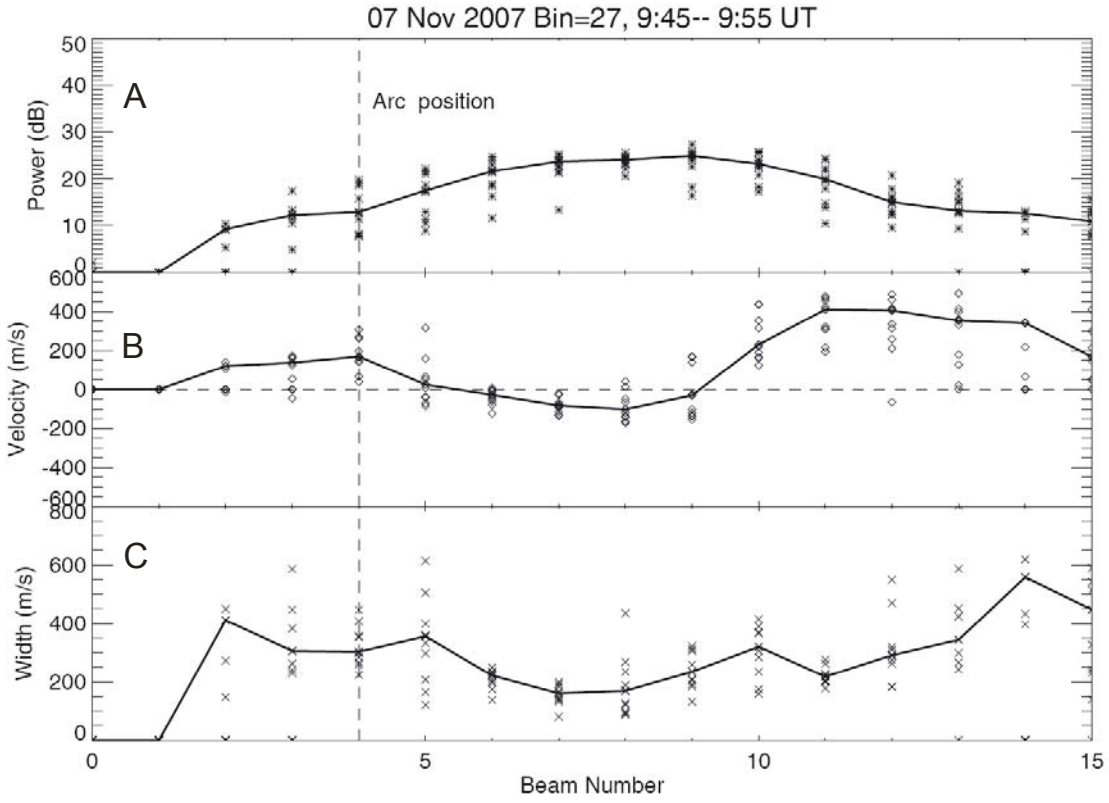

Figure 4.15. Power, velocity and spectral width distribution for radar gate 27 and various RKN beams between 09:45 and 09:55 UT. Solid curve connects the median values for measurements in each individual radar gate. Vertical dashed line indicates an approximate location of the arc within beam 7.

4.9 Global-scale convection pattern and PC form location and orientation

Plasma flows associated with PC arcs and their role in the formation of the global convection pattern is one of the important but unresolved so far issues (Zhu et al., 1997). For the considered event, the RKN and other SuperDARN radars collected a reasonable amount of data and the assessment of the global convection pattern is possible. Standard SuperDARN convection maps have been made for the entire period of the study by

applying the FIT procedure (Ruohoniemi and Baker, 1998). Below we comment on several interesting maps.

For the period of the arc detachment from the auroral oval, e.g. 09:06 UT, Fig. 4.16, the arc was located within the region of antisunward flow. For the RES location which is the center of the all-sky camera FoV, the flow is toward geographic East and this is consistent with what CADI observations (data are not presented here).Velocity magnitudes of ~100 m/s are also consistent. For the arc location, the velocities are rather decreased. The enhanced flow channel is well seen in the area with low luminosity, between the detaching arc and the rest of the auroral oval.

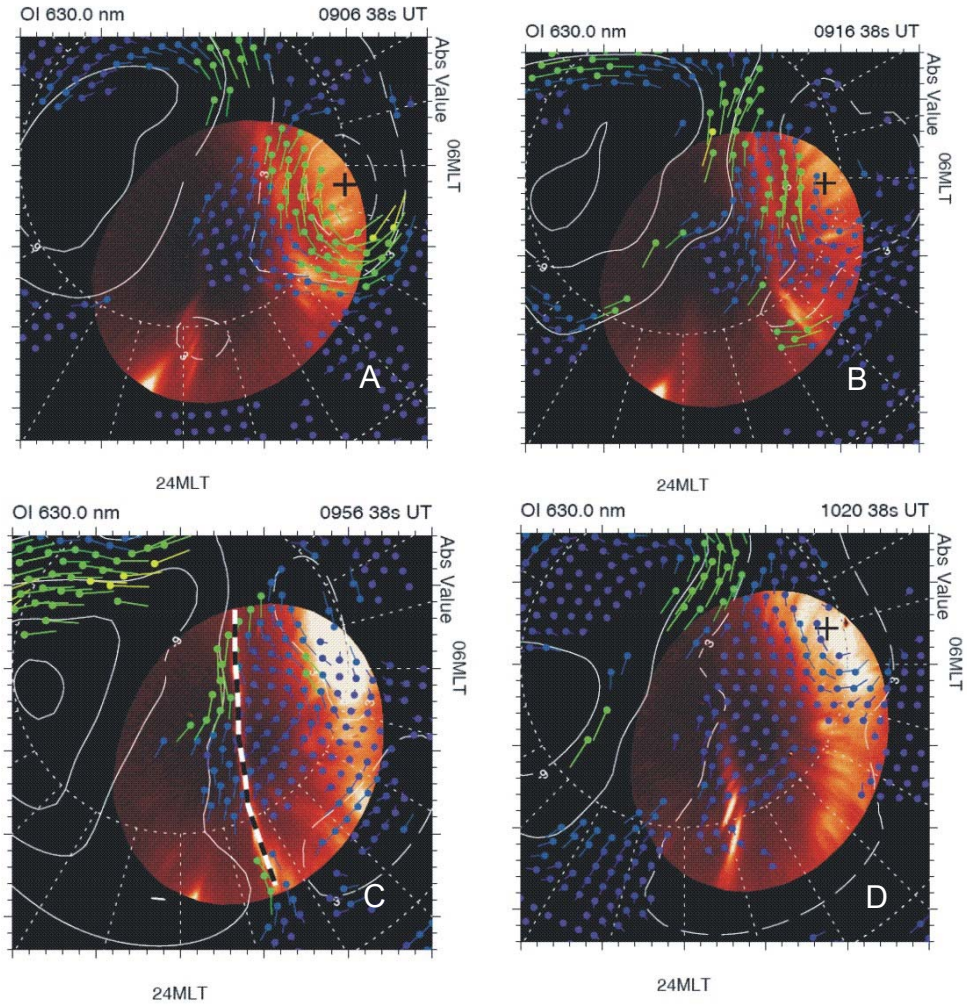

Figure 4.16. Global-scale maps of the luminosity distribution according to the Resolute Bay OMTI camera measurements and overlaid convection vectors inferred from the entire SuperDARN network measurements for the scan closest to optical measurements. (a) 09:10 UT; (b) 09:16 UT; (c) 09:56 UT; (d) 10:20 UT. The color scheme is the same as in Fig. 4.13.

At later time, e.g. around 09:16 UT, when the equatorward edge of the arc has been changing and TALO camera showed the onset of a new and bent arc, the flow pattern showed a peculiar kink, Fig. 4.16b, with plasma flow roughly around the bent arc so that the arc was located roughly in the convection reversal region. For 19:56 UT, the arc is still located within the region of antisunward flow. The sunward flow to the East of the arc is not seen; instead, the FIT technique infers very stagnant flows there. We feel that this is a minor deficiency of the technique. Toward the end of the event, when the main arc started to fade away and multiple arcs were seen at TALO, Fig. 4.16d, the flow was antisunward with significant westward component, e. g. for the RES location. It is interesting to note that the flow between the two arcs (the main to the East of TALO and the new one in the TALO zenith) is almost zonal, directed to the West. One would expect this on the basis of the velocity map for 10:20 UT, Fig. 4.16d. Such flow seems to be a separate local current system established between the arcs; in Fig. 4.16d one can recognize global morning and evening convection cells with quite regular flows.

4.10 High Arctic magnetic perturbations during the PC arc event

As have been mentioned, magnetic perturbations were extremely weak during the event considered, including the auroral zone locations. Here we investigate in detail the high-latitude measurements in close vicinity to the arc. We consider RES, TALO, CBB and RKN data, Fig. 4.17. In Fig. 4.17, the period of arc occurrence is denoted by horizontal bar in the bottom panels.

Figure 4.17 shows that magnetic perturbations in all components and at all locations were of the order of 10 nT, which are very low values. Temporal variations at RKN were quite different as compared to other magnetometers suggesting that this magnetometer was measuring in a different geophysical area. This is consistent with the fact that RKN was located within the auroral oval (Fig. 4.3) while all others magnetometers were located poleward of the oval, in the polar cap. This conclusion is supported by the RKN measurements in the X component; a sharp negative deflection occurred right after the auroral oval intensification. No similar perturbations were detected at other locations.

Patterns of the X-component variation in Fig. 4.17 were similar at CBB and RES; there was a negative perturbation starting from the moment the arc passed the zenith position (CBB) or reaching maximum near the arc zenith position (RES). Maximum in the perturbation were achieved after the arc passed the zeniths. Over the next ~ 30 min, the X components not only recovered to the "pre-arc" levels, but even went up. X-component perturbations at TALO were similar to the ones at CBB.

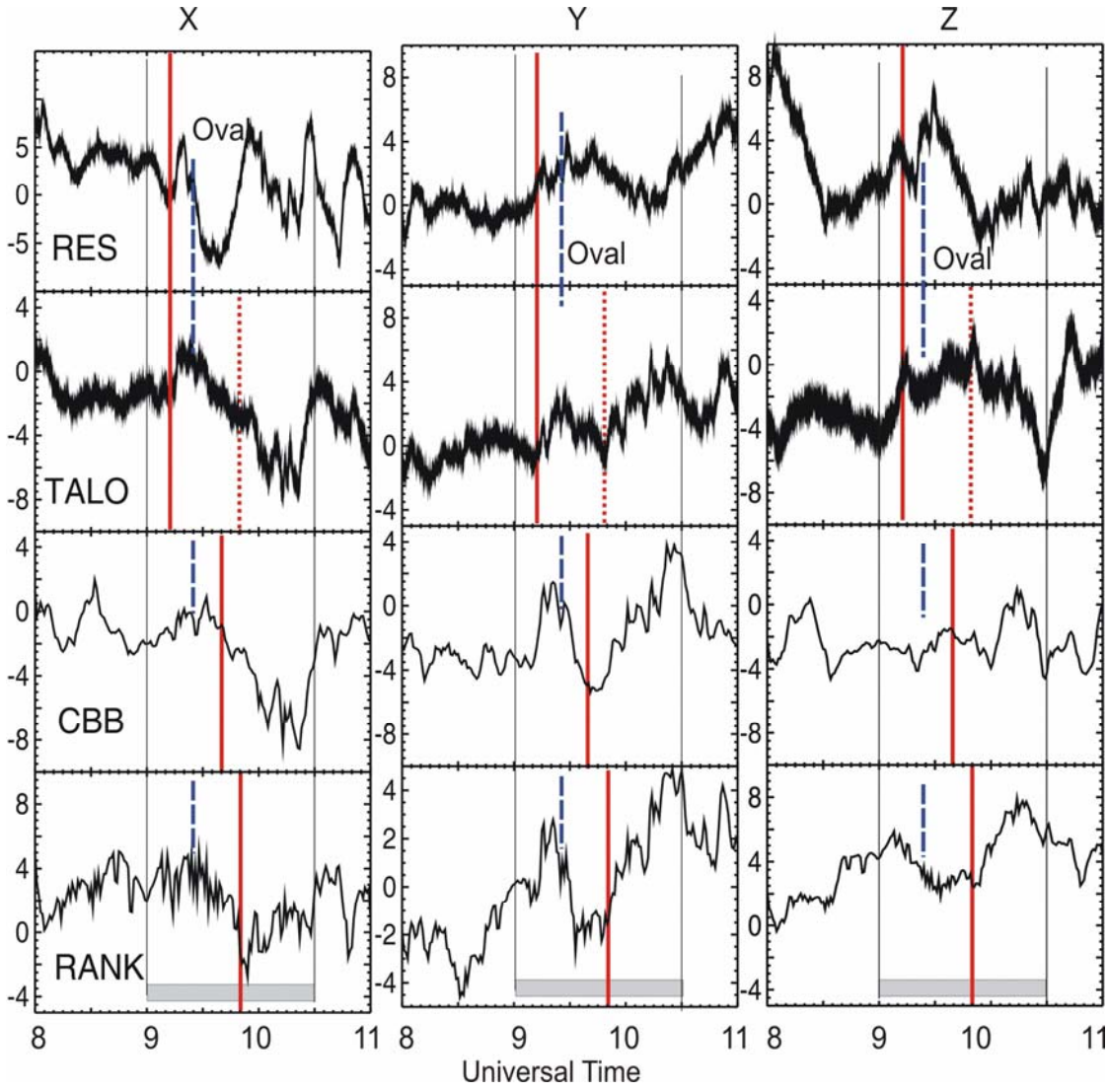

Figure 4.17. X, Y and Z component fluctuations of the Earth magnetic field in nT recorded at Rankin Inlet (RKN), Cambridge Bay (CBB), Taloyak (TALO) and Resolute Bay (RES) between 08:00 and 11:00 UT on 07 November 2007. Here a red vertical line denote the time for the PC arc location near the zenith for each magnetometer. Dashed line shows the time of second (bended) arc occurrence over TALO. Blue line corresponds to intensification of luminosity within the auroral oval, as detected at RES.

Patterns of the Y-component variations in Fig. 4.17 were also similar at CBB and RES, namely there was a positive perturbation well prior to the arc arrival to the zenith and negative perturbation after the arc passed the zenith position.

The Z-component perturbations at RES and CBB were very small and less consistent. The RES perturbation was negative (positive) prior (after) the arc crossing the zenith.

Explanation of magnetic observations can be given in terms of two-strean model of the currents, Fig. 4.18. In Fig. 4.18 we show the arc detached from the auroral oval. We assume that there was an antisunward current stream (sunward convection) downward of the arc and sunward current stream (antisunward convection) at the poleward edge of the auroral oval. We also show three typical locations of the magnetometers with respect to the arc. For these two streams and a magnetometer location at points 1, the X-, Y- and Z-component perturbations would be negative, positive and negative. This is consistent with what has been observed. For the position 2 and anywhere between 2 and 3, the second stream of oppsite direction would start compernsating the magnetic effect of the first current, so that the perturbations would go toward zero. For the position 3, the second stream, that was more intense than the first one, would dominate and provide negative, negative and positive perturbations in the X, Y and Z components, respectively. This also consistent with observations.

Proposed interpretation implies that the magnetometers did not sense currents duskward of the arc. These were probably not strong; in absence of precipitation, the ionospheric conductance was probably too low to provide strong enough current. These magnetic variations associated with the moving PC arc are quite different from the data presented by Zhang et al. (1999). These authors considered a case of very strong transpolar arc crossing the Eureka station (MLAT=89^0). The major signatures of the arc were positive ~ 30 nT perturbation in the X component, almost no perturbation in the Y component, and a transient jump of ~ 20 nT from negative to positive values in the Z component. These variations were shown to fit well with a single infinite string-like source stretched towards noon. In that study, it was reported that, for other cases, no clear magnetometer signatures of PC arcs were found. This result supports our

conclusions that interpretation of magnetometer signals related to the PC arcs is a challenging task.

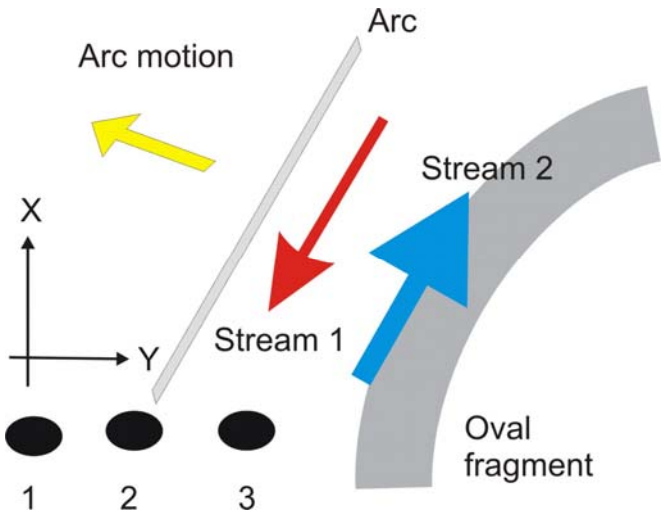

Figure 4.18. Model of equivalent current streams explaining the magnetic observations at RES and CBB during the PC arc event on 07 November 2007.

4.11 Discussion

In this study, the Rankin Inlet PolarDARN/SuperDARN HF radar measurements were combined with all-sky camera observations at Resolute Bay and Taloyak to investigate radar signatures of, and the plasma flows around, the polar cap optical arc originated on the dawnside, at the poleward edge of the auroral oval, and moving across the polar cap. The optical arc was stretched along the line constituting an angle of ~ 30^0 with the radar's central beams so that mostly the component of the plasma flow tangential to the arc was monitored.

In terms of general morphology, the observed PC arc was a typical dawnside feature reported in the past (Shiokawa et al., 1995). The arc was one of the brightest in a series other faint features. Its speed of duskward progression was of ~ 100 m/s. The motion was fairly steady. The equatorward "end" of the arc was seen as "buried' into the auroral oval luminosity band very much similar to what has been reported for the theta aurora (Zhu et al., 1997; Newell et al., 2009). We also reported some dynamical

changes in the arc configuration and plasma flows at this "juncture" of the PC arc and the oval.

The whole event occurred during a period of positive IMF B_z (+2 nT) with some short-lived dives to ~ 0 nT. The arc disappearance right at the IMF B_z turning to negative values at ~10:30 UT is consistent with the notion that a PC arc is predominantly a B_z positive phenomenon (Newell et al., 2009). Rodriguez et al. (1997) reported that the PC arcs disappear about 20-30 min after the southward IMF turning. In our case, the arc faded away at about the time of B_z sharp southward turning. Several weak PC forms were seen at RES after 10:30 UT. These were much weaker and well might be simply bands of polar rain (Newell et al., 2009). In this respect, it would have been beneficial to have particle measurements on DMSP satellites. Unfortunately, such data are not available for the event considered.

The main arc first appeared for B_y^+ condition while this IMF component was undergoing a transition to negative B_y. So, the polarity of IMF B_y was not what has been reported in the past for moving theta aurora and some polar cap arcs in the morning sector (Kullen, 2002). Later on, about 10 min later, the B_y had finally reached negative values, and observations of auroral duskward progression for negative B_y would be consistent with previous studies (Valladares et al., 1994). We wonder if some disagreement with previous publications resulted from incorrect determination of the time delay for the IMF to propagate from the ACE satellite position to the Earth's magnetosphere. Our procedure of evaluation of delays is described in Appendix A.

Radar signatures of the PC arc were quite different as compared to recent SuperDARN radar observations of theta aurora (Chang et al., 1998; Milan et al., 2005; Liu et al., 2005; Eriksson et al., 2006) and auroral zone evening arcs (Uspensky et al., 2001) in a sense that the echoes were detected continuously and in most of the space around the optical structure at radar ranges of 1000-1500 km. In the past, patchy and episodic echo occurrence across vast areas constituting theta-aurora were only available and no small-scale details of the flows have been investigated.

Koustov et al. (2008) presented recently a case of PC arc monitoring with the RKN radar. Although the optical arc in that case was similar to ours, our radar signatures

are quite different. For the case of Koustov et al. (2008), the echoes were detected only at very short ranges. These were very likely E region echoes. The signatures of the arc have been identified as a significant echo power drop and velocity polarity change at the front edge of the moving arc. In our case, there is little doubt that the echoes were coming from the F region because of large ranges of echo detection. The echo power was enhanced in the wake of the arc with very few echoes duskward of it. The former feature is similar to the effect of echo power decrease in the luminous areas, but the power decrease with range was rather smooth, without a sharp drop. The effect of power decrease was prominent when the arc was aligned with beam 7 (Fig. 4.7).

We showed that the blob with enhanced echo power in the arc's wake was shifting together with the arc duskward. This might be interpreted in two ways: either irregularities were strong enough only in that region or the propagation conditions were only good there. Duskward of the arc, the propagation conditions were probably poor because of low density (no precipitation). As the arc moved away from the radar, its poleward edge became less and less "visible" with eventually no echo returns at all (Fig. 4.7). This could be interpreted as deteriorating propagation conditions.

Our observations at the end of the event, when a new arc was set over TALO, clearly showed limitations of the RKN radar in monitoring auroral arcs. The new arc was quite prominent, seen by both TALO and RES all sky cameras, but no echoes in this arc vicinity have been detected. Whether this is because of extra radio wave absorption in the precipitation region or no irregularity generation cannot be resolved.

The other differences with the previous case is behavior of the echo velocity near the arc. Observations between 09:00 and 09:15 UT showed sheared flows with a pattern very much similar to the case of Koustov et al. (2008). It is not so clear if this was truly the shear. Global convection mapping (Fig. 4.17, top left panel) interpreted the data as the azimuthal flow rather than meridional at this time. The observed velocity shear then is merely reflection of the fact that the radar was observing almost perpendicular to the flows so that the velocity polarity was different in the most CW and CCW beams.

The sheared flows for the period around 09:50 UT seem to be the real shear. Moreover, the new significant area with sunward flow was observed. CADI also detected "rotation" of the convection direction for observations on the dusk- and dawn-

sides of the arc (data are not presented here). FIT mapping washed out this shear though strongly stagnant flows for the expected regions was very evident.

An interesting and important feature of our observations is that the reversal of the flow did not coincide with the arc location. There might be some concerns about accuracy of the echo and luminosity mapping. We note that for the period under discussion, the arc was located near the zenith so that errors in luminosity mapping were minimal (<50 km). The radar echo mapping is more questionable. The expected error in mapping (overestimation of location range) can be anywhere from 50 to 300 km (Yeoman et al., 2008). Another effect is radio wave slowing down in the ionospheric plasma so that, again, the actual ranges should be shorter. If this is correct, the shear would be located even farther away from the arc, somewhere between the arc location and the poleward edge of the oval luminosity (Fig. 4.13). Such artificial shifting of echo locations to closer ranges would mean that not much echoes were seen westward of the arc location. This makes sense as one would not expect much electron density in those regions so that refraction is not sufficient to bent radar waves and meet the orthogonality condition.

The nature of sunward flow away from the arc would have been puzzling if we did not have TALO optical observations. The TALO camera showed the onset of an additional arc near the zenith at times when sunward flows were detected by the radar. The arc showed up fairly suddenly at about 09:46 UT and lasted for about 6 min. We note that signatures of the sunward flow in radar maps were seen ~ 6 min prior and ~ 10 min after the arc detection.

Another expected feature of echoes in the vicinity of an auroral arc is the velocity enhancement in the area adjacent to the arc (Uspensky et al., 1983; Timofeev et al., 1987; Aikio et al., 2002). We did not find any evidence for the effect in Rankin data; this can be explained by limitations in the radar spatial resolution (45 km in range and worse in the azimuthal plane). We note that another possible reason for the weaker effect is that the polar cap arcs are not as intense as the ones in the auroral zone.

Previous publications did not show a clear picture of plasma flows around morning PC arcs (Newell et al., 2009). Carlson et al. (1988) reported a great deal of structuring in the flows. Our observations are in full agreement with this opinion.

Despite the fact that the arc was seemingly homogeneous, the velocity distribution was very patchy and the trends were often difficult to infer. Consider Fig. 4.14. For the same radar bin, say 27 in Fig. 4.14, the observed velocities were anywhere between -100 and + 100 m/s. If one scans azimuthally, at the same range, but in different beams, Fig. 4.15, again the velocity changes up to 100 m/s. One may argue that this is typical variability of the velocity but one would expect more stability for the case of a regular optical form moving at roughly constant speed in the ionosphere.

The main arc signatures in echo spectral width were similar to the case of Koustov et al. (2008); the width was enhanced in the vicinity of the arc (Fig. 4.13). Several interpretations of this result can be offered. One of these is the fact that each echo in the arc vicinity might be a collection of microscattering from various parts of the arc, both in terms of the height and the azimuth. Somewhat different areas might have slightly different velocities and their integration in one gate signal might lead to unusually broad spectra. The other explanation is strong natural non-homogeneity of the flows near the arc because of sharp plasma gradients are expected to occur which might lead to GD instability and "fingers" formation with quite different macro-characteristics.

The data available do not allow us to make definite conclusions about the magnetospheric origin of the observed PC arc. While the arc was moving duskward, the remnants of the auroral oval luminosity at the eastern edge of the camera FoV were identifiable. This suggests that the arc was formed by splitting/detaching from the oval and not by protruding into the polar cap from the midnight auroral oval. Thus, processes of merging between the IMF and Earth's magnetic field (e.g., Blomberg et al., 2005) are more likely responsible for the arc formation and dynamics as compared to the evolution of interchange instabilities (e.g., Golovchanskaya et al., 2006). Sojka et al. (1994) proposed the coupled magnetosphere-ionosphere model that considers a shear Alfven wave interacting with the ionosphere. One of their predictions is that for the background convection velocities of > 300 m/s, the wave would lead to a splitting of the initial conductance band onto fine structures and multiple arcs should be observed. In our event, the arc-associated convection flows were very close to the threshold. It is interesting to note that data in green light shows that between ~09:30 and 10:00 UT, the arc was split onto two structures separated by <100 km. Green light data after 10:00 UT

were confusing to allow for a judgment about the existence of double structure of the arc as the arc started to fade and move away from the RES zenith. It is interesting that first signs of the upcoming sunward flow channel can be traced on the RKN velocity maps up to 09:30 UT, about the time of splitting the arc onto two stripes. We note that the double structuring of the main arc has no apparent relation to the onset of the additional arc over TALO at ~ 09:45 UT. Also, after splitting, the arc separation maintained at the same distance, contrary to the theory by Sojka et al. (1994).

4.12 Conclusions

Major results of the present study can be formulated as follows:

1) A case of HF radar continuous monitoring of a PC arc moving duskward is presented. Observations were performed in the dawn sector at magnetic latitudes of ~ 77^0. Radar signatures of the moving SA form have been identified as 1) a significant echo power enhancement in the wake (dawnside) of the arc and 2) a significant increase in echo spectral width dawnward of the form. The arc was observed in the region of antisunward convection.
2) The flow channel with sunward plasma convection has been observed dawnward of the arc for ~ 20-30 min. The channel onset correlated with splitting of the main arc onto two very closely spaced arcs (as seen in green luminosity light) and onset additional arc in space between the PC arc and the poleward edge of the auroral oval.
3) Very weak magnetic perturbations associated with the motion of the PC arc passing the zenith of a magnetometer have been detected. For a magnetometer location to the west (duskward) or to the east (dawnward) of the arc the X component shows a positive deflection of ~ 15-20 nT while the Y component shows negative deflection of a comparable magnitude. The Z component shows a negative (positive) deflection for the magnetometer location to the west (east) of the SA form. Radar data indicate that it is not easy to infer the structure of the convection around the SA form on the basis of magnetometer data alone.

4) SuperDARN network global pattern estimates indicate that the local convection reversal associated with the SA form was not aligned/coinciding with the convection reversal of global-scale convection cells; rather, it was located poleward (duskward) of it. The duskward progression of the arc-associated reversal and optical arc probably reflected the mesoscale restructuring of the global-scale convection pattern from B_y^- to B_y^+ configurations.

CHAPTER 5

CONCLUSIONS AND SUGGESTIONS FOR FUTURE RESEARCH

This Thesis has two distinct areas of research. First, a statistical analysis of the Rankin Inlet PolarDARN radar echo occurrence rates has been performed by considering data for one full year of operation (2007). Measurements across the magnetic L shells have been considered so that they could be compared with across L shell observations of two other SuperDARN radars monitoring echoes from within the auroral oval, Saskatoon and Halley. Second, the Rankin Inlet radar has successfully monitor the vicinity of a morning side polar cap arc, allowing for a study of the radar signatures of the arc and the details of the plasma flows associated with the arc progression in space and time.

5.1 Conclusions

Conclusions are made on each of the objectives of this thesis separately.

5.1.1 Rankin Inlet occurrence rates

1. The radar shows preferential ranges/magnetic latitudes of ionospheric echo occurrence; the highest rates are achieved between 75^0 and 80^0 magnetic latitude. Typical average rate over a day is ~34%. Within this band, the rates vary with the magnetic local time of observations from highest values of ~40% during dawn-noon hours to lowest values of ~ 20% during early morning and dusk hours. There is a slight variation with season.

2. The second band of enhanced RKN echo occurrence is between 80^0 and 85^0 of magnetic latitude. Here typical rates are ~10% and vary significantly with season; the lowest values are achieved during summer (~3%) and the highest during winter (12%).

3. Daily average RKN echo occurrence rates of ~30% are significantly higher than daily average rates for Saskatoon, ~6%, and Halley ~1.5%.

4. The RKN rates are larger (smaller) for winter (summer) observations. Although the radar is located at relatively high geographic latitudes, and in this aspect it is closer to the Halley radar configuration, the radar does not show similar strong seasonal variation.

5. It is a fortunate combination of reasonable propagation conditions and irregularity production in the transition region between the auroral oval and polar cap that gives unusually high echo occurrence rates for the RKN radar.

6. All three radars detect the majority of echoes through the direct propagation mode at ranges ~ 800-1500 km. Optimal ranges of echo detection for the SAS and HAL radars are equatorward of the auroral oval on the dayside and thus these radars suffer here from deficiency in the irregularity production. Besides remoteness from the auroral oval, the irregularities can be prevented from development by strong sunlight. In other MLT sectors, although the irregularity production within the radar FoVs could be comparable, the auroral zone radars experience much more problems with radio wave propagation. These include strong auroral zone precipitation events that lead to radio wave absorption and bending in the E and bottom F regions so that ground scatter precludes ionospheric echo detection at optimal ranges. On the other hand, precipitation and regular density enhancement due to sunlight provide relatively frequent opportunity for the SAS radar to detect echoes through 1½ hop propagation mode at high latitudes of ~80^0 in the midnight sector and near winter noon. At these latitudes, the SAS echo occurrence rates are not as high as for the RKN radar because much less energy can be forward scattered along the path at the groud reflection and a significant amount of energy can be lost by absorption in the E region. Similar effect seems to be not working at Halley. This can be explained by low radio wave reflectivity from ice/snow permanently existing in Antarctica so that 1½ hop mode cannot happen. In addition, this radar is located even more equatorward of the auroral oval and thus the irregularity production zone is in the middle of its FoV where the radar wave bending is not optimal. Finally, the high geographic location of the HAL radar leads to general deficiency in radar wave bending.

5.1.2 Polar cap arc monitoring with the Rankin Inlet radar

1. We identified and analyzed an event of PC monitoring with RKN F region echoes. The signatures of the arc are (a) enhanced echo power and (b) enhanced spectral width of echoes in the close vicinity of the arc, mostly in its wake.

2. The arc was observed within the band of antisunward convecting plasma.

3. The arc was accompanied by the development of a flow channel with sunward plasma convection dawnward of the arc. The event lasted for ~ 20-30 min. The channel onset correlated with splitting of the main arc onto two very closely spaced arcs (as seen in green luminosity light) and the onset of an additional arc in a region between the original arc and the poleward edge of the auroral oval.

4. The global convection patterns inferred from the entire SuperDARN network observations showed that the convection reversal in the arc vicinity was not aligned/coinciding with the convection reversal of the global-scale morning convection cell; it was located poleward (duskward) of it. Thus, the reversal is rather a local phenomenon reflecting the meso-scale restructuring of the global-scale convection pattern accompanying B_y IMF fluctuations and polarity changes.

5. Only very weak magnetic perturbations (< 20 nT) were observed during the arc progression over the zenith of RES. The magnetometer signatures of the arc are (a) positive deflection in the X component for magnetometer location to the west (duskward) or to the east (dawnward) of the arc (b) negative deflection for the Y component (c) a negative (positive) deflection in the Z component for the magnetometer location to the west (east) of the SA form.

5.2 Suggestions for future research

Further work into each of the two objectives of this Thesis would provide a more comprehensive understanding of each issue. Below we suggest potential areas for expansion.

5.2.1 Echo occurrence rates

1. In this Thesis, only one year has been considered, 2007. This was the first full year of the RKN radar operation. By now, data are available for 2008 and very soon, the full set for 2009 will be completed. Also, data for the Inuvik PolarDARN radar are available since December 15, 2008. We suggest continued routine data processing of the echo occurrence rate for both radars to investigate the seasonal and solar cycle effects. A previous study by Koustov et al. (2003) indicated that the seasonal effect in the SuperDARN radar echo occurrence is very weak during years of solar cycle minimum. The situation changes drastically once the solar activity increases. The nature of the seasonal variations of echo occurrence is not well understood. Since PolarDARN radars operate at high magnetic latitudes, their data might provide additional clues to the nature of the seasonal effect.

2. Since the echo occurrence rate is affected seriously by the radio wave propagation conditions, it is highly desirable to study the electron density variations at very high magnetic latitudes. Lately, in conjunction with the International Polar Year, the incoherent scatter radar at Svalbard has been operating on a continuous basis thus providing ample of electron density data at the magnetic latitude of 82^0. The data are accessible through the Madrigal portal so that typical density profiles for various seasons can be inferred. Since magnetic latitudes of Svalbard are about the same as the latitudes at which the Rankin radio waves enter the ionosphere, it would be interesting to learn how propagation conditions change throughout a day for various seasons and how this affects the propagation modes for the PolarDARN radars. One of the potentially important issues is a strong seasonal variation of the ground scatter. Currently, it is believed that snow/ice coverage is the main reason why winter observations do not show frequent occurrence of GS.

3. It is desirable to investigate the PolarDARN radar echo occurrence rates as a function of magnetic activity. It is known that the auroral oval expands equatorward as the Kp index increases. We showed that most of the RKN echoes occur near the poleward edge of the auroral oval. It would be interesting to know if an increase in

magnetic activity would lead to a relative shift of HF echo detection zone in magnetic latitude.

5.2.2 Polar cap arcs

1. Since a PC arc is a unique and rare phenomenon, more events need to be identified and investigated. With introduction of the Inuvik PolarDARN radar, the search would be more successful. It is known that arcs in the polar cap can be detected at any MLT time. A natural expansion of the presented work would be observations of the evening sector arcs that are detaching from the auroral oval and drifting dawnward. In the evening sector there is a chance to get concurrent data from one of the DMSP satellites. This is because of special configuration of their trajectories. DMSP provides information on particles and fields and thus gives an opportunity to place convection measurements in a broader context. Lately, several ionosondes have been installed in the Canadian Arctic, at Rankin Inlet and Eureka, both within the Rankin Inlet FoV. The hope is that their data, being added to the RKN data, would provide more extensive coverage and ease interpretation of PolarDARN data, especially if only one radar shows echoes.

2. Of special interest would be cooperative work with the newly installed Resolute Bay incoherent scatter radar (RISR) that has unprecedented spatial and reasonable (1-2 minutes) temporal resolution. Combination of PolarDARN's more global coverage with RISR local measurements would permit studies of the convection perturbations associated with the generation and progression of PC arcs.

3. Observations of auroras at Taloyak provide numerous opportunities for joint work with the Rankin Inlet radar. Contrary to Resolute Bay, the distance from Rankin Inlet to Taloyak is only ~ 900 km. We showed in Chapter 3 that detection of echoes at these ranges is significantly more frequent than at Resolute Bay ranges of ~1400 km. Joint Taloyak-Rankin data would allow one to study plasma flows at the poleward edge of the auroral oval, near various optical forms that are often seen in this region of transition from the auroral oval to the polar cap.

References:

Aikio, A. T., T. Lakkala, A. Kozlovsky, and P. J. S. Williams, Current systems of stable drifting auroral arcs in the evening sector, J. Geophys. Res., 107, 1424, doi:10.1029/2001JA009172, 2002.

Akasofu, S. I., The development of the auroral substorm, Planet. Space Sci., 12, 273–282, 1964.

Akasofu, S.-I., Recent progress in studies of DMSP auroral photographs, Space Science Reviews, 19, 169-215, 1976.

Axford, W. I., and C. O. Hines, A unifying theory of high-latitude geophysical phenomena and geomagnetic storms, Can. J. Phys., *39*, 1433-1464, 1961.

Ballatore, P., J.-P. Villain, N. Vilmer, and M. Pick, The influence of the interplanetary medium on SuperDARN radar scattering occurrence, Ann. Geophys., 18, 1576-1583, 2001.

Berkey, F. T., and Y. Kamide, On the distribution of global auroras during intervals of magnetic quiet, J. Geophys. Res. 81, 4701–4714,1976.

Blomberg, L. G., J. A. Cumnock, I. I. Alexeev, E. S. Belenkaya, Bobrovnikov, S. Yu, and V. V. Kalegaev, Transpolar aurora: time evolution, associated convection patterns, and a possible cause, Ann. Geophys., 23, 1917–1930, 2005.

Carlson, H. C., Jr. R. A. Heelis, E. J. Weber, and J. R. Sharber, Coherent mesoscale convection patterns during northward interplanetary magnetic field, J. Geophys. Res., 93, 14501-14514, 1988.

Carlson, H. C., and S. W. H. Cowley, Accelerated polar rain electrons as the source of Sun-aligned arcs in the polar cap during northward interplanetary magnetic field conditions, J. Geophys. Res. 110, A05302, doi:10.1029/2004JA010669, 2005.

Chang, S.-W., J. D. Scudder, J. B. Sigwarth, L. A. Frank, N. C. Maynard, W. J. Burke, W. K. Peterson, E .G. Shelley, R. Friedels, J. B. Blake, R. A. Greenwald, R. P. Lepping, G. J. Sofko, J.-P. Villain, and M. Lester, A comparison of a model for the theta aurora with observations from Polar, Wind, and SuperDARN, J. Geophys. Res., 103, 17367-17390, 1998.

Chapman, S., and V. C. A. Ferraro. A new theory of magnetospheric storms: The initial phase, J. Geophys. Res., 36, 77, 1931.

Cravens, T. E., Physics of Solar System Plasmas, Cambridge University Press, New York, 1997.

Dungey, J. W., Interplanetary magnetic field and the auroral zones, Phys. Rev. Lett., 6, 47, 1961.

Danskin, D. W., A. V. Koustov, T. Ogawa, N. Nishitani, S. Nozawa, S. E. Milan, M. Lester, and D. André, On the factors controlling occurrence of F-region coherent echoes, Ann. Geophys., 20, 1385-1397, 2002.

Danskin, D. W., A. V. Koustov, T. Ogawa, N. Nishitani, S. Nozawa, S. E. Milan, M. Lester, and D. André, On the factors controlling occurrence of F-region coherent echoes, Ann. Geophys., 20, 1385-1397, 2002.

Eriksson, S., G. Provan, F. J. Rich, M. Lester, S. E. Milan, S. Massetti, J. T. Gosling, M. W. Dunlop, and H. Re`me, Electrodynamics of a split-transpolar aurora, J. Geophys. Res., 111, A11319, doi:10.1029/2006JA011976, 2006.

Eather, R., and S. Mende, Systematics in Auroral Energy Spectra, J. Geophys. Res., 77, 4, doi:10.1029/JA077i004p00660, 1972.

Fejer, B. G., and M. C. Kelley, Ionospheric irregularities, Rev. Geophys., 18, 401-454, 1980.

Feldstein, Ya. I., and G.V. Starkov, Dynamics of auroral belt and polar geomagnetic disturbances, Planet. Space Sci., 15, 209, 1967.

Fiori, R. A. D., A. V. Koustov, D. Boteler, and R. A. Makarevich, PCN magnetic index and average convection velocity in the polar cap inferred from SuperDARN radar measurements, J. Geophys. Res., 114, A07225, doi:10.1029/2008JA013964, 2009.

Fitzgerald, G. F., Sunspots and magnetic storms, The Elcetrician, 30, 48, 1892.

Fitzgerald, G. F., Sunspots and magnetic storms, comet tails, atmospheric electicity and aurorae, The electrician, 46, 287, 1900.

Frank, L. A., J. D. Craven, J. L. Burch, and J. D. Winningham, Polar views of the Earth's aurora with Dynamic Explorer, Geophys. Res. 9 ,1001–1004,1982.

Fukumoto, M., N. Nishitani, T. Ogawa, N. Sato, H. Yamagishi, and A. S. Yukimatu, Statistical analysis of echo power, Doppler velocity and spectral width obtained with the Syowa South HF radar, Advances in Polar Upper Atmosphere Research, 13, 37-47, 1999.

Fukumoto, M., N. Nishitani, T. Ogawa, N. Sato, H. Yamagishi, and A. S. Yukimatu, Statistical study of Doppler velocity and echo power around 75^0 magnetic latitude with the Syowa East HF radar, Advances in Polar Upper Atmosphere Research, 14, 93-102, 2000.

Fukunishi, H., Y. Takahashi, T. Nagatsuma, T. Mukai, and S. Machida, Latitudinal structure of nightside field-aligned currents and their relationship to the plasma sheet regions, J. Geophys. Res., 98, 11,235-11,255, 1993.

Gallagher, H. A., Jr., Radar and optical observations of plasma convection associated with very high-latitude auroral arcs, PhD Thesis, Boston College, USA, 1997.

Gillies, R. G., G. C. Hussey, G. J. Sofko, K. A. McWilliams, R. A. D. Fiori, P. Ponomarenko, and J.-P. St.-Maurice, Improvement of SuperDARN velocity measurements by estimating the index of refraction in the scattering region using interferometry, J. Geophys. Res., 114, A07305, doi:10.1029/2008JA013967, 2009.

Golovchanskaya, I. V., A. Kullen, Y. P. Maltsev, and H. Biernat, Ballooning instability at the plasma sheet–lobe interface and its implications for polar arc formation, J. Geophys. Res., 111, A11216, doi:10.1029/2005JA011092, 2006.

Gorin, J. D., Velocity of decameter electrojet irregularities under strongly driven conditions, MSc Thesis, U of Saskatchewan, Saskatoon, SK, Canada, 2008.

Greenwald, R. A., K. B. Baker, J. R. Dudeney, M. Pinnock, T. B. Jones, C. Thomas, J.-P. Villain, J.-C. Cerisier, C. Hanuise, R. D. Hunsucker. G. J. Sofko, J. Koehler, E. Nielsen, and R. Pellinen, DARN/SUPERDARN, A global view of the dynamics of high-latitude convection, Space Sci. Rev., 71, 761-796, 1995.

Hamza, A. M., M. Huber, W. Lyatsky, A. V. Koustov, D. Andre, and G. Sofko, Eastward convection jet at the poleward boundary of the nightside auroral oval, Geophys. Res. Lett, 27, 2809-2812, 2000.

Hanuise, C., High-latitude ionospheric irregularities: a review of recent results, Radio Sci., 18, 1093-1121, 1983.

Hargreaves, J. K.: The Solar-Terrestrial Environment, Cambridge University Press, Cambridge, UK, 1992.

Hosokawa, K., T. Iyemori, A. S. Yukimatu, and N. Sato, Source of field-aligned irregularities in the subauroral F region as observed by the SuperDARN radars, J. Geophys. Res., 106, 24713-24731, 2001.

Huber, M., HF radar echo statistics and spectral studies using SuperDARN, M.Sc. Thesis, U of Saskatchewan, Saskatoon, 1999.

Ismail, S., D. D. Wallis, and L. L. Cogger, Characteristics of polar cap Sun-aligned arcs. J. Geophys. Res. 82, 4741–4749, 1977.

Kelly, M.C.: The Earth's Ionosphere, The Academic Press, San Diego, 1989.

Keskinen, M. J., and S. L. Ossakow, Nonlinear evolution of plasma enhancements in the auroral ionosphere. 1. Long wavelength irregularities, J. Geophys. Res., 87, 144-150, 1982.

Koustov, A. V., G. J. Sofko, D. André, D. W. Danskin, and L. V. Benkevitch, Seasonal variation of HF radar F region echo occurrence in the midnight sector, J. Geophys. Res., 109, A06305, doi:10.1029/2003JA010337, 2004.

Koustov, A. V., D. W. Danskin, R. A. Makarevitch, and J. D. Gorin, On the relationship between the velocity of E-region HF echoes and ExB plasma drift, Ann. Geophys., 23, 371–378, 2005.

Koustov, A. V., R. A. Drayton, R. A. Makarevich, K. A. McWilliams, J.-P. St-Maurice, T. Kikuchi, and H. U. Frey, Observations of high-velocity SAPS-like flows with the King Salmon SuperDARN radar, Ann. Geophys., 24, 1591–1608, 2006.

Koustov, A. V., Hosokawa, N. Nishitani, T. Ogawa, and K. Shiokawa, Rankin Inlet PolarDARN radar observations of duskward moving Sun-aligned optical forms, Ann. Geophys., 26, 2711–2723, 2008.

Koustov, A., K. Hosokawa, N. Nishitani, T. Ogawa, K. Shiokawa, and H. Liu, PolarDARN radar observations of plasma flows associated with morning polar cap forms detaching from the auroral oval, 2009 AGU Fall Meeting, Dec 13-18, 2009, San Francisco, Ca, USA, abstract SM33A-1555.

Kullen, A., M. Brittnacher, J. A. Cumnock, and L. G. Blomberg, Solar wind dependence of the occurrence and motion of polar auroral arcs: A statistical study, J. Geophys. Res., 107, 1362, doi:10.1029/2002JA009245, 2002.

Lassen, K., and C. Danielsen, Quiet time pattern of auroral arcs for different directions of the interplanetary magnetic field in the Y-Z plane. J. Geophys. Res. 83, 5277–5284, 1978.

Liou, K., J. M. Ruohoniemi, P. T. Newell, R. Greenwald, C.-I. Meng, and M. R. Hairston, Observations of ionospheric plasma flows within theta auroras, J. Geophys. Res., 110, A03303, doi:10.1029/2004JA010735, 2005.

Liu, H., A. Koustov, K. Hosokawa, N. Nishitani, T. Ogawa, and K. Shiokawa, Plasma flows around polar cap arcs as seen by the PolarDARN radars, China's 13th solar-terrestrial space physics national meeting, Yinchuan, China, August 16-20, 2009.

Milan, S. E., B. Hibert, and A. Grocott, Formation and motion of a transpolar arc in response to dayside and nightside reconnection, J. Geophys. Res., 110, A01212, doi: 10.1029/2004JA010835, 2005.

Milan, S. E., J. A. Davies, and M. Lester, Coherent HF radar backscatter characteristics associated with auroral forms identified by incoherent radar techniques: A comparison of CUTLASS and EISCAT observations, J. Geophys. Res., 104, 22,591-22,604, 1999.

Milan, S. E., T. K. Yeoman, M. Lester, E. C. Thomas, and T. B. Jones, Initial backscatter occurrence statistics from the CUTLASS HF radars, Ann. Geophys., 15, 703-718, 1997.

Newell, P. T., K. Liou, and G. R. Wilson, Polar cap particle precipitation and aurora: Review and commentary, J. Atmos. and Solar-Terrestrial Physics, 71, 199–215. 2009.

Parker, E. N., Dynamics of the interplanetary gas and magnetic fields, Astrophysical Journal, 128, 664-676, 1958.

Parkinson, M. L., J. C. Devlin, H. Ye, C. J. Waters, P. L. Dyson, A. M. Breed, and R. J. Morris, On the occurrence and motion of decameter-scale irregularities in the sub-auroral, auroral, and polar cap ionosphere, Ann. Geophys., 21, 1847-1868, 2003.

Peredo M., J. A. Slavin, E. Mazur, and S. A. Curtis, Three-dimensional position and shape of the bow shock and their variation with Alfvenic sonic and magnetosonic Mach numbers and interplanetary magnetic field orientation, J. Geophys. Res., 100, 7907-7916, 1995.

Rodriguez, J. V., C. E., Valladares, K., Fukui, H. A., Gallagher, Antisunward decay of polar cap arcs, J. Geophys. Res., 102, A12, doi: 10.1029/97JA01727, 1997.

Ruohoniemi, J. M., and K. B. Baker, Large-scale imaging of high-latitude convection with Super Dual Auroral Radar Network HF radar observations, J. Geophys. Res., 103, 20,797-20,811, 1998.

Ruohoniemi, J. M., and R. A. Greenwald, Rates of scattering occurrence in routine HF radar observations during solar cycle maximum, Radio Sci., 32, N3, 1051-1070, 1997.

Seran, E., M. Godefroy, K. Kauristie, J.-C. Cerisier, J.-J. Berthelier, M. Lester, and L.E. Sarri, What can we learn from HF signal scattered from a discrete arc., Ann. Geophys., 27, 1887-1800, 2009.

Shepherd, S. G., R. A. Greenwald, and J. M. Ruohoniemi, Cross polar cap potentials measured with Super Dual Auroral Radar Network during quasi-steady solar wind and interplanetary magnetic field conditions, J. Geophys. Res., 107(A7), 1094, doi: 10.1029/2001JA000152, 2002.

Shiokawa, K., K. Yumoto, K. Hayashi, T. Oguti, and D. J. McEwen, A statistical study of the motions of auroral arcs in the high-latitude morning sector, J. Geophys. Res., 100, 21979-21985, 1995.

Shiokawa, K., M. Katoh, M. Satoh, M. K. Ejiri, T. Ogawa, T. Nakamura, T. Tsuda, and R. H. Wiens, Development of optical mesosphere thermospheric imagers (OMTI), Earth, Planets, Space, 31, 887-896, 1999.

Shiokawa, K., T. Ogino, K. Hayayshi, and D. J. McEwen, Quasi-periodic poleward motions of morning side Sun-aligned arcs: A multi event study, J. Geophys. Res., 102, 24325-24332, 1997.

Sibeck, D. G., R. E. Lopez, and E. C. Roelof, Solar Wind control of the magnetopause shape, location, and motion, J. Geophys. Res**.,** 96, 5489 -5495, 1991.

Sibeck, D. G., R. E. Lopez, and E. C. Roelof, Reply to comment by M. W. Dunlop, M. P. Freeman, and C. J. Farrugia on "Solar wind control of the magnetopause shape, location and motion", J. Geophys. Res., 97, 10879 – 10882, 1992.

Smith, C. W., M. H. Acuna, L. F. Burlaga, J. L. Heureux, N. F. Ness, and J. Schiefele, The ACE magnetic field experiment, Space Sci. Rev., 86, 613 – 632, 1998.

Sojka, J. J., L. Zhu, D. J. Crain, and R. W. Schunk, Effect of highlatitude ionospheric convection on Sun-aligned polar cap arcs, J. Geophys. Res., 99, 8851–8863, 1994.

Sonett, C. P., Coupling of the Solar Wind and the Exosphere, Phys. Rev. Lett. 5, 46–48, DOI: 10.1103/PhysRevLett.5.46, 1960.

Starkov, G. V., J. Oksman, M. V. Uspensky, and A.V. Kustov, On the dependence of radar aurora amplitude on ionospheric electron density, J. Geophysics, 52, 49-52, 1983.

Timofeev E. E., M. K. Vallinkoski, T. V. Kozelova, A. G. Yahnin, and R. J. Pellinen, Systematics of arc-associated electric fields and currents as inferred from radar backscatter measurements, J. Geophysics., 61, 122-137, 1987.

Tsunoda, R. T., High latitude irregularities: A review and synthesis, Rev. Geophys., 26, 719-760, 1988.

Uspensky M. V., R. J. Pellinen, W. Baumjohann, G. V. Starkov, E. Nielsen, G. Sofko, and K. U. Kaila, Spatial variations of ionospheric conductivity and radar auroral amplitude in the eastward electrojet region during pre-substorm conditions, J. Geophysics, 52, 40-48, 1983.

Uspensky, M. V., P. Eglitis, H. Opgenoorth, G. Starkov, T. Pulkkinen, and R. Pellinen, On auroral dynamics observed by HF radar: 1. Equatorward edge of the afternoon-evening diffuse luminosity belt, Ann. Geophys., 18, 1560-1575, 2001.

Valladares, C. E., and H. C. Carlson Jr., The electrodynamic, thermal, and energetic character of intense Sun-aligned arcs in the polar cap, J. Geophys. Res., 96, 1379-1400, 1991.

Valladares, C. E., H. C. Jr. Carlson, and K. Fukui, Interplanetary magnetic field dependency of stable Sun-aligned polar cap arc, J. Geophys. Res., 99, 6247-6272, 1994.

Vallance Jones, A., Aurora, D. Reidel Publ. Co, Dordrecht, Holland, 1974.

Villain, J.P., R.A., Greenwald, K.B., Baker, and Ruohoniemi, J.M., HF radar observations of E region plasma irregularities produced by oblique electron streaming, J. Geophys. Res., 92, 12,327-12,342, 1987.

Villain, J.-P., R. André, M. Pinnock, R. A. Greenwald, and C. Hanuise, A Statistical study of the Doppler spectral width of high-latitude ionospheric F-region echoes recorded with SuperDARN coherent HF radars, Ann. Geophys., 20, 1769-1781, 2002.

Yeoman, T. K., G. Chisham, L. J. Baddeley, R. S. Dhillon, T. J. T. Karhunen, T. R. Robinson, A. Senior, and D. M. Wright, Mapping ionospheric backscatter measured by the SuperDARN HF radars – Part 2: Assessing SuperDARN virtual height models, Ann. Geophys., 26, 843-852, 2008.

Zhang, Y., D. J. McEwen, N. Konga, J. J. Sojka, and L. Zhu, Horizontal electrojet associated with the sun-aligned arcs., J. Atmos. and Solar-Terr. Phys., 61, 1249-1257, 1999.

Zesta E., E. Donovan, L. Lyons, G. Enno, J. S. Murphree, and L. Cogger, Two-dimensional structure of auroral poleward boundary intensifications, J. Geophys. Res., 107, 1350, doi:10.1029/2001JA000260, 2002.

Zhu, L., C. E. Valladares, J. J. Sojka, R. W. Schunk, and D. J. Crain, Model-observation comparison of multiple polar cap arcs, J. Geophys. Res., 101, 323-333, 1996.

Zhu, L., R. W. Schunk, and J. J. Sojka, Polar cap arcs: a review, J. Atmos. Terr. Phys., 59, 1087-1126, 1997.

Appendix A:

Linear growth rate of the gradient-drift instability in the high-latitude F region

The gradient-drift (GD) instability occurs in the presence of background gradient of the plasma density oriented perpendicularly to the crossed electric and magnetic fields. Such situation is typical for the high-latitude ionosphere where background plasma gradients are frequent due to particle precipitations.

To derive expression for the GD instability growth rate in the high-latitude F region, we consider the following geometry: the Earth's magnetic field is vertical and oriented in the direction opposite to the *z* axis, the electric field is along the *x* axis and the plasma gradient $\boldsymbol{e}_y \frac{1}{L} = \frac{1}{n_0}\frac{dn_0}{dy}$ is along the *y* axis, Figure A1.

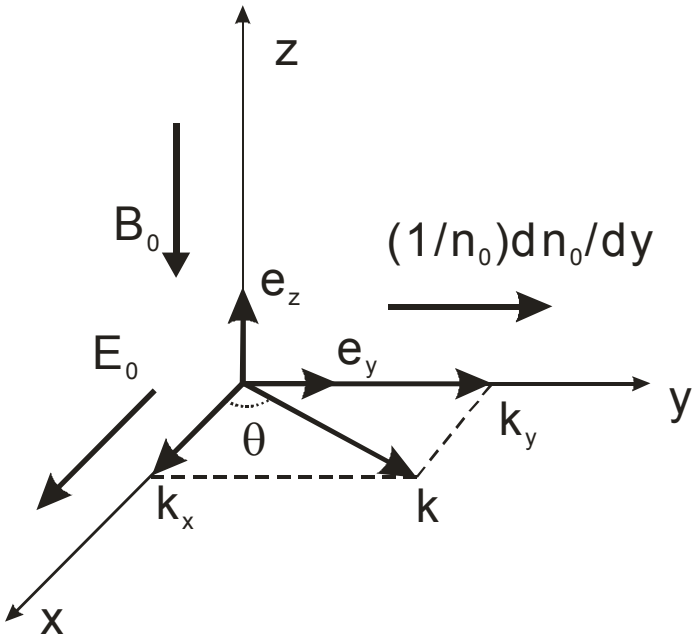

Figure A1. Configuration of the electric and magnetic fields and the background gradient of the electron density adopted for the analysis.

We start from simplified equations of charged particle motion that are considered to be valid for the heights below ~200 km where collisions between charged particles can be neglected (Kelley, 1989):

$$m_\alpha \frac{d\mathbf{V}_\alpha}{dt} = q_\alpha \left[\mathbf{E} + \mathbf{V}_\alpha \times \mathbf{B}\right] - m_\alpha \nu_{\alpha n} \mathbf{V}_\alpha - \frac{1}{n_\alpha} \nabla (n_\alpha T_\alpha) , \qquad \text{(A1)}$$

where α=*i,e* represents either ions or electrons, and, for each species α , $\boldsymbol{V}_a$ is the velocity, ν_{an} is the collision frequency with neutrals, m_α and q_α are the mass and charge, $T_\alpha = k_B T_\alpha^{/}$ is the temperature in Kelvins multiplied by the Boltzman constant k_B. For the analysis, we also use the continuity equations for each species α :

$$\frac{\partial n_\alpha}{\partial t} + \nabla \cdot (n_\alpha \mathbf{V}_\alpha) = 0 . \qquad \text{(A2)}$$

We assume that every quantity in equations (A1) and (A2) has the background value and small perturbation, e.g. for the electron density:

$$n_\alpha = n_{o\alpha} + \delta n_\alpha ; \quad \delta n_\alpha << n_{o\alpha} . \qquad \text{(A3)}$$

The background conditions for the velocities of the electrons and ions have been investigated in Chapter 1. Here we consider the perturbed quantities. The strategy is to find expressions for the velocities $\delta \boldsymbol{V}_\alpha$ in terms of $\delta \boldsymbol{E}$ (or electrostatic potential $\delta\varphi$) from (A1) and then use them in (A2). Obtained system of two equations for two unknowns would be analyzed.

We assume that the considered perturbations are of a sinusoidal type, i.e. all quantities are proportional to $\exp(-i\omega t + i\boldsymbol{kr})$, and they are slow $\omega << \nu_{an}$ so that the left-hand side term in (A1) can be omitted.

Equations (A1) for the perturbed quantities (so called, linearized equations) can be written as

$$0 = \frac{q_\alpha}{m_a}\left[\delta\mathbf{E} + \delta\mathbf{V}_\alpha \times \mathbf{B}_0\right] - \nu_{an}\delta\mathbf{V}_\alpha - \frac{T_\alpha}{m_\alpha}\frac{\nabla(\delta n_\alpha)}{n_{0\alpha}} . \qquad \text{(A4)}$$

While arriving to (A4), we assumed that there are no temperature changes in perturbations ($\delta T_\alpha = 0$). We note that equations (A4) are very similar for the electrons and ions except of different sign of the charge. For this reason, we temporally write equations without indices and introduce them back once we consider equations for each species individually.

Equation (A4) for the electrons can be presented in the form:

$$0 = -\frac{e}{m}\delta\mathbf{E} + \Omega\delta\mathbf{V}\times\boldsymbol{e}_z - \nu\delta\mathbf{V} - \frac{T}{m}i\boldsymbol{k}\frac{\delta n}{n};\quad e = |q|. \tag{A5}$$

For simplicity we consider below one specific Fourier component $(\omega, \boldsymbol{k})$ of the perturbation and assume that the mode propagates exactly perpendicular to the magnetic field $\boldsymbol{k} = (k_x, k_y);\quad k_z = 0$. By assuming potential electric field $\delta\boldsymbol{E} = -\nabla\delta\varphi = -i\boldsymbol{k}\delta\varphi$, equation (A5) can be expressed in components as

$$ik_x(\frac{e}{m}\delta\varphi) + \Omega\delta V_y - \nu\delta V_x - ik_x\frac{T}{m}\frac{\delta n}{n} = 0; \tag{A6}$$

$$ik_y(\frac{e}{m}\delta\varphi) - \Omega\delta V_x - \nu\delta V_y - ik_y\frac{T}{m}\frac{\delta n}{n} = 0. \tag{A7}$$

Equations (A6) and (A7) can be presented in a matrix form:

$$\hat{A}\cdot\begin{pmatrix}\delta V_x\\ \delta V_y\end{pmatrix} = i\begin{pmatrix}k_x\\ k_y\end{pmatrix}\cdot B;\quad \hat{A} = \begin{vmatrix}-\nu & \Omega\\ -\Omega & -\nu\end{vmatrix};\ B = -\frac{e}{m}\delta\phi + \frac{T}{m}\frac{\delta n}{n}. \tag{A8}$$

Solution of (A8) is

$$\delta V_x = \frac{1}{Det(\hat{A})}\begin{vmatrix}iBk_x & \Omega\\ iBk_y & -\nu\end{vmatrix} \approx \frac{i}{\Omega^2}\left(-Bk_x\nu - Bk_y\Omega\right);\quad Det(\hat{A}) = \nu^2 + \Omega^2 \approx \Omega^2; \tag{A9}$$

$$\delta V_y = \frac{1}{Det(\hat{A})}\begin{vmatrix} -\nu & iBk_x \\ -\Omega & iBk_y \end{vmatrix} \approx \frac{i}{\Omega^2}\left(-Bk_y\nu + Bk_x\Omega\right); \quad Det(\hat{A}) = \nu^2 + \Omega^2 \approx \Omega^2. \quad \text{(A10)}$$

Here we used the fact that in the ionospheric F region $\nu << \Omega$ for both the electrons and ions.

Linearized continuity equations (A2) are:

$$(-i\omega + i\mathbf{k}\mathbf{V}_0)\frac{\delta n}{n} + (i\boldsymbol{k}\boldsymbol{\delta V} + \frac{1}{L}\delta V_y) = 0. \quad \text{(A11)}$$

Using (A9) and (A10), one can evaluate

$$\begin{aligned} &ik_x\delta V_x + ik_y\delta V_y = \frac{1}{\Omega^2}(Bk_x^2\nu + Bk_y^2\nu) = \\ &= \frac{\nu}{\Omega^2}(k_x + k_y^2)B = \frac{\nu}{\Omega^2}k_\perp^2 B = \frac{\nu}{\Omega^2}k_\perp^2(-\frac{e}{m}\delta\varphi + \frac{T}{m}\frac{\delta n}{n}); \end{aligned} \quad \text{(A12)}$$

$$\frac{1}{L}\delta V_y \approx \frac{1}{L}\cdot\frac{i}{\Omega}\cdot k_x(-\frac{e}{m}\delta\varphi + \frac{T}{m}\frac{\delta n}{n}). \quad \text{(A13)}$$

Combining (A11)-(A13), one gets

$$\frac{\delta n}{n}(-i\omega + i\mathbf{k}\mathbf{V}_0 + \frac{\nu}{\Omega^2}\frac{T}{m}k_\perp^2) + \frac{\delta\varphi}{m}e(-\frac{\nu}{\Omega^2}k_\perp^2 - \frac{i}{\Omega}\frac{k_x}{L}) = 0. \quad \text{(A14)}$$

Equations (A14), written for electrons and ions separately, are

$$\frac{\delta n}{n}\xi_e + \frac{e}{m_e}\beta_e\delta\varphi = 0; \quad \text{(A15)}$$

$$\frac{\delta n}{n}\xi_i - \frac{e}{m_i}\beta_i\delta\varphi = 0, \quad \text{(A16)}$$

where the following abbreviations were introduced:

$$\xi_e = -i\omega + i\mathbf{k}\mathbf{V}_{0e} + \frac{\nu_{en}}{\Omega_e^2}\frac{T_e}{m_e}k_\perp^2; \quad \beta_e = -\frac{\nu_{en}}{\Omega_e^2}k_\perp^2 - \frac{i}{\Omega_e}\frac{k_x}{L}; \tag{A17}$$

$$\xi_i = -i\omega + i\mathbf{k}\mathbf{V}_{0i} + \frac{\nu_{in}}{\Omega_i^2}\frac{T_i}{m_i}k_\perp^2; \quad \beta_i = -\frac{\nu_{in}}{\Omega_i^2}k_\perp^2 + \frac{i}{\Omega_i}\frac{k_x}{L}. \tag{A18}$$

The system of equations (A15)-(A16) has a non-trivial solution if its determinant is zero. Thus, we arrive to the following equation (called the dispersion equation):

$$\xi_e\beta_i + \xi_i\beta_e\frac{m_i}{m_e} = 0$$

or more explicitly

$$\begin{aligned}&\left[-i\omega_R + i\mathbf{k}\mathbf{V}_{0e} + \frac{\nu_{en}}{\Omega_e^2}\frac{T_e}{m_e}k_\perp^2\right]\cdot\left[-\frac{\nu_{in}}{\Omega_i^2}k_\perp^2 + \frac{i}{\Omega_i}\frac{k_x}{L}\right] + \\ &\left[-i\omega_R + i\mathbf{k}\mathbf{V}_{0i} + \frac{\nu_{in}}{\Omega_i^2}\frac{T_i}{m_i}k_\perp^2\right]\cdot\left[-\frac{\nu_{en}}{\Omega_e\Omega_i}k_\perp^2 - \frac{i}{\Omega_i}\frac{k_x}{L}\right] = 0.\end{aligned} \tag{A19}$$

To analyze (A19), we assume that the sinusoidal perturbation increases its amplitude slowly as compared to the frequency of the wave

$$\omega = \omega_R + i\gamma; \quad |\gamma| << \omega_R. \tag{A20}$$

The real part of (A19) is then

$$\begin{aligned}&-\gamma\frac{\nu_{in}}{\Omega_i^2}k_\perp^2 - \frac{\nu_{en}\nu_{in}}{\Omega_e^2\Omega_i^2}\frac{T_e}{m_e}k_\perp^4 + (\omega_R - \mathbf{k}\mathbf{V}_{0e})\frac{k_x}{\Omega_i L} - \\ &-\gamma\frac{\nu_{en}}{\Omega_e\Omega_i}k_\perp^2 - \frac{\nu_{en}\nu_{in}}{\Omega_e\Omega_i^3}\frac{T_i}{m_i}k_\perp^4 - (\omega_R - \mathbf{k}\mathbf{V}_{0i})\frac{k_x}{\Omega_i L} = 0\end{aligned}, \tag{A21}$$

which gives for $\frac{\nu_{in}}{\Omega_i} >> \frac{\nu_{en}}{\Omega_e}$ (valid in the F region)

$$\gamma = \frac{\Omega_i^2}{\nu_i} \frac{\mathbf{k}(\mathbf{V}_{0i} - \mathbf{V}_{0e})}{k_\perp^2} \frac{k_x}{\Omega_i L} - \frac{\Omega_i^2}{\nu_i} \frac{\nu_{en}\nu_{in}}{\Omega_e \Omega_i^3} \frac{T_e + T_i}{m_i} k_\perp^2 \tag{A23}$$

We now take into account the fact that at the F-region heights (see Chapter 1 for appropriate expressions):

$$\mathbf{k}(\mathbf{V_{0i}} - \mathbf{V_{0e}}) = k_x(V_{0ix} - V_{0ex}) + k_y(V_{0iy} - V_{0ey}) \approx \frac{\nu_i}{\Omega_i} k_x V_0, \tag{A24}$$

where $V_0 = E_0 \big/ B_0$ is the magnitude of the Hall (**ExB**) drift. Introducing the ion-acoustic speed $C_S^2 = \frac{T_e + T_i}{m_i}$, coefficient of the cross-field diffusion $D_\perp = \frac{\nu_{en}}{\Omega_e \Omega_i} C_s^2$, and the angle θ of the vector $\boldsymbol{k}$ with respect to the x axis (Fig. A1), the last expression has a more compact form:

$$\gamma = \frac{k_x^2 V_0}{k_\perp^2 L} - k_\perp^2 D_\perp = \frac{V_0}{L} \cos^2\theta - k_\perp^2 D_\perp. \tag{A25}$$

More general expression for the case of $k_z \neq 0$ has been given by Keskinen and Ossakow (1982):

$$\gamma = \frac{\frac{1}{L}\frac{E_0}{B}}{(\frac{k_z}{k_x}\frac{\Omega_e \Omega_i}{\nu_{en}\nu_{in}})^2 + 1} - k_\perp^2 D_\perp - k_z^2 D_{//}, \tag{A26}$$

where $D_{//} = \frac{C_s^2}{\nu_{in}}[1 + \frac{(\nu_{in}/\Omega_i)^2}{\nu_{en}\nu_{in}/\Omega_e\Omega_i + (k_z^2/k_x^2)}]$. Using typical auroral F region parameters $\nu_{in}/\Omega_i = 10^{-2}$, $\nu_{en}/\Omega_e = 10^{-4}$, $E_0 = 10\ mV/m$, $|k_z/k_x| = 10^{-6}$, $L = 10\ km$, $Cs = 450\ m/s$ (so that $D_\perp = 0.21\ m^2/s$ and $D_{//} \approx 10^7\ m^2/s$), one can find that the GD instability has growth time of $\gamma^{-1} \approx 1000\ s$ for the irregularity wavelength of 30 m. The growth time increases significantly (the GD instability is more difficult to start) for modes propagating non-orthogonally to the magnetic field line.

Appendix B:

Estimation of the time delay for an IMF disturbance propagation from the ACE satellite location to the high-latitude ionosphere

In this Thesis, an attempt has been made to relate the onset of the polar cap arc and perturbation of the interplanetary magnetic field (IMF). Also, the SuperDARN convection maps were built by applying the FIT technique of Ruohoniemi and Baker (1998). Both tasks required an estimate of the disturbance propagation time from the point of IMF measurements on the ACE satellite to the high-latitude ionosphere. To accomplish this, the method introduced by Shepherd et al. (2002) was adopted. Namely, the delay time was assumed to be comprised of three parts: the solar wind advection time (τ_{sw}), the magnetosheath transit time (τ_{ms}), and the Alfven transit time along magnetic field lines from the subsolar magnetopause to the ionosphere (τ_{alf}):

$$\begin{aligned} \tau_{sw} &= (X_{sc} - X_{bs}) / V_{sw} ; \\ \tau_{ms} &= (X_{bs} - X_{mp}) / V_{sw} \times 8; \\ \tau_{alf} &= 2 \text{ min}, \end{aligned} \qquad \text{(A.1)}$$

where X_{sc} is the ACE satellite position projected onto the Sun-Earth line, X_{bs} is the subsolar bow shock location (see Peredo et al., 1995), V_{sw} is the solar wind velocity, X_{mp} is the distance to the subsolar magnetopause (see Sibeck et al., 1991; 1992). The factor of 8 in equation (A.1) is due to the slowing of the plasma in the magnetosheath.

Following the above papers, one can estimate:

$$X_{mp} = (p/p_0)^{-0.15} (11.3 + 0.26\ B_z)\ (R_E); \quad X_{bs} = 1.46\ X_{mp}. \qquad \text{(A.2)}$$

Here p is the solar wind pressure and p_0=2.04 nPa. The IMF parameters were obtained from the ACE magnetometer instrument (Smith et al., 1998).

Appendix C:

Major IDL program for plotting Rankin Inlet radar parameters

```
@/home/stk/idl/lib/oldfit.pro
@/home/stk/usr/code/src.idl/sasgenlib.pro
@/home/stk/idl/lib/time.pro
@/home/stk/idl/lib/datamap.pro
@/home/stk/idl/lib/.pro
@/home/stk/idl/lib/fitlib.pro
@/home/stk/idl/lib/rprm.pro
@/home/stk/idl/lib/genlib.pro
PRO run_example
      fitfile = '20071107'
      fitloc = '/2007/11/'
      shr = 9
      smn = 0
      ehr = 10
      emn = 0
      fit_avg_plot,shr,smn,ehr,emn,fitfile+'.C0.rkn.fitacf','rank/'
END
;NOTE: program currently not set up to handle the end of a day, after
last scan in file program will get stuck in an infinite loop
PRO fit_avg_plot,$;function call
                 hr,$;start hour
                 mn,$;start minute
                 e_hr,$;end hour
                 e_mn,$;end minute
                 fitfile_name,$;fit file name
                 loc;file location string
print,fitfile_name
      station = 'Rankin'
      IF ( STRPOS( fitfile_name, 'gz') NE (-1) ) THEN BEGIN
            print,'gzip compressed files cannot be read: ',
fitfile_name
      ENDIF
      IF ( STRPOS( fitfile_name, 'bz2') NE (-1) ) THEN BEGIN
            print,'bzip2 compressed files cannot be read: ',
fitfile_name
      ENDIF
      IF (( STRPOS( fitfile_name, 'fitacf') EQ (-1) ) AND
( STRPOS( fitfile_name, 'fit') EQ (-1) ) )THEN BEGIN
            print,'This is neither an old style nor a new style fit
file: ', fitfile_name
      ENDIF
      new_file= ( STRPOS( fitfile_name, 'fitacf') NE (-1) )
      IF new_file THEN BEGIN
            ifileptr= FitOpen( fitfile_name, /READ)
      IF (ifileptr LE 0) THEN BEGIN
            print,'Could not open the file', fitfile_name
      ENDIF
      ENDIF ELSE BEGIN
            ifileptr= OldFitOpen( fitfile_name)
      IF (ifileptr.fitunit LE 0) THEN BEGIN
                 print,'Could not open the file', fitfile_name
      ENDIF
```

```
      ENDELSE
      IF new_file THEN BEGIN
            status= FitSeek( ifileptr, 93, 1, 1, 0, 0, 0, atme=atme)
            status= FitRead( ifileptr, prm, fit)
      ENDIF ELSE BEGIN
            status= OldFitSeek( ifileptr, 93, 1, 1, 0, 0, 0, atme=atme)
            status= OldFitRead( ifileptr, prm, fit)
      ENDELSE
      yr = prm.time.yr
      mo = prm.time.mo
      dy = prm.time.dy
      if hr lt 10 then hour='0'+string(hr,format='(i0)') else
hour=string(hr,format='(i0)')
      if mn lt 10 then minu='0'+string(mn,format='(i0)') else
minu=string(mn,format='(i0)')
      if mn eq 0 then minu='00'
      if mo lt 10 then month='0'+string(mo,format='(i0)') else
month=string(mo,format='(i0)')
      if dy lt 10 then day='0'+string(dy,format='(i0)') else
day=string(dy,format='(i0)')
      bin_min=27
      bin_max=27
      start_time=9
      end_time=10
      outgraph='/home/liu/arc/results/20071107/test/'+string(yr,format=
'(i4)')+month+day+'_'+string(start_time,format='(i2)')+'_'+string(end_t
ime,format='(i2)')+'_'+string(bin_min,format='(i2)')+'_'+string(bin_max
,format='(i2)')+'_graph_test.ps'
      hr = 9
      mn = 48
      sc = 0
      e_hr = 9
      e_mn = 51
      e_sc = 0
      low_range = 0                        ; start at range gate zero
      high_range = 74               ; go to last range gate
      n_scans = 30000
      vel =  fltarr(high_range+1,n_scans)
      ele=vel
      vel_err = vel
      pwr_l = vel
      width_l = vel
      time = fltarr(n_scans)
      beamnum = time
      k = 0l
      range = 0
      hour = 0
      minute = 0
      second = 0
      bmnum = 0
      s_time= cnv_mdhms_sec(yr,mo,dy,hr,mn,sc)
      IF new_file THEN BEGIN
            status= FitSeek( ifileptr, yr, mo, dy, hr, mn, sc,
atme=atme)
      ENDIF ELSE BEGIN
            status= OldFitSeek( ifileptr, yr, mo, dy, hr, mn, sc,
atme=atme)
```

```
      ENDELSE
      last_time = cnv_mdhms_sec(yr,mo,dy,e_hr,e_mn,e_sc)
      WHILE (s_time LT last_time) DO BEGIN
            IF new_file THEN BEGIN
                  status= FitRead( ifileptr, prm, fit)
            ENDIF ELSE BEGIN
                  status= OldFitRead( ifileptr, prm, fit)
            ENDELSE
            s_time=
cnv_mdhms_sec(yr,mo,dy,prm.time.hr,prm.time.mt,prm.time.sc)
            IF (s_time LT last_time) THEN BEGIN
            ;***************place end of day check here so program
doesn't crash at end of file
                  time(k) = prm.time.hr*3600l + prm.time.mt*60l +
prm.time.sc
                  beamnum(k) = prm.bmnum
                  FOR range = low_range,high_range DO BEGIN
                        vel(range,k) = fit.v(range)
                        pwr_l(range,k) = fit.p_l(range)
                        width_l(range,k) = fit.w_l(range)
                        vel_err(range,k) = fit.v_e(range)
                        ele(range,k) = fit.elv(range)
                  ENDFOR
                  k = k+1
            ENDIF
      ENDWHILE
      k = k -1
      time = time(0:k)
      beamnum = beamnum(0:k)
      vel = vel(*,0:k)
      pwr_l = pwr_l(*,0:k)
      width_l = width_l(*,0:k)
      vel_err = vel_err(*,0:k)
      ele =ele(*,0:k)
      ;close fit file
      IF new_file THEN BEGIN
            CLOSE, ifileptr
            FREE_LUN, ifileptr
      ENDIF ELSE BEGIN
            status= OldFitClose( ifileptr)
      ENDELSE
set_plot,'ps'
            set_plot,'ps'
            device,/landscape,/inches,xsize=9.3125,ysize=6.9688, $
      filename=outgraph,font_size=8,yoffset=10.3125,xoffset=0.25,/color
,/helvetica
            graph_title=station+';
'+string(prm.time.yr,format='(i4)')+'/'+string(prm.time.mo,format='(i0)
')$
                  +'/'+string(prm.time.dy,format='(i0)')
            !P.MULTI = [0,1,3]
            loadct,12
                  x=time(0:30)/3600.
                  test=where(time gt start_time*3600. and time le
end_time*3600. ,count)
                  v1=vel(bin_min,test)
                  w1=width_l(bin_min,test)
```

```
                  p1=pwr_l(bin_min,test)
                  e1=ele(bin_min,test)
                  beam1=beamnum(test)
!P.position=[.1,0.6,0.9,0.85]
plot, beam1,p1,ytitle='Power
(dB)',font=0,charsize=3,xrange=[0,15],yrange=[0,50],title=day+'
'+'Nov'+' ' +string(yr,format='(i4)')+'
'+'Bin='+string(bin_min,format='(i2)')+','+string(hr,format='(i2)')+':'
+string(mn,format='(i2)')+'--
'+string(e_hr,format='(i2)')+':'+string(e_mn,format='(i2)')+'
'+'UT',xtickname=STRARR(4)+' ',/nodata
oplot, beam1,p1,psym=2

            for j=bin_min+1,bin_max do begin
                  beam_plot=where(pwr_l(j,*) GT 3 AND width_l LT 800. ,
beam_num)
                        IF beam_num GT 0 THEN BEGIN
                    oplot, beam1,pwr_l(j,beam_plot),psym=2
                        ENDIF
            endfor
      pwr_gate_avg = fltarr(16)
            FOR z=0, 15 DO BEGIN
                  for j=bin_min,bin_max do begin
                       pwr_loc = where(pwr_l(j,*) GT 3 AND width_l(j,*)
LT 800 AND vel(j,*) NE 0 AND beamnum EQ z,pwr_loc_cnt)
                        IF pwr_loc_cnt GT 0 THEN
pwr_gate_avg(z)=MEDIAN(pwr_l(j,pwr_loc))
                  ENDFOR
            ENDFOR
            pwr_gate_x=INDGEN(z+1)
            oplot,pwr_gate_x,pwr_gate_avg[pwr_gate_x],psym=2
            oplot,
pwr_gate_x,pwr_gate_avg[pwr_gate_x],color=200,thick=2
            oplot, [4,4],[0,50],linestyle=2
            xyouts, 4.2,35,'Arc  position',charsize=1.5,font=0
!P.position=[.1,0.35,0.9,0.6]
 plot, beam1,v1,ytitle='Velocity
(m/s)',psym=4,font=0,charsize=3,xrange=[0,15],yrange=[-
600,600],xtickname=STRARR(4)+' '
            for j=bin_min+1,bin_max do begin
                  beam_plot=where(pwr_l(j,*) GT 3 AND width_l LT 800.,
beam_num)
                        IF beam_num GT 0 THEN BEGIN
                    oplot, beam1,vel(j,beam_plot),psym=4
                        ENDIF
            endfor
vel_gate_avg = fltarr(16)
            FOR z=0, 15 DO BEGIN
                  for j=bin_min,bin_max do begin
                       vel_loc = where(pwr_l(j,*) GT 3 AND width_l(j,*)
LT 800 AND vel(j,*) NE 0 AND beamnum EQ z,vel_loc_cnt)
                        IF vel_loc_cnt GT 0 THEN
vel_gate_avg(z)=MEDIAN(vel(j,vel_loc))
                  ENDFOR
            ENDFOR
            vel_gate_x=INDGEN(z+1)
            oplot,vel_gate_x,vel_gate_avg[vel_gate_x],psym=4
```

```
            oplot,
vel_gate_x,vel_gate_avg[vel_gate_x],color=200,thick=2
            oplot, [4,4],[-600,600],linestyle=2
            oplot, [0,15],[0,0],linestyle=2
!P.position=[.1,0.1,0.9,0.35]
 plot, beam1,w1,ytitle='Width (m/s)',psym=7,font=0,xtitle='Beam
Number',charsize=3,xrange=[0,15],yrange=[0,800]
            for j=bin_min+1,bin_max do begin
                  beam_plot=where(pwr_l(j,*) GT 3 AND width_l LT 800. ,
beam_num)
                        IF beam_num GT 0 THEN BEGIN
                    oplot, beam1,width_l(j,beam_plot),psym=7
                        ENDIF
            endfor
width_gate_avg = fltarr(16)
            FOR z=0, 15 DO BEGIN
                  for j=bin_min,bin_max do begin
                        width_loc = where(pwr_l(j,*) GT 3 AND
width_l(j,*) LT 800 AND vel(j,*) NE 0 AND beamnum EQ z,width_loc_cnt)
                        IF width_loc_cnt GT 0 THEN
width_gate_avg(z)=MEDIAN(width_l(j,width_loc))
                  ENDFOR
            ENDFOR
            width_gate_x=INDGEN(z+1)
            oplot,width_gate_x,width_gate_avg[width_gate_x],psym=7
            oplot,
width_gate_x,width_gate_avg[width_gate_x],color=200,thick=2
            oplot, [4,4],[0,800],linestyle=2
      device, /close;graph file close
END;fit_avg_plot
;plot y error bars
PRO error_bar_y,x,y,y_e,x_e,clr
 oplot,[x,x],[y-y_e,y+y_e],color=clr
 oplot,[x-x_e,x+x_e],[1.0,1.0]*(y-y_e),color=clr
 oplot,[x-x_e,x+x_e],[1.0,1.0]*(y+y_e),color=clr
END
;plot x error bars
PRO error_bar_x,x,y,y_e,x_e,clr
 oplot,[x-x_e,x+x_e],[y,y],color=clr
 oplot,[1.0,1.0]*(x-x_e),[y-y_e,y+y_e],color=clr
 oplot,[1.0,1.0]*(x+x_e),[y-y_e,y+y_e],color=clr
END

;Range_plot.pro
PRO run_example
      fitfile = '20071107'
      fitloc = '/2007/11/'
      shr = 9
      smn = 0
      ehr = 10
      emn = 0
      fit_avg_plot,shr,smn,ehr,emn,7,fitfile+'.C0.rkn.fitacf','rank/'
END
PRO fit_avg_plot,$;function call
                  hr,$;start hour
                  mn,$;start minute
                  e_hr,$;end hour
```

```
                  e_mn,$;end minute
                  beam1,$;specified beam
                  fitfile_name,$;fit file name
                  loc;file location string
print,fitfile_name
      station = 'Rankin'
      IF ( STRPOS( fitfile_name, 'gz') NE (-1) ) THEN BEGIN
            print,'gzip compressed files cannot be read: ',
fitfile_name
      ENDIF
      IF ( STRPOS( fitfile_name, 'bz2') NE (-1) ) THEN BEGIN
            print,'bzip2 compressed files cannot be read: ',
fitfile_name
      ENDIF
      IF (( STRPOS( fitfile_name, 'fitacf') EQ (-1) ) AND
( STRPOS( fitfile_name, 'fit') EQ (-1) ) )THEN BEGIN
            print,'This is neither an old style nor a new style fit
file: ', fitfile_name
      ENDIF
      new_file= ( STRPOS( fitfile_name, 'fitacf') NE (-1) )
      IF new_file THEN BEGIN
            ifileptr= FitOpen( fitfile_name, /READ)
      IF (ifileptr LE 0) THEN BEGIN
            print,'Could not open the file', fitfile_name
      ENDIF
      ENDIF ELSE BEGIN
            ifileptr= OldFitOpen( fitfile_name)
      IF (ifileptr.fitunit LE 0) THEN BEGIN
                  print,'Could not open the file', fitfile_name
      ENDIF
      ENDELSE
      IF new_file THEN BEGIN
            status= FitSeek( ifileptr, 93, 1, 1, 0, 0, 0, atme=atme)
            status= FitRead( ifileptr, prm, fit)
      ENDIF ELSE BEGIN
            status= OldFitSeek( ifileptr, 93, 1, 1, 0, 0, 0, atme=atme)
            status= OldFitRead( ifileptr, prm, fit)
      ENDELSE
      yr = prm.time.yr
      mo = prm.time.mo
      dy = prm.time.dy
      if hr lt 10 then hour='0'+string(hr,format='(i0)') else
hour=string(hr,format='(i0)')
      if mn lt 10 then minu='0'+string(mn,format='(i0)') else
minu=string(mn,format='(i0)')
      if mn eq 0 then minu='00'
      if mo lt 10 then month='0'+string(mo,format='(i0)') else
month=string(mo,format='(i0)')
      if dy lt 10 then day='0'+string(dy,format='(i0)') else
day=string(dy,format='(i0)')
      hr = 9
      mn = 40
      sc = 0 ;start time
      e_hr = 9
      e_mn = 55
      e_sc = 0 ;endtime
      low_range = 0                ; start at range gate zero
```

```
      high_range = 74               ; go to last range gate
      n_scans = 30000
      vel =  fltarr(high_range+1,n_scans)
      vel_err = vel
      pwr_l = vel
      width_l = vel
      ele = vel
      time = fltarr(n_scans)
      beamnum = time
      k = 0l
      range = 0
      hour = 0
      minute = 0
      second = 0
      bmnum = 0
      outgraph
='/home/liu/arc/results/20071107/range_gate/'+string(yr,format='(i4)')+
month+day+'_'+string(beam1,format='(i0)')+'_'+string(hr,format='(i0)')+
string(mn,format='(i0)')+'_'+string(e_hr,format='(i0)')+string(e_mn,for
mat='(i0)')+'_'+'gate.ps'
      s_time= cnv_mdhms_sec(yr,mo,dy,hr,mn,sc)
      ; seek to first record
      IF new_file THEN BEGIN
            status= FitSeek( ifileptr, yr, mo, dy, hr, mn, sc,
atme=atme)
      ENDIF ELSE BEGIN
            status= OldFitSeek( ifileptr, yr, mo, dy, hr, mn, sc,
atme=atme)
      ENDELSE
      last_time = cnv_mdhms_sec(yr,mo,dy,e_hr,e_mn,e_sc)
      ;read in data from fit file
      WHILE (s_time LT last_time) DO BEGIN
            IF new_file THEN BEGIN
                  status= FitRead( ifileptr, prm, fit)
            ENDIF ELSE BEGIN
                  status= OldFitRead( ifileptr, prm, fit)
            ENDELSE
            s_time=
cnv_mdhms_sec(yr,mo,dy,prm.time.hr,prm.time.mt,prm.time.sc)
            IF (s_time LT last_time) THEN BEGIN
            ;***************place end of day check here so program
doesn't crash at end of file
                  time(k) = prm.time.hr*3600l + prm.time.mt*60l +
prm.time.sc       ; time in second from start of day
                  beamnum(k) = prm.bmnum
                  FOR range = low_range,high_range DO BEGIN
                        vel(range,k) = fit.v(range)
                        pwr_l(range,k) = fit.p_l(range)
                        width_l(range,k) = fit.w_l(range)
                        vel_err(range,k) = fit.v_e(range)
                        ele(range,k)=fit.elv(range)
                  ENDFOR
                  k = k+1
            ENDIF
      ENDWHILE
      ;truncate arrays
      k = k -1
```

```
      time = time(0:k)
      beamnum = beamnum(0:k)
      vel = vel(*,0:k)
      pwr_l = pwr_l(*,0:k)
      width_l = width_l(*,0:k)
      vel_err = vel_err(*,0:k)
      ele =ele(*,0:k)
      ;close fit file
      IF new_file THEN BEGIN
            CLOSE, ifileptr
            FREE_LUN, ifileptr
      ENDIF ELSE BEGIN
            status= OldFitClose( ifileptr)
      ENDELSE
      x=time (0:30)
      blank = strarr(60)
      for iii=0, 59 DO blank(iii)=' '
      f_vel = fltarr(k+1)
      f_wid = f_vel
      f_pow = f_vel
      f_err = f_vel
      f_vel_sd = f_vel
      f_intsd = fltarr(40)
      f_interr = f_intsd
      e_vel = fltarr(k+1)
      e_wid = e_vel
      e_pow = e_vel
      e_err = e_vel
      e_vel_sd = e_vel
      e_intsd = fltarr(3)
      e_interrr = e_intsd
      e_bin2 = intarr(k+1)
      f_bin2 = intarr(k+1)
      FOR i1 = 0, k DO BEGIN
            f_vel(i1) = 0.
            f_wid(i1) = 0.
            f_pow(i1) = 0.
            f_err(i1) = 0.
            count = 0.
            ;select f region based on max abs vel
            max_vel_f = max(vel(11:41,i1));max f vel
            min_vel_f = min(vel(11:41,i1));min f vel
            ;select max locations appropriate to polarity of max f
vel,+11 is to set first gate at 11 rather than 0 as where sets it
            IF max_vel_f GT 0 THEN max_vel_gate = where(vel(11:41,i1)
GE 0.60*max_vel_f,max_vel_cnt)+11
            IF max_vel_f LT 0 THEN max_vel_gate = where(vel(11:41,i1)
GE 1.40*max_vel_f,max_vel_cnt)+11
            ;select min locations appropriate to polarity of min f
vel,+11 is to set first gate at 11 rather than 0 as where sets it
            IF min_vel_f LT 0 THEN min_vel_gate = where(vel(11:41,i1)
LE 0.60*min_vel_f,min_vel_cnt)+11
            IF min_vel_f GE 0 THEN min_vel_gate = where(vel(11:41,i1)
LE 1.40*min_vel_f,min_vel_cnt)+11
            ;set to null if min/max f vel is 0
            IF min_vel_f EQ 0 THEN min_vel_cnt = 0
            IF max_vel_f EQ 0 THEN max_vel_cnt = 0
```

```
            ;determine if max or min vel average required
            IF max_vel_cnt GT min_vel_cnt THEN BEGIN
                  f_gate = max_vel_gate
                  f_count = max_vel_cnt
                  f_peak = where(vel(11:40,i1) EQ max_vel_f)+11
            ENDIF ELSE BEGIN
                  f_gate = min_vel_gate
                  f_count = min_vel_cnt
                  f_peak = where(vel(11:40,i1) EQ min_vel_f)+11
            ENDELSE
            IF f_count EQ 1 THEN BEGIN
                  ;creat set to exclude single data point
                  excld_max = where(vel(11:41,i1) LT max_vel_f)+11
                  excld_min = where(vel(11:41,i1) GT min_vel_f)+11
                  ;find next highest extrememax
                  max_vel_f = max(vel(excld_max,i1))
                  min_vel_f = min(vel(excld_min,i1))
                  ;select max locations appropriate to polarity of max
f vel,+10 is to set first gate at 10 rather than 0 as where sets it
                  IF max_vel_f GT 0 THEN max_vel_gate =
where(vel(11:41,i1) GE 0.60*max_vel_f AND vel(11:41,i1) LE
max_vel_f,max_vel_cnt)+11
                  IF max_vel_f LT 0 THEN max_vel_gate =
where(vel(11:41,i1) GE 1.40*max_vel_f AND vel(11:41,i1) LE
max_vel_f,max_vel_cnt)+11
                  ;select min locations appropriate to polarity of min
f vel,+10 is to set first gate at 10 rather than 0 as where sets it
                  IF min_vel_f LT 0 THEN min_vel_gate =
where(vel(11:41,i1) LE 0.60*min_vel_f AND vel(11:41,i1) GE
min_vel_f,min_vel_cnt)+11
                  IF min_vel_f GE 0 THEN min_vel_gate =
where(vel(11:41,i1) LE 1.40*min_vel_f AND vel(11:41,i1) GE
min_vel_f,min_vel_cnt)+11
                  ;set to null if min/max f vel is 0
                  IF min_vel_f EQ 0 THEN min_vel_cnt = 0
                  IF max_vel_f EQ 0 THEN max_vel_cnt = 0
                  IF max_vel_cnt GT min_vel_cnt THEN BEGIN
                        f_gate = max_vel_gate
                        f_count = max_vel_cnt
                        f_peak = where(vel(11:41,i1) EQ max_vel_f)+11
                  ENDIF ELSE BEGIN ;if not then perform min vel avg
                        f_gate = min_vel_gate
                        f_count = min_vel_cnt
                        f_peak = where(vel(11:41,i1) EQ min_vel_f)+11
                  ENDELSE
            ENDIF
            FOR j1 = 0, f_count-1 DO BEGIN
                  IF abs(vel(f_gate(j1),i1)) GE 25 AND
width_l(f_gate(j1),i1) LT 500. AND width_l(f_gate(j1),i1) GT 25 AND
pwr_l(f_gate(j1),i1) GT 3. AND vel_err(f_gate(j1),i1) LE 250 THEN BEGIN
                        f_vel(i1) += vel(f_gate(j1),i1)
                        f_wid(i1) += width_l(f_gate(j1),i1)
                        f_pow(i1) += pwr_l(f_gate(j1),i1)
                        f_intsd(j1) = vel(f_gate(j1),i1)
                        f_interr(j1) = vel_err(f_gate(j1),i1)
                        count += 1.
                  ENDIF
```

```
            ENDFOR
            IF count GT 0 THEN BEGIN
                  f_vel(i1) = f_vel(i1)/count
                  f_wid(i1) = f_wid(i1)/count
                  f_pow(i1) = f_pow(i1)/count
                  f_err(i1) = max(f_interr)
                  f_bin2(i1) = f_peak
            ENDIF
            IF count GE 2 THEN f_vel_sd(i1) = stddev(f_intsd(0:f_count-
1)) ELSE f_vel_sd(i1) = 0
      ENDFOR
      FOR i2 = 0, k DO BEGIN
            e_vel(i2) = 0.
            e_wid(i2) = 0.
            e_pow(i2) = 0.
            e_err(i2) = 0.
            count2 = 0.
            max_pwr_e = max(pwr_l(3:10,i2))
            mid_gate_e = where(pwr_l(3:10,i2) EQ max_pwr_e,g_num)
            low_gate_e = mid_gate_e(n_elements(mid_gate_e)-1)-1+3
            high_gate_e = mid_gate_e(n_elements(mid_gate_e)-1)+1+3
            FOR j2 = low_gate_e, high_gate_e DO BEGIN
                  IF abs(vel(j2,i2)) GT 25 AND width_l(j2,i2) LT 500.
AND width_l(j2,i2) GT 25 AND pwr_l(j2,i2) GT 3. AND vel_err(j2,i2) LE
150 THEN BEGIN
                        e_vel(i2) += vel(j2,i2)
                        e_wid(i2) += width_l(j2,i2)
                        e_pow(i2) += pwr_l(j2,i2)
                        e_intsd(j2-low_gate_e) = vel(j2,i2)
                        e_interr = vel_err(j2,i2)
                        count2 += 1.
                  ENDIF
            ENDFOR
            IF count2 GT 0 THEN BEGIN
                        e_vel(i2) = e_vel(i2)/count2
                        e_wid(i2) = e_wid(i2)/count2
                        e_pow(i2) = e_pow(i2)/count2
                        e_err(i2) = max(e_interr)
                        e_bin2(i2) = mid_gate_e(n_elements(mid_gate_e)-
1)+3
            ENDIF
            IF count2 GE 2 THEN e_vel_sd(i2) = stddev(e_intsd(0:count2-
1)) ELSE e_vel_sd(i2)=0
      ENDFOR
      beamset = where(beamnum EQ beam1,count_beam)
      start_time=9.0
      end_time=10.0
      set = where(beamnum EQ beam1 AND f_vel NE 0 AND time GE
start_time*3600 AND time LT end_time*3600, num_set)
      set2 = where(beamnum EQ beam1 AND e_vel NE 0 AND time GE
start_time*3600 AND time LT end_time*3600,num_set2)
      set3 = where(beamnum EQ beam1 AND f_vel NE 0 AND e_vel NE 0 AND
time GE start_time*3600 AND time LT end_time*3600,num_set3)
      IF num_set NE 0 AND num_set2 NE 0 THEN BEGIN
            ;format x axis markings
            IF time(k)-time(0) LE 10800 THEN BEGIN
                  IF time(k)-time(0) LE 3600 THEN BEGIN
```

```
                        xtint = 300
                        xmn = 2

      get_ticks3,time(0),time(k),tickv,tickname,prm.time.yr,prm.time.mo
,count
                  ;place x axis mark every 30 mins if total time 1.5hr
to 3 hr
                  ENDIF ELSE BEGIN
                        xtint = 1800
;                       xmn = 3
      get_ticks2,time(0),time(k),tickv,tickname,prm.time.yr,prm.time.mo
,count
                  ENDELSE
            ;place x axis mark every hr if total time greater than 3 hr
            ENDIF ELSE BEGIN
                  xtint = 3600
                  xmn = 6

      get_ticks,time(0),time(k),tickv,tickname,prm.time.yr,prm.time.mo,
count
            ENDELSE
            loadct,0
            !p.font=0
            set_plot,'ps'
            device,/landscape,/inches,xsize=10.3125,ysize=7.9688, $

      filename=outgraph,font_size=8,yoffset=10.3125,xoffset=0.25,/color
,/helvetica
            graph_title=day+' '+'Nov'+' ' +string(yr,format='(i4)')+'
'+'Beam='+string(beam1,format='(i2)')+','+string(hr,format='(i2)')+':'+
string(mn,format='(i2)')+'--
'+string(e_hr,format='(i2)')+':'+string(e_mn,format='(i2)')+' '+'UT'
            !P.multi=[0,1,3]
            loadct,12
            !P.position=[.1,0.64,0.9,0.89]
            slant_range = (findgen(75));*45)+180
            FOR j = 0,count_beam-1 DO BEGIN
                  rng_plot=where(pwr_l(0:40,beamset(j)) GT 3 AND
width_l(0:40,beamset(j)) LT 800 AND vel(0:40,beamset(j)) NE 0,rng_num)
                  IF rng_num GT 0 THEN BEGIN
                        IF j EQ 0 THEN BEGIN

      plot,slant_range(rng_plot),pwr_l(rng_plot,beamset(j)),title=graph
_title,xtickname=blank,ytitle='Power (dB)',$

      yrange=[0,50],xrange=[slant_range(0),slant_range(40)],psym=2,char
size=4,font=0
                        ENDIF ELSE BEGIN

      oplot,slant_range(rng_plot),pwr_l(rng_plot,beamset(j)),psym=2;,th
ick=4
                        ENDELSE
                  ENDIF
            ENDFOR
            pwr_gate_avg = fltarr(41)
            FOR z=0, 40 DO BEGIN
```

```
                  pwr_loc = where(pwr_l(z,*) GT 3 AND width_l(z,*) LT
800 AND vel(z,*) NE 0 AND beamnum EQ beam1,pwr_loc_cnt)
                  IF pwr_loc_cnt GT 0 THEN
pwr_gate_avg(z)=MEDIAN(pwr_l(z,pwr_loc))
            ENDFOR
            oplot,slant_range,pwr_gate_avg,thick=4,color=200
            oplot,[29,29],[0,50],thick=4,linestyle=2
            xyouts, 4.5,
38,'Beam='+string(beam1,format='(i2)'),charsize=2.2
            xyouts, 29., 38,'Arc position',charsize=2.2
            !P.position=[.1,0.39,0.9,0.64]
            FOR j = 0,count_beam-1 DO BEGIN
                  rng_plot=where(pwr_l(0:40,beamset(j)) GT 3 AND
width_l(0:40,beamset(j)) LT 800 AND vel(0:40,beamset(j)) NE 0,rng_num)
                  IF rng_num GT 0 THEN BEGIN
                        IF j EQ 0 THEN BEGIN

      plot,slant_range(rng_plot),vel(rng_plot,beamset(j)),xtickname=bla
nk,ytitle='Velocity (m/s)',$
                                    yrange=[-
500,500],xrange=[slant_range(0),slant_range(40)],psym=4,charsize=4,font
=0
                        ENDIF ELSE BEGIN
oplot,slant_range(rng_plot),vel(rng_plot,beamset(j)),psym=4;,thick=4
                        ENDELSE
                  ENDIF
            ENDFOR
            vel_gate_avg = fltarr(41)
            FOR z=0, 40 DO BEGIN
                  vel_loc = where(pwr_l(z,*) GT 3 AND width_l(z,*) LT
800 AND vel(z,*) NE 0 AND vel(z,*) GT -500 AND vel(z,*) LT 500 AND
beamnum EQ beam1,vel_loc_cnt)
                  IF vel_loc_cnt GT 0 THEN
vel_gate_avg(z)=MEDIAN(vel(z,vel_loc))
            ENDFOR
            oplot,slant_range,vel_gate_avg,thick=4,color=200
            oplot, [29,29],[-600,600],thick=4,linestyle=2
            oplot, [0,40],[0,0],thick=4,linestyle=2
            !P.position=[.1,0.14,0.9,0.39]
            FOR j = 0,count_beam-1 DO BEGIN
                  rng_plot=where(pwr_l(0:40,beamset(j)) GT 3 AND
width_l(0:40,beamset(j)) LT 800 AND vel(0:40,beamset(j)) NE 0,rng_num)
                  IF rng_num GT 0 THEN BEGIN
                        IF j EQ 0 THEN BEGIN

      plot,slant_range(rng_plot),width_l(rng_plot,beamset(j)),xtitle='R
ange Gate',ytitle='Width (m/s)',$

      yrange=[0,800],xrange=[slant_range(0),slant_range(40)],psym=7,cha
rsize=4,font=0
                        ENDIF ELSE BEGIN

      oplot,slant_range(rng_plot),width_l(rng_plot,beamset(j)),psym=7
                        ENDELSE
                  ENDIF
            ENDFOR
            wid_gate_avg = fltarr(41)
```

```
            FOR z=0, 40 DO BEGIN
                  wid_loc = where(pwr_l(z,*) GT 3 AND width_l(z,*) LT
800 AND vel(z,*) NE 0 AND beamnum EQ beam1,wid_loc_cnt)
                  IF wid_loc_cnt GT 0 THEN
wid_gate_avg(z)=MEDIAN(width_l(z,wid_loc))
            ENDFOR
            oplot,slant_range,wid_gate_avg,thick=4,color=200
            oplot, [29,29],[0,800],thick=4,linestyle=2
      device, /close;graph file close
      print, 'Execution complete'
      ENDIF ELSE print,'No valid points in file '+fitfile_name
END;fit_avg_plot
;plot y error bars
PRO error_bar_y,x,y,y_e,x_e,clr
 oplot,[x,x],[y-y_e,y+y_e],color=clr
 oplot,[x-x_e,x+x_e],[1.0,1.0]*(y-y_e),color=clr
 oplot,[x-x_e,x+x_e],[1.0,1.0]*(y+y_e),color=clr
END
;plot x error bars
PRO error_bar_x,x,y,y_e,x_e,clr
 oplot,[x-x_e,x+x_e],[y,y],color=clr
 oplot,[1.0,1.0]*(x-x_e),[y-y_e,y+y_e],color=clr
 oplot,[1.0,1.0]*(x+x_e),[y-y_e,y+y_e],color=clr
END
```